Towards precise proton exchange membrane fuel cell cathode degradation prediction

Zur Erlangung des akademischen Grades eines
Doktors der Ingenieurwissenschaften (Dr.-Ing.)
von der KIT-Fakultät für Elektrotechnik und Informationstechnik des
Karlsruher Instituts für Technologie (KIT)

angenommene
Dissertation
von

David Alexander Bernhard, M.Sc.
geboren in: Aschaffenburg

Tag der mündlichen Prüfung:	12. Januar 2026
Referentin:	Prof. Dr.-Ing. Ulrike Krewer
Korreferent:	Prof. Dr. rer. nat. K. Andreas Friedrich

Preamble

"Ergebnisse, Meinungen und Schlüsse dieser Publikation sind nicht notwendigerweise die der Volkswagen Aktiengesellschaft."

"The results, opinions and conclusions expressed in this publication are not necessarily those of the Volkswagen Aktiengesellschaft."

Kurzfassung

Die vorliegende Dissertation befasst sich mit dem zentralen Problem der Kathoden-Degradation in Polymerelektrolytbrennstoffzelle (englisch Polymer Electrolyte Fuel Cell, PEM-FC) welche maßgeblich die Lebensdauer und Wirtschaftlichkeit von Brennstoffzellensystemen beeinflusst. Ziel der Arbeit ist die Entwicklung eines fortschrittlichen Modells zur Vorhersage kathodenbezogener Spannungsverluste infolge von Degradationsprozessen. Dieses Modell soll zur Optimierung von Betriebsstrategien beitragen und die Konzeption und Entwicklung langlebigerer Kathoden unterstützen. Die Degradation der PEM-FC, insbesondere auf der Kathodenseite, stellt eine der größten Herausforderungen in der Brennstoffzellentechnologie dar, da sie die Lebensdauer und somit die Wirtschaftlichkeit des Gesamtsystems maßgeblich bestimmt.
Bestehende Modelle konzentrieren sich zumeist auf den Verlust der elektrochemisch aktiven Oberfläche (ECSA), sind jedoch häufig nicht in der Lage, diese Verluste präzise in Spannungsverluste unter variierenden Betriebsbedingungen zu übersetzen. Diese begrenzte Prognosefähigkeit erschwert die gezielte Verbesserung der Betriebsführung sowie die Entwicklung langlebigerer Komponenten. Um diese Lücke zu schließen, wird in dieser Arbeit ein erweitertes diagnostisches Verfahren angewendet, um die zugrunde liegenden Ursachen der Kathoden-Degradation detailliert zu analysieren.
Dabei werden zentrale Kathodenparameter wie ECSA, Tafel-Slope, Austauschstromdichte, Massentransportwiderstand sowie PtOx-bedingte Spannungsverluste im Rahmen beschleunigter Alterungstests (AST) erfasst. Die Untersuchungen zeigen, dass die durch Oxidbildung verursachten Überspannungen mit zunehmender Alterung abnehmen und PtOx-Verluste stark vom Kathodenpotential abhängen. Gegen Ende der Tests nehmen PtOx-Verluste, mit Ausnahme bei sehr kleinen Stromdichten, deutlich ab, zeigen jedoch über alle Proben hinweg eine konsistente Abhängigkeit von der Halbzellenspannung. Trotz Berücksichtigung dieser PtOx-bedingten Effekte bleiben nicht zuordenbare Verluste bestehen bzw. erscheinen teils sogar erhöht – insbesondere bei höheren Stromdichten.
Darüber hinaus wird gezeigt, dass die Spannungsverluste im Zuge der Kathoden-Degradation mit zunehmender Stromdichte ansteigen, ohne dass sich dies durch eine Veränderung des ohmschen Widerstands erklären lässt. Die Analyse legt vielmehr nahe, dass Veränderungen im Tafel-Slope, welche auf strukturelle Veränderungen des Katalysators hinweisen, eine wesentliche Rolle spielen. Aufbauend auf einem bestehenden physikalischen Modell wird in dieser Arbeit die ECSA-Degradation unter verschiedenen AST-Bedingungen vorhergesagt. Der berechnete

ECSA-Verlust wird anschließend empirisch mit den gemessenen Spannungsverlusten korreliert, wobei neben der ECSA auch die Entwicklung von Tafel-Slope und Austauschstromdichte berücksichtigt wird.
Abschließend liefert die Dissertation ein umfassendes Modell zur Verknüpfung von ECSA-Verlusten und Spannungsabfall, welches neue Einblicke in die Alterung von PEM-Brennstoffzellen ermöglicht. Das Modell bietet damit eine wertvolle Grundlage für die Optimierung des Zellbetriebs und die Entwicklung robusterer Kathodenmaterialien mit dem Ziel, die Brennstoffzellentechnologie nachhaltiger und kosteneffizienter zu gestalten.

Abstract

The present dissertation focuses on the critical issue of cathode degradation in Polymer Electrolyte Membrane Fuel Cells (PEM-FCs), which significantly impacts the longevity and cost-effectiveness of fuel cell systems. The primary objective is to develop an advanced model for predicting cathode-related voltage losses during degradation processes. This model aims to optimize system operation strategies and guide the design of more durable cathodes.

PEM-FC degradation, particularly at the cathode, is a pivotal challenge in fuel cell technology, dictating the overall system's lifespan and economic viability. Although existing models attempt to forecast cathode degradation by primarily focusing on the loss of electrochemical active surface area (ECSA), they often fall short in accurately translating this degradation into voltage losses, especially under varying operational conditions. This gap in predictive capability limits the effectiveness of strategies aimed at improving operational efficiency and cathode longevity.

To address this, the dissertation employs an advanced diagnostic approach to dissect the underlying causes of cathode degradation. Key cathode properties, including ECSA, Tafel slope, exchange current density, mass transport resistance, and PtOx-related voltage losses, are measured during accelerated stress tests. These diagnostics reveal that the overpotential caused by oxide formation decreases with aging, and PtOx losses depend on the cathode potential. PtOx-related losses diminish towards the end of the test, except at the smallest current densities, and exhibit a consistent dependency on half-cell voltage across all samples. However, accounting for PtOx-related voltage losses, unassigned losses remain or even appear larger, showing a steady increase with current density.

Further it is demonstrated, that voltage losses associated with cathode degradation escalate with current density, which is not attributed to changes in ohmic resistance. Instead, the research highlights that variations in the Tafel slope, indicative of structural changes in the catalyst, play a significant role. By extending and parameterizing an existing physical model, the study predicts ECSA loss across a broad spectrum of accelerated stress test conditions. This predicted ECSA loss is then correlated with observed voltage losses through an empirical approach, accounting for changes in ECSA, Tafel slope, and exchange current density.

In conclusion, this dissertation provides a comprehensive model that links ECSA degradation with voltage loss, offering valuable insights for optimizing PEM-FC operation and enhancing cathode design. This model can serve as a crucial tool for advancing fuel cell technology, ultimately contributing to more sustainable and cost-effective energy solutions.

Acknowledgment

Acknowledgments

This thesis would not have been possible without the support of many people. For this reason, I would like to thank all the people who contributed to this work and supported me during this time.
First of all, I would like to thank my supervisor Prof. Dr.-Ing. Ulrike Krewer for her expert guidance, encouragement, continuous support, and critical feedback. All of it enhanced the quality of my thesis.
Many thanks to Dr. Sebastian Kirsch and Dr. Thomas Kadyk. Their scientific guidance, critical thinking, and ideas have been important for this research. I am especially grateful for the effort they invested in me, both professionally and personally.
I am also thankful to my second reviewer, Prof. Dr. rer. nat. Andreas Friedrich, and to Prof. Dr.-Ing. Martin Doppelbauer for chairing the examination board, as well as Prof. Dr.-Ing. Eric Sax and Prof. Dr.-Ing. Michael Heizmann for being part of the board.
Special thanks to my colleagues from InES and the entire team at Volkswagen AG Group Research Fuel Cell Department. The great working atmosphere, fruitful discussions, and many special moments made this journey unforgettable. I would particularly like to mention: Patrick Arnold, Alexander Fladung, Hannes Scholz, and Lukas Lübben.
Finally, I would like to thank the people in my life who supported me personally during my doctoral thesis and life. I would like to thank my partner Leonie for her endless support and patience, especially during the most demanding periods of the last years. I would like to thank my good friend Paul Elsholz for his critical feedback and motivating support. I would also like to thank my parents and siblings for their support and belief in me.

Braunschweig, im Monat Juni 2025 *David Alexander Bernhard*

Contents

1 Introduction

1.1 Motivation

The rapid growth of the global population and the ongoing spreading of technology is leading to a significant need for energy. Despite their severe negative impact on the environment coming along with their combustion, fossil fuels are still the primary source for energy supply [1, 2]. With a share of 23 % of the global carbon dioxide (CO_2) emissions the increasing number of light-duty vehicles (LDVs) and heavy-duty vehicles (HDVs) play an important role to reduce the carbon footprint, especially as the amount of greenhouse gas emission related to the transport sector increases faster than in any other energy-consuming sector [3]. Consequently, internal combustion engines (ICEs) need to be replaced in LDVs and HDVs. For the replacement of the ICEs either battery or fuel cell technology seems appropriate to provide local-CO_2-free propulsion power batteries or fuel cells can be used. Of course due to the higher well-to-wheel efficiency, batteries have an advantage in operating costs, especially for LDVs. But compared to lithium-ion batteries, fuel cells system can be adapted to power and energy demands, by increasing the size of the fuel cell stack or the hydrogen tank with a relative low weight penalty. Furthermore, fuel cell systems, like the the Proton Exchange Membrane, or Polymer Electrolyte Membrane Fuel Cell (PEM-FC) can be refueled twice as fast as battery systems (refueling PEM-FC: 5-10 min; fast charging battery system: 20 min for 80% state of charge), causing shorter downtime for fuel cell vehicles. Due to these beneficial properties the usage of fuel cells especially in HDVs attracted significant attention, recently [3–6]. From the available fuel cell technologies, the PEM-FC is the most promising fuel cell technology as a power supply in automotive applications [3, 5]. This technology is characterized by its good quick and cold start capability, the high power density, the flexible operating range and the lightweight and compact system design [3, 5]. Accordingly, the number of PEM-FC vehicles sold in the transport sector increases in recent years [7].
However, despite this first commercial success, there are still obstacles to overcome, to realize economic PEM-FC heavy duty trucks. One obstacle is the currently insufficient supply of hydrogen based on renewable primary energy resources plus the sparse network of hydrogen refueling stations. Besides these hydrogen-infrastructure related issues, a further and more technology related obstacle is caused by longevity and cost requirements of the HDV market. With a durability of more than 10000 hours, a loading of platinum group metals (PGM-loading: mainly Platinum)

of 0.4 mg/cm^2 and cost of \$170 per kW, current PEM-FC HDVs are not capable of replacing ICE driven HDVs at the moment [8]. To ensure, that PEM-FCs are a viable solution for the replacement of ICEs in the transport related industry, the following targets must be reached in the upcoming years [4, 9, 10]:

Table 1.1: Lifetime and cost targets of the PEM-FC system used in heavy duty vehicles until 2050 [4, 9, 10].

Year	Lifetime [h]	Costs [\$/kW]	PGM loading [mg/cm^2]
2023	$\geq$ 10000	80	$\geq$ 0.4
2030	25000	80	$\leq$ 0.3
2050	30000	60	$\leq$ 0.25

To meet these ambitious targets, it is necessary to increase the lifetime of the PEM-FC stack and to lower costs of the system. For both properties of the PEM-FC stack the used PGM catalyst is the most critical component, as it contributes significantly to the stack costs (40-60%) and due its instability under PEM-FC operation conditions it can determine the durability of the vehicle [3, 4, 8, 9]. In state of the art PEM-FCs around 90% of the catalyst material is used in the cathode. Consequently, an even deeper understanding of the lifetime limiting degradation process in PEM-FC cathodes is needed to develop better cathode catalyst, new degradation reducing operation strategies and to enable a reliable simulation of PEM-FC degradation under different operation conditions. These three aspects have a major impact on achieving the lifetime and cost requirements, to ensure the commercial competitiveness of PEM-FC HDVs.

1.2 Scope

The dissertation is about understanding and modeling cathode related voltage losses due to PEM-FC cathode degradation. The model is intended to be used in the optimization of system operation strategies of PEM-FC fuel cells to reduce cathode degradation. Thereby, the first step is to identify which degradation processes are the most relevant in PEM-FC cathode degradation. The second step is to understand how the formation of surface oxide on the Pt catalyst is influenced by degradation and how this impacts the interpretation of degradation related voltage losses. In a third step the gathered insights are use to extend a current PEM-FC degradation models to not only describe Pt surface loss during aging but also to predict voltage losses.

1.3 Outline

The introductory chapter of this work, Chapter 2, gives an overview of the general fundamentals, including a short description of the single components and used materials of a PEM-FC and a brief overview of the fundamental working principle. In a more detailed manner the different overpotentials, which are reducing the cell voltage depending on the current density are introduced. Furthermore, the degradation phenomena occurring in PEM-FCs are introduced, with a detailed description of the degradation of the cathode catalyst layer. It is also shown in this chapter, which of the so called accelerated stress tests are suitable to gain data about the cathode degradation in a reasonable amount of time. Finally, the state-of-the-art-approaches for PEM-FC degradation and performance loss predictions are introduced.
In Chapter 3, the experimental setup, the test procedures and the used diagnostic procedure are explained. Furthermore, it is described how the gathered data is processed to analyze the influence of the accelerated degradation testing on the used membrane electrode assembly and to develop a degradation model.
In Chapter 4, degradation related voltage losses obtained during accelerated stress tests are divided into different contributors and quantified by using the measured cathode properties. This break down enables the analysis how the PEM-FC performance is influenced by the cathode properties during lifetime. A special emphasis is put on the influence of oxide formation during lifetime and how changes in the oxide related losses lead to a so far unknown further contributor to performance loss in PEM-FCs.
In Chapter 5, a mathematical model, consisting of two submodels is presented. Its basic function is the prediction and analysis of voltage losses in proton exchange membrane fuel cells arising from accelerated stress testing. To describe the degradation of the catalyst active surface, the first submodel employs a statistical, physics-based population balance approach. This is then combined with an additional performance submodel. This second submodel is based on an extended Tafel approach allowing for the incorporation of the degradation of catalyst activity. The final chapter summarizes the results presented in Chapter 4 and 5 and concludes the main findings. Furthermore, approaches to improve and to validate the current model are suggested.

2 PEM-FC: Fundamentals and cathode degradation

This chapter provides an overview of PEM-FC fundamentals and topics related to PEM-FC degradation. Therefore, the different PEM-FC components, their functionalities and the working principle of the PEM-FC are introduced. It is shown how the performance of a PEM-FC depends on current density and which processes occur depending on the required load. This is necessary to understand how degradation of the different components can have an impact on cell performance within lifetime. A special focus is drawn on the degradation phenomena occurring in the PEM-FC cathode and their influence on cathode lifetime respectively performance. Finally, an overview of the state-of-the-art modeling approaches for PEM-FC respectively PEM-FC cathode degradation is given.

2.1 Components and materials used in PEM-FCs

In PEM fuel cells, the chemical energy contained in gaseous hydrogen is converted into electrical energy [11, 12]. The following chapter describes the components and materials needed for this conversion as well as the working principle of a PEM-FC. Figure 2.1 depicts the setup of a common PEM-FC single cell.

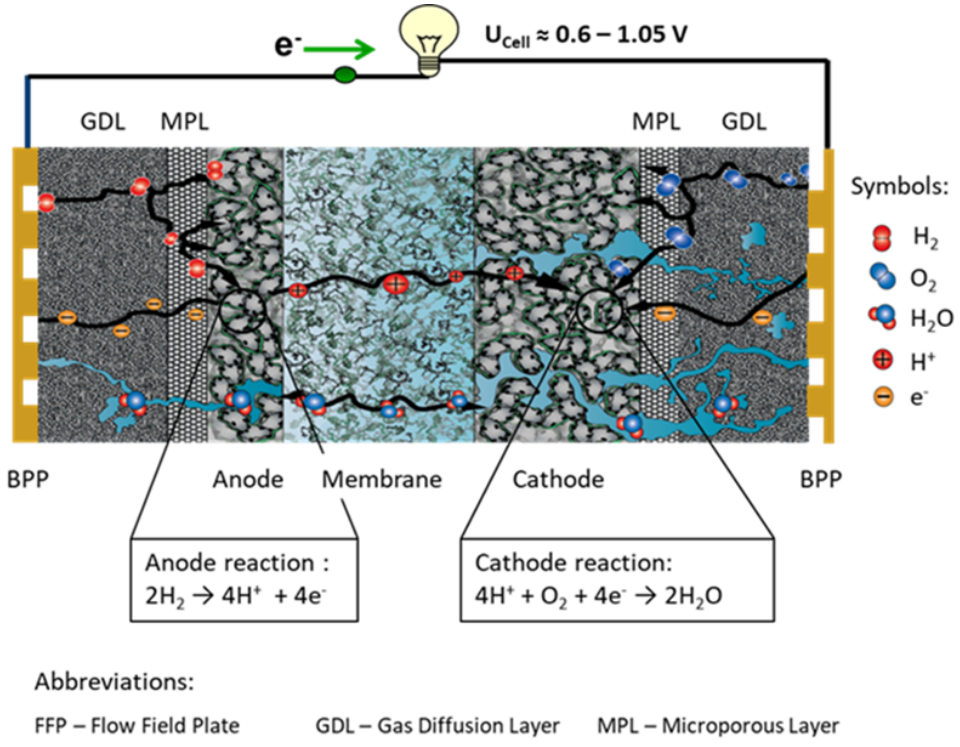

Figure 2.1: Schematic overview of a single cell PEM-FC setup.

Forming the site of energy production, the assembly of the two catalyst layers (CL) and the membrane placed between them can be seen as the centerpiece of a PEM-FC. It is referred to as catalyst coated membrane or CCM. The CCM is sandwiched between two gas diffusion layers (GDL), forming a structure known as membrane-electrode-assembly (MEA). In addition, the combination of the gas diffusion layers and the CLs are referred to as electrodes. The electrodes are divided into the anode and the cathode. The flow fields that embrace the MEA finalize the single cell. The properties and functionalities of these single cell subcompontents are wrapped up in the following.

The membrane in PEM-FCs (thickness of: 5-30 µm) must fulfill three different requirements. It needs to provide low permeability for H_2 and air, to avoid the mixing of the reactant gases [13]. Besides that, it has to act as an electrical insulation between the two electrodes. At the same time, the conduction of protons through the membrane must be possible. The most common membrane material in PEM-FCs is a polyperfluorosulfonic acid (PFSA). One of the most commonly used

PFSAs is the PFSA/polytetrafluoroethylene (PTFE) copolymer known by the trade name Nafion. The chemical structure of this polymer is shown in Figure 2.2.

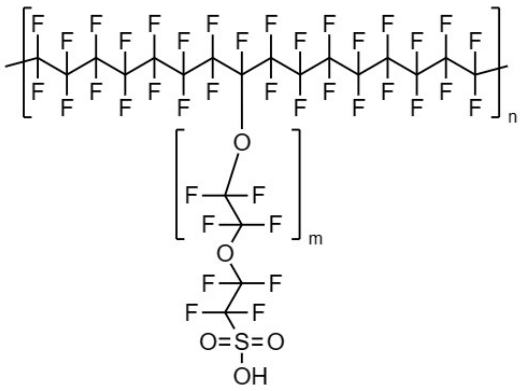

Figure 2.2: Chemical structure of the Nafion ionomer.

It consists of a tetrafluoroethylen (TFE) backbone and side chains with sulfonated acid groups. The TFE backbone mechanically and chemically stabilizes the co-polymer, which is necessary to prevent the mixing of the gases over the lifetime of the fuel cell. The terminal sulfonated acid groups enable the conduction of protons. To promote this function, a sufficiently high degree of humidification (>60 %) is needed to dissociate the acid groups and increase the mobility of the solvated protons, to guarantee proton conductivity [13–15].
The catalyst layers are in direct contact with the membrane and the GDL and must be adjusted to a number of requirements. The first requirement is to promote the conversion of the chemical energy into electrical energy. Therefore, they contain catalysts which accelerate the conversion of H_2 and air into energy and water [16, 17]. The material used in the anode catalyst layer is conventionally pure platinum, as it shows a high activity towards the oxidation of H_2 and is stable under normal PEM-FC operations conditions at the anode. Due to the high activity towards the conversion of hydrogen, platinum loadings lower than 0.1 mg_{Pt}/cm^2 are sufficient in the anodic CL [13, 14, 18]. In the cathode catalyst layer Platinum and Platinum-Alloy materials like Platinum-Cobalt (PtCo) are used, as these catalysts show a high catalytic activity towards the reduction of oxygen [13, 14, 16–18]. As the reduction of oxygen is sluggish in comparison to the hydrogen oxidation, higher loadings of the PGM (0.3-0.4 mg_{Pt}/cm^2) are needed in current automotive PEM-FC applications to achieve the required performance [4, 13, 14, 16–18]. To optimize the usage of the expensive precious metal used in both CLs, both catalysts are dispersed as nanoparticles (2-10 nm) on a porous particulate support material. By dispersing the catalyst, it is possible to maximize the number of active sites for the electrochemical reaction.

This distribution is described by the electrochemical active surface area (ECSA). Furthermore, the porosity of the support particles ensures the sufficient supply of H_2 and air to the active sites of the catalyst layers. In parallel it needs to be electrically conductive, as the electrons produced in the oxidation reaction at the anode must be conducted to the attached gas diffusion layer. Well established in CLs are graphitic carbons, like heat treated carbon blacks. These carbon materials offer enough surface area for a good distribution of the catalyst particles, a sufficient porosity for the gas supply and a high electrical conductivity. Besides that, the catalyst layers must be able to transport the produced protons. To enable the proton conduction, the electrodes are partly filled with electrolyte (10-30% of the pore volume), which covers the catalyst particles and allows the movement of protons through the support structure to the reactive catalyst particles. In most of the PEM-FC applications PFSAs, like Nafion, are used as electrolyte [19, 20].
A further requirement of the materials used in CLs is to minimize (if not avoid) flooding of the CL with produced water. Consequently, the CL needs to be hydrophobic. This hydrophobicity in the CL is an intrinsic property of the carbon catalyst. Additionally, enhancing the hydrophobicity of the reaction environment can further be facilitated by the electrolyte. However, this aspect seems to depend on the thickness of the ionomer film that builds upon covering the catalyst particles and its support. Thin films (opposite to bulk like thick films) might even offer a hydrophilic surface towards the gas phase as a consequence of chain arrangement in the film [21, 22].
State of the art GDL materials consist of two layers. The layer close to the CL is the so called micro-porous layer (MPL, pore size of 0.1-20 nm, thickness of 20-50 µm), the layer close to the flow field is thicker and stiffer and has a macro-porous structure (pore size of 1-100 µm, thickness of 200–300 µm) [13]. It is referred to as "substrate" as it serves as substrate for the MPL in the GDL production process. As substrate, carbon papers and carbon cloth are established. To reduce the accumulation of water, typically hydrophobic components like PTFE are added to the macro-porous structure [23–26]. The MPL has a number of function requirements. First of all the MPL-combination (anode and cathode) shall allow a good compromise between cathode electrode flooding (majorly when operating at temperature 60 °C) and CCM dry out (especially when operating at temperatures >80 °C in high loads). To help reduce the consequence of flooding, the MPL is hydrophobic and tightly attached to the electrodes, as pockets between electrodes and MPL would fill with water that cause mass transport losses. Accordingly, the MPL requires a certain degree of flexibility to allow for some plastic deformation upon compression. To help reduce dry out effects, the humidity of the CCM is to be kept high. With an optimized contact to the electrode and the substrate, the MPL reduces the CCM temperature. While a reduction of flooding is mandatory at low temperatures, a certain amount of water trapped within the CCM and thus forming a humidity buffer is advantageous at high temperatures. Therefore, especially at the anode, the MPL is dense and hydrophobic. Besides enabling operation in a wide temperature, pressure and load regime, the GDL also has to fulfill mechanical tasks, like minimizing damage to the CCM from puncturing by GDL fibers, counteracting the membrane swelling with proper elastic modulus or optimizing the compression under channels and ribs of the flow field

with the right stiffness [23–27].
In a single PEM-FC unit, the cell is supplied with the gaseous reactants via the anode and cathode Flow Field Plates (FFP). These plates can have various designs like parallel or serpentine flow channels. The FFPs have to provide the cell with a homogeneous gas supply. Besides the gas supply, various other functions need to be fullfilled by the FFPs in a PEM-FC. The plates are also responsible for the removal of the products and the conduction of electrons and heat released by the reaction. Moreover, they provide mechanical strength for the unit cell and spatial seperation of single unit cells if the cells are combined to a PEM-FC stack, in which case they are also the electrical connector between the single unit cells. Therefore, the flow fields are also known as Bipolare Plates (BPP). The following requirements need to be fulfilled by the FFPs: i) high thermal and electric conductivity, ii) strong corrosion resistance — particularly against Fenton-reactive species such as iron cations that accelerate membrane degradation [28, 29], iii) impermeability for gases and iv) sufficient mechanical strength. The materials used for FFPs are graphite, composites and metals, as these materials can fulfill all the listed requirements. Due to its physical and chemical properties, the good processability, the good availability and the low costs, stainless steel has proven to be a good fit for BPP in automotive applications, recently [30–34]. But also graphite and composite based FFPs can be found in automotive applications like PEM-FC buses.

2.2 Working principle of PEM-FCs

The generation of electric energy in a PEM-FC is related to the electrochemical conversion of the gases in the CL. Therefore the anode side is supplied with pure hydrogen, while the cathode side is supplied commonly with air or in more rarely cases with pure oxygen. The gases flow into the cell via the FFPs and are homogeneously transported to the CL by the diffusion layers (GDL and MPL). After the gases have passed the GDL and MPL, they are entering the CL via diffusion, as the tortuous and porous structure on the micrometer and nanometer scale length shelters the the electrode from the convective flow in the FFPs [25, 35]. By permeating the catalyst covering ionomer film, the reactants reach the catalyst material and the reactions can take place. At the anode, hydrogen is oxidized and dissociates into protons and electrons,

$$2H_2 \rightleftharpoons 4H^+ + 4e^-. \tag{2.1}$$

This reaction is known as the hydrogen oxidation reaction (HOR). As the CL and membrane are humidified, a hydrogen-bonded network builds up inside the ionomer. This networks enables the conduction of the produced proton from the anode to the cathode catalyst layer (CCL). In the CCL, the protons are further conducted by the ionomer to the catalyst particles. In parallel, electronic conduction takes place and the produced electrons are "moving" from the anode catalyst

particles to the cathode catalyst particles via the electric conductive pathway in the cell and the external load circuit. At catalyst particles, oxygen is reduced and water is formed,

$$O_2 + 4H^+ + 4e^- \rightleftharpoons 2H_2O. \tag{2.2}$$

This reaction is known as Oxygen Reduction Reaction (ORR). The HOR and ORR result in the following Redox-reaction,

$$O_2 + 2H_2 \rightleftharpoons 2H_2O. \tag{2.3}$$

In the following this Redox-reaction is brought into a thermodynamic context. As the produced electrons are conducted via the external circuit from the anode to the cathode, electrical work (W_{elec}) is done [25, 35, 36],

$$W_{elec} = q \cdot E. \tag{2.4}$$

Where q describes the conducted charge and E the electrical potential difference between anode and cathode, which is the driving force for the exchange of electrons. The moved charge q in a PEM-FC can be replaced by [25, 35, 36] ,

$$q = n \cdot F, \tag{2.5}$$

where n is the amount of electrons released by the conversion of a hydrogen molecule and F is the Faraday´s constant (96485 C/mol). Based on thermodynamic fundamentals, described in detail in different publications like Jiang et al. [35], Eikerling et al. [36] or O'Hayre et al. [25], the electrical work can also be linked to the change of the Gibbs Free Energy ΔG,

$$\Delta G = -W_{elec}. \tag{2.6}$$

Equation 2.6 defines the maximum electrical work, obtainable from a fuel cell reaction at constant temperature and pressure. In combination with the equations 2.4 and 2.5, the correlation between the electrical potential of the the Redox-reaction (see Equation 2.1-2.2) and the change in Gibbs free energy between the reactants and products is given

$$\Delta G = -n \cdot F \cdot E. \tag{2.7}$$

At standard conditions (T = 25 °C and p = 1.013 bar) Equation 2.7 defines the standard potential E^0 of the cell

$$E^0 = -\frac{\Delta G}{n \cdot F}, \tag{2.8}$$

which is also known as the reversible potential (E_{rev}) at standard conditions [25, 35, 36]. In the PEM-FC two E^0 are possible, as the produced water can be in gaseous or liquid form. In case of gaseous water formation ΔG^0 is -228.56 kJ/mol, which is also known as the change of the Gibbs

free energy at the lower heating value (LHV) $\Delta G^0{}_{LHV}$. If the water is in a liquid state, the ΔG^0 is increased to -237.2 kJ/mol, which is the higher ΔG^0 related to the higher heating value (HHV, $\Delta G^0{}_{HHV}$) [25, 35, 36]. This values result in the following standard potentials

$$E^0_{LHV} = -\frac{2 \cdot -228.56\ kJ/mol}{-4 \cdot 96485\ C/mol} = 1.18\ V \tag{2.9}$$

respectively,

$$E^0_{HHV} = -\frac{2 \cdot -237.2\ kJ/mol}{-4 \cdot 96485\ C/mol} = 1.23\ V. \tag{2.10}$$

These potentials are only valid at standard conditions, but PEM-FCs are mostly used at different conditions, like air instead of oxygen or elevated temperatures [25, 35, 36]. In this case the Nernst equation can be used to calculate the reversible potential of the cell,

$$E_{rev} = E^0 + \frac{\Delta S^0_{rxn}}{nF} \cdot (T - T_0) - \frac{RT}{nF} \cdot ln \frac{\prod a^{v_i}_{i,products}}{\prod a^{v_i}_{i,reactants}}. \tag{2.11}$$

Where the second term on the right hand side of Equation 2.11 describes the influence of PEM-FC operation at elevated temperatures. Which is determined by the entropy of reaction ΔS^0_{rxn} and the difference between the operation temperature T and the standard condition temperature T_0. The third term on the right hand side of this equation, is related to the activities a_i of the different species i participating in the electrochemical reaction as reactants and products. Their stochiometries of the reactions is represented by v_i. For a PEM-FC supplied with H_2 and ambient air, Equation 2.11 can be written as,

$$E_{rev} = E^0 + \frac{\Delta S^0_{rxn}}{nF} \cdot (T - T_0) - \frac{RT}{nF} \cdot ln \frac{a_{H_2O}}{a^2_{H_2} \cdot a_{O_2}}. \tag{2.12}$$

The activities of the reactants in Equation 2.12 can be replaced by the dimensionless partial pressures. Assuming that water is produced exclusively in the liquid phase, its activity, a_{H_2O}, is taken to be unity. Consequently, the reversible cell potential E_{rev} can be determined by using the following equation

$$E_{rev} = E^0 + \frac{\Delta S^0_{rxn}}{4F} \cdot (T - T_0) - \frac{RT}{4F} \cdot ln \frac{1}{p^2_{H_2} \cdot p_{O2}}. \tag{2.13}$$

Just like E_0 (see Equations 2.8-2.10), the entropy of reaction ΔS^0_{rxn} is defined by the physical state of the produced water. For gaseous water formation $\Delta S^0{}_{rxn}$ is -44.34 J/molK and -163.1 J/molK, if liquid water is produced [25, 35]. Accordingly, at 80 °C a E_{rev} of ~ 1.17 in the liquid water formation is reached (p_{H_2} = 1 and p_{O_2} = 0.21).

2.3 Cell voltage and overpotentials

The reversible cell potential introduced in the previous chapter can only be reached in an ideal system. In real PEM-FC applications, these theoretical values are reduced by the parasitic current arising from the H_2-crossover. In general, the measured voltage without an applied load (idle operation mode) in real PEM-FCs is between 0.95 and 1.05 V, depending on the efficiency of H_2-crossover suppression respectively on the reduction of the parasitic current. This voltage is known as the open circuit voltage of a fuel cell U_{OCV}. But more importantly, as soon as load is applied to the cell and an electric current is drawn, the cell voltage is reduced by different charge- and mass-transport phenomena. These voltage losses are called overpotentials, which reduce the cell voltage [25, 36–38]. They depend on the MEA properties and operation conditions. In Figure 2.3 an exemplary polarization curve is shown, highlighting the different overpotentials. As all overpotentials increase with current density, lower cell voltages are obtained when higher currents are drawn.

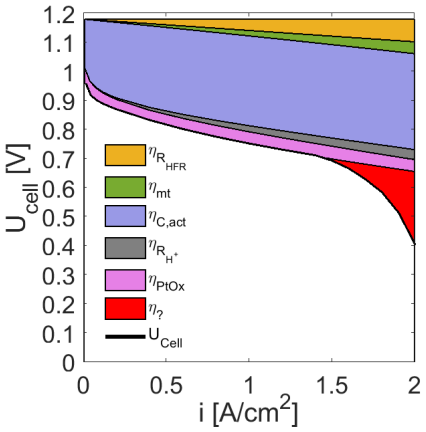

Figure 2.3: Exemplary polarization curve of an PEM-FC in the gaseous phase (product water is formed as vapor), the theoretical cell voltage is reduced by the different overpotentials explained in the following chapters.

In Equation 2.14, the cell voltage is described by subtracting up to seven different overpotentials (η_x) from the reversible cell potential E_{rev},

$$\begin{aligned} U_{Cell}(i) = E_{rev} &- \eta_{A,act}(i) - \eta_{C,act}(i) - \eta_{mt}(i) \\ &- \eta_{R_{HFR}}(i) - \eta_{R_{H^+}}(i) - \eta_{PtOx}(i) - \eta_{?}(i). \end{aligned} \tag{2.14}$$

here i stands for the current density (load point dependency). In the following, these overpotentials are introduced and their dependencies from the MEA properties and the load point are explained.

2.3.1 Anode activity related overpotential

The overpotential occuring at the anode is related to the activation energy needed to initialize the HOR. To explain why the anode overpotential can be approximated with an ohmic behavior, it is necessary to introduce the Butler-Volmer equation [25, 36, 39],

$$i = i_{0,HOR} \cdot ECSA_A \cdot \left[exp\left(\frac{\alpha_A nF}{RT} \cdot \eta_{A,act} \right) - exp\left(-\frac{(1-\alpha_A)nF}{RT} \cdot \eta_{A,act} \right) \right]. \tag{2.15}$$

On the left hand side of the Butler-Volmer equation for the HOR, i represents the current density. On the right hand side of Equation 2.19, $i_{0,HOR}$ describes the exchange current density, $ECSA_A$ represents the electrochemical active surface of the anode catalyst per electrode area (cm^2_{Pt}/cm^2), α_A describes the charge transfer coefficient of the anode, and the overpotential of the reaction is represented by $\eta_{A,act}$. In general, the exchange current density i_0 depends on the catalyst material and can be interpreted as a measure of the activity of a catalyst. The higher the exchange current density, the lower the overpotential of the reaction. It characterizes the reaction rate of a catalyst at the equilibrium, which means that the net turnover is zero [25, 36, 39]. With an exchange current density $i_{0,HOR}$ of 10^{-2} A/cm^2_{Pt}, the HOR in a PEM-FC can be described as a kinetically favored reaction and it is reasonable to assume low values for $\eta_{|A,act}$ ($i << i_{0,HOR} \cdot ECSA$) . With this assumption Equation 2.15 can be simplified to [39],

$$i = i_{0,HOR} \cdot ECSA_A \cdot \frac{nF}{RT} \cdot \eta_{A,act}, \tag{2.16}$$

respectively to

$$\eta_{A,act} = i \cdot \frac{RT}{nF \cdot i_{0,HOR} \cdot ECSA_A}. \tag{2.17}$$

Due to the high HOR-activity of Pt, only very small values of $\eta_{|A}$ in a PEM-FC occur, therefore the overpotential of the anode $\eta_{|A,act}$ is often set to zero

$$\eta_{A,act} = 0. \tag{2.18}$$

This is valid, if the Pt-loading in the anode is high enough ($0.03\ mg_{Pt}/cm^2$) and an ECSA higher than $20\ cm^2_{Pt}/cm^2$ is achieved [38, 40, 41]. In state-of-the-art automotive anodes these values are reached, consequently, $\eta_{|A,act}$ is disregarded in Figure 2.3.

2.3.2 Cathode activity related overpotential

The second overpotential on the right hand side of Equation 2.14 describes the voltage loss caused by the oxygen reduction reaction (see Equation 2.2). Also for this reaction the Butler-Volmer equation (see Equation 2.15) can be used to describe the current produced by the ORR depending on the cathode overpotential,

$$i + i_{H_2} = i_{0,ORR} \cdot ECSA_C \cdot \left[exp\left(\frac{\alpha_C nF}{RT} \cdot \eta_{C,act} \right) - exp\left(-\frac{(1-\alpha_C)nF}{RT} \cdot \eta_{C,act} \right) \right]. \quad (2.19)$$

On the left hand side of Equation 2.19, i represents the current density, which is corrected by the hydrogen crossover current i_{H2}. This current results from the membrane crossover of hydrogen from the anode to the cathode and the following conversion of hydrogen on the cathode catalyst. On the right hand side of Equation 2.19, $i_{0,ORR}$ describes the exchange current density of the ORR corrected for temperature and pressure influence to a reference exchange current density $i_{0,ORR,ref}$ [42]. $ECSA_C$ represents the active surface area of the cathode catalyst and α_C describes the cathodic charge transfer coefficient. The overpotential of the reaction is represented by $\eta_{C,act}$ [25, 36, 39]. As the $i_{0,ORR}$, catalyzed by a platinum catalyst is 5-8 magnitudes lower than $i_{0,HOR}$, the ORR can be described as a comparatively slow reaction and the simplification of the Butler-Volmer equation shown in the Equations 2.16-2.17 can not be applied [39]. But as soon as a load is applied to a PEM-FC, the requested current exceeds the exchange current density of the ORR by several orders of magnitude. Consequently, the second term on the right hand side of Equation 2.19, describing the backward reaction of the ORR, can be neglected and the equation can be simplified to

$$i + i_{H_2} = i_{0,ORR} \cdot ECSA_C \cdot \left[exp\left(-\frac{\alpha_C nF}{RT} \cdot \eta_{C,act} \right) \right] \quad (2.20)$$

whereby the overpotential related to cathode catalyst activity can be determined by rearranging this equation [25, 36, 39],

$$\eta_{C,act} = \frac{RT}{\alpha_C nF} \cdot ln\left(\frac{i + i_{H_2}}{i_{0,ORR} \cdot ECSA_C} \right) = \frac{2.3 \cdot RT}{\alpha nF} \cdot log\left(\frac{i + i_{H_2}}{i_{0,ORR} \cdot ECSA_C} \right). \quad (2.21)$$

According to the Tafel equation introduced by Julius Tafel in 1905, the constant values are known as the Tafel slope m,

$$m = \frac{2.3 \cdot RT}{\alpha nF}. \quad (2.22)$$

In literature a common value of the Tafel slope is 70 mV/dec [42–45]. This slope is reached at a temperature of 80 °C, a single electron step (n equals 1) and a charge transfer coefficient (α) of 1. This assumption is valid for small activity overpotentials, respectively low and medium current

densities. As $i_{0,HOR}$,α_A $\eta_{A,act}$ and $ECSA_A$ are not further discussed in the following chapters, $i_{0,ORR}$, α_C, $\eta_{C,act}$ and $ECSA_C$ are simplified to i_0, α, η_{act} respectively ECSA. The cathode activity related overpotential η_{act} is represented by the purple area in Figure 2.3.

2.3.3 Oxygen mass-transport related overpotential

In the previous chapter the voltage loss related to the overpotential needed, if a PEM-FC produces an electric current, is described. But in Equation 2.19 the assumption is drawn, that the concentration of reactants and products in the CL is unaffected by the conversion of oxygen into water (see Equation 2.2) taking place, as soon as load is applied. In reality, mass-transport phenomena in the cathode (GDL, MPL and CL) will cause a depletion of oxygen, especially at high loads [25].
To account for the decrease in oxygen concentration, the following concentration- resp. pressure-dependent expression for the exchange current density can be used

$$i_0 = i_0^{ref} \cdot \left(\frac{p_{O2,CL}}{p_{O2}^{ref}} \right)^{\gamma}. \tag{2.23}$$

Where i_0 is described by a reference exchange current density i_0^{ref} at any given temperature and the reference oxygen-partial pressure p_{O2}^{ref} (O_2 partial pressure at reference conditions of 101.3 kPa), related to the actual oxygen-partial pressure $p_{O2,CL}$ in the catalyst layer and γ represents the reaction order of the ORR wtr. to p_{O2}^{ref} [42]. By inserting Equation 2.23 into Equation 2.21, the overpotential related to cathode catalyst activity becomes

$$\eta_{act} = \frac{RT}{\alpha nF} \cdot ln \left(\frac{i + i_{H_2}}{i_0^{ref} \cdot \left(\frac{p_{O2,CL}}{p_{O2}^{ref}} \right)^{\gamma} \cdot ECSA} \right). \tag{2.24}$$

By expanding the ratio between $p_{O2,CL}$ and p_{O2}^{ref} by the oxygen-partial pressure in the channels of the FFP $p_{O2,FFP}$

$$\frac{p_{O2,CL}}{p_{O2}^{ref}} = \frac{p_{O2,FFP}}{p_{O2}^{ref}} \cdot \frac{p_{O2,CL}}{p_{O2,FFP}}, \tag{2.25}$$

Equation 2.24 can be rewritten as (n = 1),

$$\eta_{act} = \frac{RT}{\alpha F} \cdot ln \left(\frac{i + i_{H_2}}{i_0^{ref} \cdot \left(\frac{p_{O2,FFP}}{p_{O2}^{ref}} \right)^{\gamma} \cdot ECSA} \right) - \frac{RT}{\alpha F} \cdot \gamma \cdot ln \left(\frac{p_{O2,CL}}{p_{O2,FFP}} \right). \tag{2.26}$$

In this equation the first tern on the right hand side equals Equation 2.21 with a pressure corrected version of $i_{0,ORR}$. The second term on the right hand side describes the influence of the mass-transport resistance of the cathode on the activation overpotential [42],

$$\Delta\eta_{act,mt} = \frac{RT}{\alpha F} \cdot \gamma \cdot ln\left(\frac{p_{O2,CL}}{p_{O2,FFP}}\right). \tag{2.27}$$

Besides η_{act}, the mass-transport phenomena in the cathode also affects the E_{rev} described in Equation 2.13. With the expansion of the oxygen partial pressure term described in Equation 2.25, the pressure dependent term of Equation 2.13 can be written as (n equals 4)[42, 46],

$$E_{rev} = E^0 + \frac{\Delta S^0_{rxn}}{4F} \cdot (T - T_0) + \frac{RT}{4F} \cdot ln\left[\left(\frac{p_{H2,CL}}{p^{ref}_{H2}}\right)^2 \cdot \left(\frac{p_{O2,FFP}}{p^{ref}_{O2}}\right)\right] + \frac{RT}{4F} \cdot ln\left(\frac{p_{O2,CL}}{p_{O2,FFP}}\right). \tag{2.28}$$

The first three terms on the right hand side of Equation 2.28 defines E_{rev} like it is also shown in Equation 2.13 and the fourth term on the right hand side of Equation 2.28 is the mass-transport related effect of reactant depletion on E_{rev}, defined as $\Delta\eta_{Nernst,mt}$ [42, 46],

$$\Delta\eta_{Nernst,mt} = \frac{RT}{4F} \cdot ln\left(\frac{p_{O2,CL}}{p_{O2,FFP}}\right). \tag{2.29}$$

Accordingly, the entire voltage loss related to the oxygen mass-transport can be determined via

$$\eta_{mt}(i) = \Delta\eta_{Nernst,mt} + \Delta\eta_{act,mt} = \frac{RT}{4F} \cdot ln\left(\frac{p_{O2,CL}}{p_{O2,FFP}}\right) + \frac{RT}{\alpha F} \cdot \gamma \cdot ln\left(\frac{p_{O2,CL}}{p_{O2,FFP}}\right). \tag{2.30}$$

The oxygen partial pressure in the CL $p_{O2,CL}$ can be determined with the following equation derived by Gu et al. [47]

$$p_{O2,CL} = p_{O2,FFP} - \frac{RT}{4F} \cdot R_{mt} \cdot i. \tag{2.31}$$

With this correlation Equation 2.30 becomes

$$\eta_{mt}(i) = \frac{R \cdot T}{F} \cdot \left(\frac{1}{4} + \frac{\gamma}{\alpha}\right) \cdot ln\left(\frac{p_{O2} - \frac{R \cdot T}{4F} \cdot i \cdot R_{mt}(i)}{p_{O2}}\right), \tag{2.32}$$

where α represents the cathodic transfer coefficient obtained from the Tafel-slope, γ is the ORR reaction order with respect to oxygen partial pressure ($\gamma = 0.54$ according to Neyerlin et al. [48]) and $p_{O2,FFP}$ is the oxygen partial pressure present within the channels of the flow field. And the

oxygen mass-transport resistance of the cathode (GDL, MPL and CL) is represented by R_{mt} and can be calculated according to Baker et al. with the following equation [49]

$$R_{mt} = \frac{4F}{RT} \cdot \frac{p_{O2,FFP}}{i_{lim}}. \tag{2.33}$$

The limiting current density i_{lim} used in Equation 2.33 can be determined by stationary [49] or transient [50] limiting current measurement methods. The method used in this work is explained in Chapter 3.3. The influence of the overpotential η_{lmt} is shown by the green area in Figure 2.3. It is shown, that the influence of η_{lmt} increases with increasing current density.

2.3.4 Ohmic overpotentials

In the Chapters 2.3.1-2.3.3 the voltage losses related to catalyst activity and oxygen mass-transport are introduced. But as shown in Figure 2.1 protons and electrons need to be moved from the anode to the cathode to realize the electrochemical system and to generate electricity . These transport processes can be described by the Ohm´s law. Consequently they can be designated as ohmic overpotentials [25].
According to literature, the first charge-transport related overpotential is caused by the Ohmic resistance of the electrically conductive parts of the cell and the proton-transport through the membrane. Thereby, the ohmic losses caused by the membrane resistance can be minimized by a sufficiently high humidification of the membrane, due to the use of humidified reactant gases and the impact of the produced water. The second ohmic overpotential is linked to the transport of the protons from the membrane-electrode-interface to the catalyst particles. This transport is accompanied by losses which can be described by the proton transport resistance of the cathode ionomer $\mathrm{R_{H^+}}$.
The ohmic and proton transport resistance of the cathode ionomer can be obtained by fitting electrochemical impedance spectroscopy (EIS) data to a transmisssion line model, which describes the catalyst physics [51, 52]. In Figure 2.4 the Nyquist plot of an exemplary impedance spectra recorded between 50 Hz and 30 kHz and the fit of a transmission line model derived from Makharia et al. to this data is shown [51].

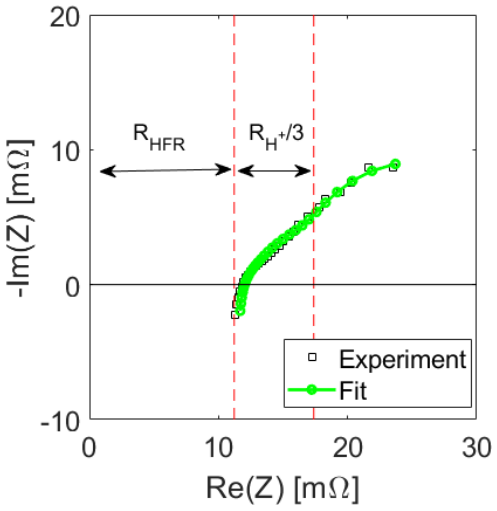

Figure 2.4: Fit of the measured impedance spectra and determination of the high frequency resistance R_{HFR} and cathode ionomer resistance R_{H^+} according to [51].

With this fit, the Ohmic resistance of the electrically conductive parts of the cell and the proton-transport through the membrane can be extracted by determining the high frequency intercept on the real impedance axis. As this resistance is related to a frequency of at least 1 kHz, it is known as the so-called high frequency resistance (R_{HFR})[51, 52]. With R_{HFR} the overpotential related the first ohmic overpotential ($\eta_{|R_{HFR}}$) can be calculated with the following equation

$$\eta_{R_{HFR}}(i) = i \cdot A \cdot R_{HFR}(i), \tag{2.34}$$

where A describes the active area of the MEA and i the current density [51]. This overpotential is represented by the yellow area in Figure 2.3.
According to Makharia et al. the resistance of the cathode ionomer R_{H^+} can be obtained from the 45 ° branch of the fit shown in Figure 2.4) and the related overpotential $\eta_{|R_{H^+}}$ (shown in Figure 2.3 in grey) can be described as [51]

$$\eta_{R_{H^+}}(i) = \frac{1}{3} \cdot i \cdot A \cdot R_{H^+}(i). \tag{2.35}$$

This resistance depends also on the humidification of the used polymer for the proton conduction, consequently it can be minimized with the proper choice of operation conditions of the PEM-FC system.

2.3.5 Platinum oxide related overpotential

The sixth overpotential described in Equation 2.14 is attributed to interaction of oxygen containing molecules and the catalyst particle surface. On the one hand this interaction is needed for the ORR, but on the other hand it reduces the cell performance. In literature this loss is linked to the formation of different oxide surface species on the catalyst particles in the cathode, which is referred to PtOx in this work [37, 43, 53–55]

$$Pt + H_2O/O_2 \Rightarrow PtOx. \tag{2.36}$$

The formation of oxides on the platinum surface of the PEM-FC catalyst nanoparticles is discussed in numerous publications like Alsabet et al. or Jerkiewicz et al. [37, 43, 55–67]. Based on Cyclic Voltammogram (CV) measurements and various simulations, the following conclusions about the oxidation process can be drawn: i) in a cell voltage range of 0.6 to 0.75 V, the oxidation process is induced by the physisorption of water on the Pt-surface [59, 62, 68] ii) in a voltage range of 0.75 to 0.85 V the oxidation of the Pt-surface starts to occur [59, 62, 63]. According to Jerkiwiecz et al., the adsorbed water gets discharged at a cell voltage of 0.85 V and oxygen is chemisorbed on two Pt atoms [62, 65],

$$2\,\mathrm{Pt} + \mathrm{H_2O} \leftrightharpoons \mathrm{Pt_2O} + 2\,\mathrm{H^+} + 2\,\mathrm{e^-}. \tag{2.37}$$

An unambiguous proof of the reaction shown in Equation 2.37 is still missing. Consequently, various other oxidation reactions involving further adsorption steps can be found in literature [61, 63, 66, 67]. iii) a further increase of the cell voltage causes further oxidation of the platinum surface [59, 62, 63, 65, 68],

$$2\,\mathrm{Pt_2O} + \mathrm{H_2O} \leftrightharpoons 2\,\mathrm{PtO} + 2\,\mathrm{H^+} + 2\,\mathrm{e^-}. \tag{2.38}$$

This ongoing oxidation is also linked to an intrusion of oxygen atoms into the atomic lattice of the platinum surface. Due to this intrusion, Pt-atoms are lifted from the original lattice, an occurence known as the "buckling" effect [69]. iv) as soon as a cell voltage of 1.05 V is reached, the so called place-exchange-mechanism occurs. This means that oxygen atoms are incorporated into the metal lattice, displacing platinum atoms and leading to the formation of so-called subsurface oxides,

$$PtO \leftrightharpoons PtO_{sub}. \tag{2.39}$$

Furthermore, it was shown in various studies that the built-up of the surface adsorbates and oxides described in Equations 2.37-2.39 is logarithmic in time [61, 63, 64, 67].
As shown in Equation 2.37 and Equation 2.2, the formation of PtOx and ORR are both simultaneously occurring at the catalyst surface, consequently the desired ORR is in competition with

the oxide formation and is negatively impacted by the oxidation process. But despite the efforts made to understand and describe the surface oxidation of Pt surfaces in PEM-FCs, no equation can be found in literature which describes $\eta_{|PtOx}$ explicitly. A few publications exist, in which an attempt to quantify the reversible voltage loss related to the formation of PtOx under PEM-FC-relevant conditions was made [54, 55]. Eckl et al. for example, used different conditioning voltages and a variety of time ranges for the formation of the surface oxides and determined the difference between the cell voltage of the oxide-free and the oxide-afflicted cathode-catalyst in a current range from 0 to 1.4 A/cm^2 [55]. Their results show on the one hand, that $\eta_{|PtOx}$ depends on the involved oxygen species (see Equation 2.37-2.39), as higher voltage losses are observed when the conditioning voltage is increased from 0.6 V to 0.8 V. With a further increase of the potential, a drop of $\eta_{|PtOx}$ is observed. This might be related to a buckling effect, as the lifted Pt-atoms might be able to participate in the ORR again. It was observed that the PtOx-related voltage loss depends on the current density, if the same conditioning procedure is used. In Figure 2.5 the measured reversible voltage losses for a conditioning voltage of 0.8 V and a hold-time of 1800 s are shown [55]. It can be seen, that the voltage loss depends on the current density. It increases from 20 mV at the lowest current to 90 mV at full load, where saturation can be observed. This kind of behavior of the PtOx-related overpotential was observed independently of the conditioning voltage (between 0.6-0.9 V) or its hold time (1-36.000 s) [55].

To explain the observed behavior shown in Figure 2.5, the following hypothesis is given by

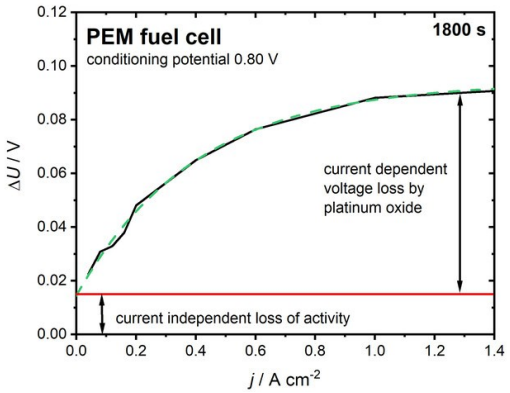

Figure 2.5: Measured voltage loss in a current density range from 0.04 to 1.4 A/cm^2 related to the formation of PtOx. The measured voltage losses for the different current densities were measured after a conditioning phase at 0.80 V for 1800 s. Reprinted with permission from Eckl et al. [55]. Copyright 2022 American Chemical Society.

Eckl et al.[55]. The offset performance loss of 20 mV can be related to the partial blocking of active sites. This coverage of active sites is the same independently from the current density, due to the PtOx conditioning of every load point. To explain the increase of performance loss with

increasing current density, an increase of Tafel slope was proposed and related to a shift of the reaction mechanism from the 4 e$^-$ (see Equation 2.2) to the 2 e$^-$ pathway,

$$O_2 + 2H^+ + 2e^- \rightleftharpoons H_2O_2, \tag{2.40}$$

$$H_2O_2 + 2H^+ + 2e^- \rightleftharpoons 2H_2O. \tag{2.41}$$

A correlation between the increase in Tafel slope and the formation of PtOx was also observed by Subramanian et al. [43]. In contrast to the study by Eckl. et al., the oxidation level of the catalyst surface was not aligned via an additional conditioning phase. Instead, a cumulative approach was taken, where the oxide coverage Θ was continuously increased depending on the cell potential. Figure 2.6 shows the resulting correlation of the measured oxide coverage and the Tafel slopes, determined with the polarization curves obtained by their cumulative approach. It can be seen,

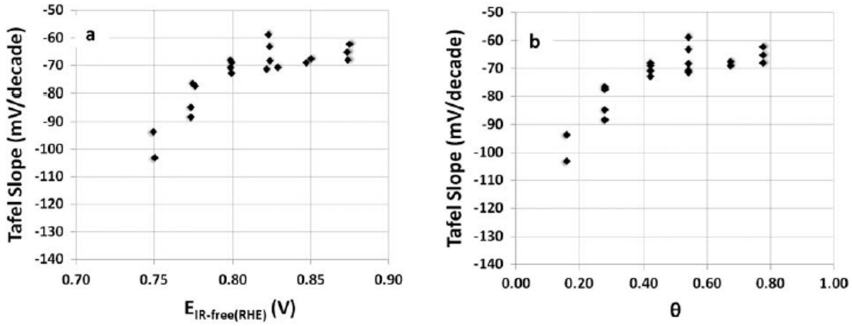

Figure 2.6: a) Development of the Tafel slope determined in [43] depending on the cathode potential $E_{IR\text{-}free}$ (IR-free: measured potential corrected by ohmic losses, see also Chapter 2.3.1 b) Correlation between Tafel slope and oxide coverage Θ. Used with permission of IOP Publishing, Ltd, from Subramanian et al. [43]; permission conveyed through Copyright Clearance Center, Inc.

that the Tafel slope increases with decreasing cell voltage respectively oxide coverage. At cell voltages higher than 0.8 V respectively an oxide coverage higher than 0.4 and an almost constant value of ~70 mV/dec is determined, which increases up to 104 mV/dec at 0.75 V (Θ= 0.16).
This observation is in line with the hypothesis, that the Tafel slope is influenced by oxide formation. Unfortunately, it is still under debate how oxide coverage and the interaction between Pt and oxygen containing adsorbates influences the ORR [43, 55, 70–73]. Consequently, it can not be answered unambiguously, if the increase of Tafel slope can be related to an alternative ORR mechanism.

2.3.6 Unassigned overpotential[1]

The last overpotential listed in Equation 2.14 is assigned to the limited cell performance at high current densities, which occurs especially for low catalyst loading on the cathode and aged MEAs [45, 53, 74–76]. So far, the origin of this overpotential is not identified, unambiguously (see Figure 2.3 red area).

Different authors assigned this overpotential to a further increase of the mass/oxygen transport resistance [45, 53, 74, 77]. Greszler et al. used cathode catalyst layers with the same carbon material and thickness, but varied the Platinum loading in the range from 0.4 down to 0.03 mg_{Pt}/cm^2 and analyzed the oxygen transport resistance of these electrodes. In this study they concluded, that the total oxygen transport resistance in the electrodes is caused by the diffusion through the electrode pores (through plane) and from an unknown transport-like resistance, which scales inversely with ECSA and can be mathematically interpreted as a thin transport-resistive ionomer film covering the catalyst particles. In their study, the value of this resistance is ~12 s/cm [2]. Such a high resistance would lead to a significant loss of oxygen partial pressure for low loaded cathodes and could explain the high performance loss at high current densities [45].

Owejan et al. expanded the study of Greszler et al. by using diluted electrodes and electrodes, which were produced by using at least one or more catalyst powders with lower Pt loading. With this approach they produced electrodes with the same loading and the same thickness, but differing distribution of platinized carbon particles. In their study they showed not only that the mass transport resistance increases for lower loaded cathodes, but also that the distribution of the platinum particles had a significant influence on the mass transport resistance. With these findings they came to the conclusion that the unassigned voltage losses at high current densities could be mitigated, if the oxygen flux through the gas / ionomer interface to the Pt surface is minimized by a proper electrode design [76].

Besides the mass transport resistance approach, some authors linked the unassigned overpotential to a changed reaction mechanism at sufficiently low half cell voltages (see also Cha. 2.3.2) [43, 73]. Doubts about the reaction-mechanism hypothesis mainly arise from the harsh increase of the Tafel slope up to several hundreds of mV at high current densities observed in Refs. [44, 76]. These slopes are much steeper than the slopes normally reported in literature for a changed reaction mechanism (up to 140 mV/dec) [43, 70, 78, 79]. Oppositely, the experimentally observed R_{mt}-increase could never be strictly linked to these unassigned losses, as an increase would be required that seems far too large to explain the unassigned voltage loss.

[1] Parts of this chapter has been published in D. Bernhard, T. Kadyk, U. Krewer, and S. Kirsch, "How platinum oxide affects the degradation analysis of PEM fuel cell cathodes," International Journal of Hydrogen Energy, vol. 46, no. 26, pp. 13 791–13 805, 2021 [54].

[2] Greszler et al. explicitly disregard a physical interpretation of this resistance beyond its functional behavior; Measurement conditions: 80 °C and ~62 % RH [45].

2.4 Degradation in PEM-FCs

In automotive applications PEM-FCs are used in a wide range of operation conditions [4, 80]. The normal operating window is within a temperature range of 60 to 80 °C, a relative humidity range of 80 to 100 % and voltage range of 0.6 up to 0.9 V [81, 82]. In Figure 2.7 a simplified voltage profile occurring in a PEM-FC drive cycle is shown. It is characterized by the dynamic operation of the PEM-FC, which involves frequent changes in voltage and current density. The profile shown only visualizes the voltage changes, as realistic drive cycle profiles can be much more dynamic.

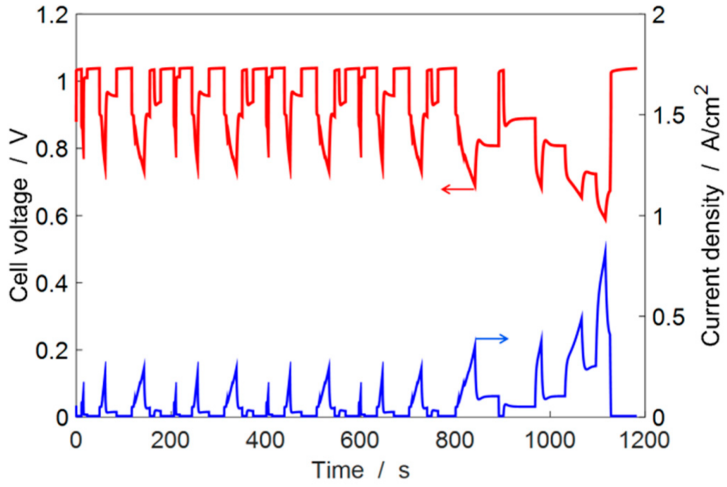

Figure 2.7: Exemplary voltage respectively current density profiles derived from from the New European Driving Cycle (NEDC) requirements according to Mayur et al.[83].

Besides driving, further operation scenarios like Shut-Down (SD) and Start-Up (SU), idling at the OCV and fuel starvation can occur. Depending on the current operation conditions of these scenarios the different PEM-FC components, introduced in Chapter 2.1, can suffer from degradation. In the following chapters the different operation conditions and their related degradation phenomena are introduced.

2.4.1 Degradation of PEM-FC components except catalyst layer

In Table 2.1 - 2.3 the main degradation mechanism for the bipolar plates, the gas diffusion layer and the membrane of PEM-FCs are summarized. As this work is focused on the degradation of PEM-FC cathodes, the conditions and the related degradation phenomena of the BPP, the GDL and the membrane are reduced to the main aspects influencing the overpotentials introduced in Chapter 2.3 and the interactions of the different degradation mechanisms are not shown. More detailed information about these degradation processes and their mutual influence are given in numerous reviews and publications [4, 20, 80–82, 84–89].

Table 2.1: Overview of BPP degradation in PEM-FCs under various operation conditions.

BBP degradation			
Operation Conditions	**Degradation Mechanism**	**Effect**	**Influence on Performance**
Driving conditions	Electrochem. reactions	oxide formation (cathode) / corrosion (anode)	increase of contact resistance causes an increase of η_{HFR}
SU/SD Fuel starvation	carbon corrosion	erosion	

Table 2.2: Overview of GDL degradation in PEM-FCs under various operation conditions.

GDL degradation			
Operation Conditions	**Degradation Mechanism**	**Effect**	**Influence on Performance**
Driving conditions	Material dissolution	Surface oxidation & Loss of PTFE	wettability changes causing flooding, resulting in an increase of R_{mt} and an increase of η_{mt}
SU/SD	Carbon corrosion Freezw Thaw	Surface oxidation Loss of PTFE	
Idle	Radical attack	Surface oxidation & Loss of PTFE	
Driving conditions	Compression Erosion by fluid	Fiber breakage loss of carbon	Structural changes up to collapse of the porosity resulting in an increase of R_{mt} and an increase of η_{mt}
SU/SD	Carbon corrosion Freeze Thaw	Loss of carbon Fiber breakage	
Idle	Radical attack	Surface oxidation & Loss of carbon	

Table 2.3: Overview of membrane degradation in PEM-FCs under various operation conditions.

Membrane degradation			
Operation Conditions	**Degradation Mechanism**	**Effect**	**Influence on Performance**
High Cell Voltage (OCV) High Temperature Low RH	Radical attack	Membrane thinning Pinholes & Cracks	Increasing crossover of H_2 causing a additional performance loss
RH cycling	Mechanical stress	Pinholes & Cracks	

2.4.2 Degradation of cathode catalyst layer

In contrast to the degradation of the different PEM-FC components introduced in Chapter 2.4.1, the degradation of the cathode catalyst layer is the dominant source for performance losses within a PEM-FC lifetime, especially the loss of ECSA and the change of catalyst activity, if alloy materials are used (see Chapter 2.4.2.3) [44, 90–94]. In Figure 2.8 the mechanisms which can cause a

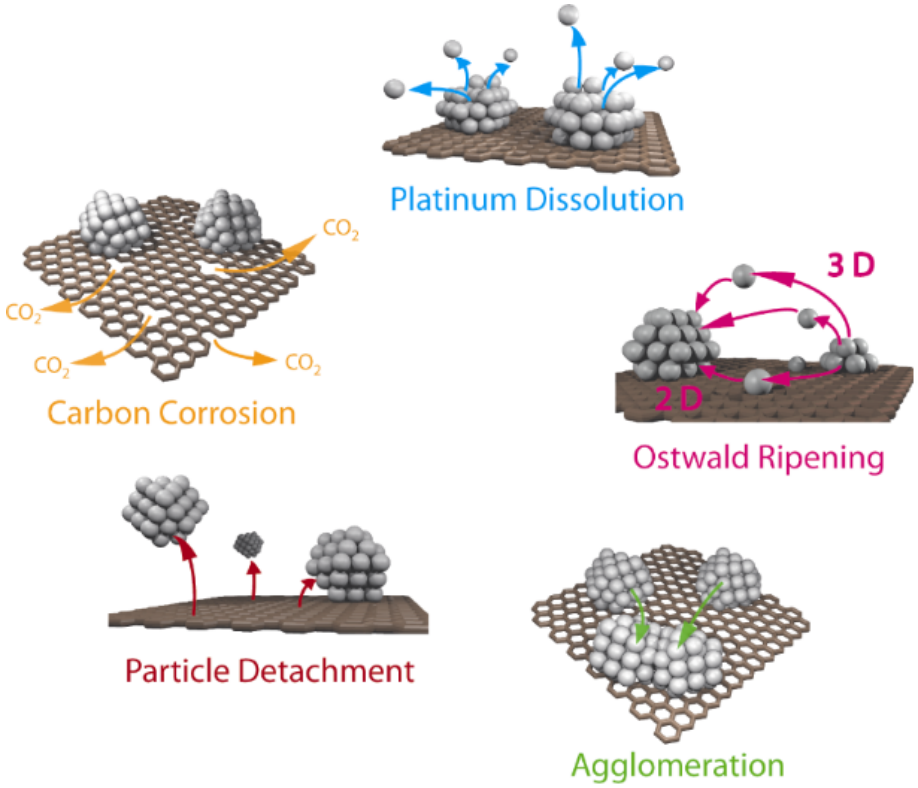

Figure 2.8: Simplified visualization of the different degradation mechanisms for Pt/PtCo-particles on a carbon support in PEM-FCs. The overview was adapted from [95], copyright Meier et al., licensee Beilstein Institut.

loss of ECSA are shown. Why these degradation phenomena can occur within the operation of a PEM-FC and how they influence the cell performance is explained in Chapter 2.4.2.1 and 2.4.2.2. In Chapter 2.4.2.3 the influence of PEM-FC operation on alloy catalyst and the influence of the degradation for this kind of catalysts on the activity are discussed.

2.4.2.1 Platinum dissolution

In the upper part of Figure 2.8 the process of platinum dissolution is shown schematically. During the dissolution process, Pt atoms are dissolved from the catalyst particle. This process is linked to alternating operations at low and high loads, which correspond to high and low cathode potentials. This results in an iterative process of surface oxidation and reduction of the catalyst nanoparticles within a PEM-FC drive cycle (see Figure 2.7 and the Start-Up / Shut-Down [4, 96–98]. An unambiguous prove for the dissolution of Pt within this PEM-FC operation is redeposition of platinum in the membrane, as the H_2-Crossover reduces dissolved Pt-ions [99–101].
A deeper understanding of the dissolution behavior of Pt and Pt-alloy catalysts is gained by connecting electrochemical flow cell systems to an inductively coupled plasma mass spectrometer (ICP-MS) capable of on-line quantification of even small traces of dissolved elements in solution [98, 102–105]. By using different potential profiles, this setup allows to determine the potential dependent dissolution behavior of platinum. In general, triangle and square wave (TW and SW) potentials with flexible lower and upper potential limits (LPL resp. UPL) were used in these experiments (see Figure 2.9). Based on these experiments, a two fold transient dissolution process is derived. In the anodic branch of the voltage cycle (LPL →UPL, see Fig 2.9) dissolved Pt

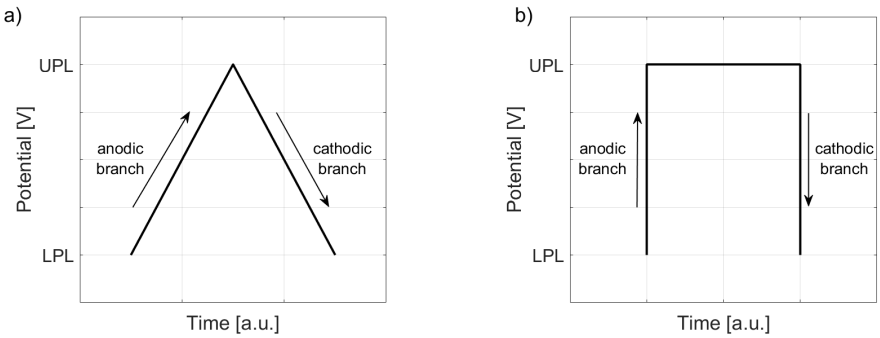

Figure 2.9: Schematic draft of a triangle and a square wave potential profiles. For a detailed analysis of platinum dissolution, various profiles with different lower and upper potential limits, scan rates and hold times at the UPL and LPL are used [98, 102–104].

can be detected at a potential of 0.8 V respectively 0.85 V for PtCo respectively Pt nanoparticles [98, 103]. This dissolution is often related to the direct electrochemical dissolution mechanism [80, 102–104, 106, 107]

$$\mathrm{Pt} \rightleftharpoons \mathrm{Pt}^{2+} + 2\mathrm{e}^{-}. \tag{2.42}$$

Most recently, simulations by Duan et al. lead to the conclusion, that the anodic dissolution is related to the dissolution of Pt-hydroxides resulting in a solvated Pt-ion complex [108],

$$Pt(OH)_2 + 2H_2O + 2H^+ \rightleftharpoons [Pt(H_2O)_4]^{2+}. \tag{2.43}$$

The anodic dissolution can be related to the dissolution of low coordinated surface facets, like edges or defects in the crystal structure [75, 109]. The anodic platinum dissolution is accelerated with increasing UPL, but slowed down at potentials higher than 1.0 V. This observation is related to surface oxide formation (see also Chapter 2.3.5) at these potentials, which passivates the platinum surfaces and stabilizes the Pt particles against further dissolution [75, 98, 103]. Consequently, anodically dissolved amount of Pt is limited by the oxidation process [80, 102–104, 106, 107]. In the cathodic branch of the voltage cycle (UPL →LPL, see Figure 2.9) dissolved Pt can be detected if a UPL of 0.9 V respectively 0.95 V for PtCo respectively Pt nanoparticles is reached [98, 103]. This observation is linked to the reduction of the surface and subsurface oxides [80, 98, 102–104, 106, 107].

$$PtO + 2H^+ \rightarrow Pt^{2+} + 2H_2O \tag{2.44}$$

and

$$PtO_{sub} + 2H^+ + 2e^- \rightarrow Pt^{2+} + 2H_2O. \tag{2.45}$$

Where the amount of dissolved Platinum increases with increasing UPL, hold time at UPL and decreasing LPL [98].
The anodic and cathodic dissolution of the Pt nanoparticles results in a reduction of the electrochemical active surface area (ECSA) [37, 44, 75, 80, 93, 94, 98, 106, 107]. This loss of ECSA is related to two different phenomena. The first phenomenon is the so called Ostwald ripening. The "electrochemical Ostwald ripening" is characterized by the preferential dissolution of smaller Pt particles, due to their higher surface energy compared to bigger particles and the following redeposition of the dissolved Pt species on the more stable larger particles (see Figure 2.8) [93–95, 107]. The second phenomenon is the precipitation of the dissolved Pt within the electrolyte and the membrane, proven by the already mentioned Pt-band formation [93–95, 107] [82, 93].
The anodic dissolution is the main reason for ECSA losses under driving conditions and cathodic dissolution dominates the ECSA loss at Shut-Down and Start-Up, idling at the OCV and fuel starvation. The loss of ECSA increases the overpotential related to the cathode activity (see Equation2.21) and consequently reduces performance and longevity of the PEM-FC.

2.4.2.2 Carbon corrosion

Besides the ECSA losses due to dissolution, the degradation of the carbon support can lead to further losses of ECSA. These losses are related to the oxidation of the carbon support, commonly known as carbon corrosion. Theoretically, the corrosion of the carbon support occurs at potentials higher than 0.207 V_{RHE} [95, 110–113]:

$$C + 2H_2O \rightarrow CO_2 + 4H^+ + 4e^- \quad (0.207 V_{RHE}, 25\,^\circ C) \tag{2.46}$$

and

$$C + H_2O \rightarrow CO + 2H^+ + 2e^- \quad (0.518 V_{RHE}, 25\,^\circ C) \tag{2.47}$$

$$CO + H_2O \rightarrow CO_2 + 2H^+ + 2e^- \quad (-0.103 V_{RHE}, 25\,^\circ C) \tag{2.48}$$

Consequently, the oxidation of the carbon support can already occur at operation conditions of a PEM-FC. However, due to sluggish reaction kinetics, the carbon corrosion rate remains low under these conditions, and the resulting carbon loss over the PEM-FC lifetime has minimal impact on overall cell performance [44, 96, 110, 114–116]. The carbon corrosion rate is mainly driven by high cell voltages and corresponding electrode potentials above 1 V. An increase in carbon corrosion rates directly raises the oxidation level of the cathode catalyst support, leading to the migration and subsequent coalescence of catalyst particles on the support surface (see Figure 2.8). Furthermore, the catalyst material can detach (see Figure 2.8) from the carrier, due to a reduced attachment to the carbon material and potentially resulting in the complete loss of the carbon support [44, 93, 96, 110, 114, 115, 117]. These further ECSA-reducing degradation mechanisms can occur significantly within Start-Up and Shut-Down processes, respectively if local fuel starvation occurs, as under these conditions, local electrode potentials higher than 1 V are reached [40, 97, 117, 118].

Besides the loss of ECSA, high carbon corrosion rates can lead to a loss of the pore structure of the support material. This structural breakdown of carbon material can increase the mass-transport resistance and consequently reduces the cell voltage according to Equation 2.32. In a more severe case, the collapse of the catalyst support blocks the transport of oxygen in parts of the cathode, causing a deactivation of these particles and can be described as a massive loss of ECSA, which increases η_{act} (see Equation 2.21) [114].

2.4.2.3 Dealloying effects

Pt-Alloy catalysts are used in PEM-FC automotive applications, as they offer two decisive advantages. On the one hand, the use of Pt-alloys allows the partial substitution of precious platinum with more economically priced metals, leading to the formation of core–shell particles — metallic cores coated with a thin platinum shell. On the other hand, it is even possible to increase the ORR activity of the catalyst, if transition metals like Cobalt, Nickel or Palladium are used as alloy materials [119–123].
The activity enhanced properties of Pt-alloy nanaoparticles is based on the weakened interactions of the catalyst with the oxygen-containing ORR intermediates like OH, as the electronic property of platinum is alternated due to the interactions with the transition metal [121, 124–126]. One reason for this change in electronic property of the platinum is the charge transfer between the transition metal atom and the platinum atom in direct vicinity, due to differences in electronegativity, known as the ligand effect. By donating electrons the ligand, fills up antibonding states in the Pt d-band. This causes a negative shift of the d-band centers of the platinum relative to the Fermi level, and weakens the adsorption of hydroxyl species like OH_{ads}. Combined with a reduced coverage of the active sites of the catalyst in these molecules compared to a pure platinum nanoparticle, the ligand effect increases the ORR activity of the Pt-alloy particle [127–131].
The other reason for the observed increase in activity of Pt-M catalysts is the so called strain effect. This effect is caused by the lattice mismatch between the platinum and the alloy material and causes a compression of the Pt-Pt interatomic distance and a lowering of the Pt d-band center. With increasing amount of the alloy, the Pt-Pt inter-atomic distance is further decreasing and more strain is induced in the platinum shell, correlating with a further reduction of the d-band center. This strain effect also causes a weakened binding of hydroxl species to the active sites of the catalyst material, inducing an enhanced electrocatalytic activity for the ORR of the Pt-M particles [119, 127, 127, 129, 132].
In general, these two effects can not be deconvoluted and appear simultaneously. But as the most common alloy catalyst used in PEM-FC consists of core-shell structured Pt-M nanoparticles, the ORR activity of the alloy catalyst is enhanced by the ligand effect when the particles feature a pure Pt skin — that is, when the alloy core is covered by a monolayer of Pt atoms. In most applications the nanaoparticles have several layers of Pt-atoms covering the alloy core. Consequently, the ORR activity increase of these catalysts is based on the strain effect [124–126].
One of the most commercially used alloy catalysts in PEM-FCs is Platinum-Cobalt Pt_3Co, especially common as cathode material [16, 17, 122, 133, 134]. For example the ORR in the Toyota Mirai is driven by a PtCo catalyst to fulfill the performance and longevity requirement for PEM-FC vehicles [16].
Different studies show that the alloy catalysts lack long-term stability, as the added non-precious

metal suffers from dissolution effects [98, 122, 133–137]. Ahluwalia et al. analyzed the dissolution behavior of a PtCo catalyst with an electrochemical flow cell system coupled with an on-line ICP-MS. With this setup they were able to detect dissolved Co under PEM-FC like operation conditions. Dealloying was performed in a 1.0 M perchloric acid electrolyte and by applying different staircase and triangle potential profiles to the catalyst. Generally speaking, dissolved Co was detected at all potentials higher than 0.1 V, where distinct Co dissolution peaks could be detect in cathodic sweeps with an UPL higher than 0.6 V and in the anodic sweep at UPL higher than 0.7 V. If the UPL is equal or higher than 0.9 V, the difference between dissolved amount of Co in the anodic and the cathodic branch of the profile can be neglected. They concluded, that the observed accelerated Co dissolution at these high potentials is related to the reduction of the formed surface oxides (see also Chapter 2.3.5). The reduction and subsequent dissolution of Pt exposes Co in the sub surface layer of the catalyst particle and causes Co dissolution. The detected amount of dissolve Co increases with increasing UPL and decreasing LPL [98].
This study shows, that this kind of alloys are not stable over the full life time of a PEM-FC. In various other publications the influence of the Co dissolution on the composition and the activity of the alloy particles is analyzed [122, 133–137]. Dubau et al. analyzed the compositional changes of PtCo catalyst during long term PEM-FC operation, by using advanced analysis methods like X-ray diffraction (XRD) measurements and transmission electron microscopy (TEM) imaging, Raman spectroscopy and X-ray energy dispersive spectroscopy (X-EDS) [122, 134]. With this approach, they were able to determine the Pt:Co atomic ratio, the particles size, and the shape and fraction of agglomerated metal particles. Their studies show, that the degradation of the alloy material starts with the dissolution of the surface Co atoms within the first hours of operation, causing the build up of a Pt-enriched shell covering the alloy core. With ongoing operation of the PEM-FC stack, the atomic ratio Pt:Co increases continuously and due to surface segregation the Co content in the particle bulk decreases. Based on their results, they concluded that the dealloying process causes not only a changed structure of the catalyst particle (PtCo alloy particles converted to Pt-enriched / Pt-Co core particles), but also the depletion of Co in the particle core. The development of the Pt-enriched / Pt-Co core particles is driven by the dissolution of Co, while the segregation of Co might homogenize Co atoms distribution in the alloy core and the Pt-enriched shell [122, 134, 138]. In parallel to the loss of the alloy material, the dissolution of Pt takes place [98, 137, 139, 140], and as described in Chapter 2.4.2.1, dissolved Pt tends to deposit on the larger catalyst particles via the Ostwald Ripening effect. This process increases the Pt shell of the particles to several layers of pure Pt around the depleted alloy core.
The dealloying process of a PtCo particle is shown schematically in Figure 2.10. It starts with the dissolution of Pt and Co atoms from the shell of the pristine PtCo particle (Figure2.10a-b). As soon as parts of Pt shell are completely dissolved, also Co atoms from the core dissolve (Figure2.10c-d). In parallel redeposition of the solved Pt atoms on the particle surface occurs (Figure2.10d). This degradation process causes the change of the pristine alloy particle into a

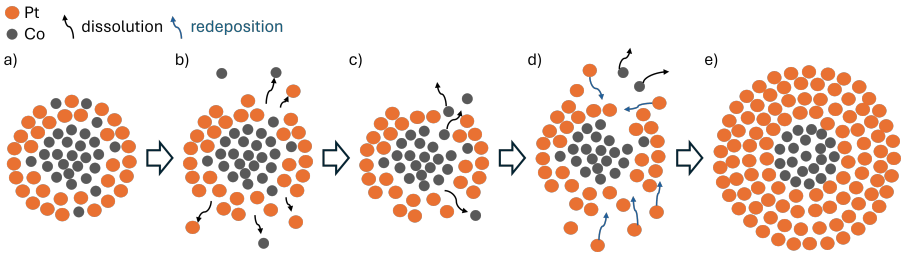

Figure 2.10: a) Pristine PtCo particle with a Co core and a few Co atoms in the Pt shell b) Dissolution of Pt and Co atoms from the shell c) Dissolution from Co atoms from the core d) further dissolution of Co atoms and redeposition of dissolved Pt e) PtCo particle with a decreased Co core and a thicker Pt shell.

particle with decreased alloy core and thickened Pt shell (Figure2.10e). Besides the shown core-shell nanoparticles, with an enriched Pt-rich shell and a Co-depleted core, observation of PtCo particles with a hollow like structure and really small amount of Co atoms left in the particles and even hollow Pt particles with no detectable residues of Co in the particle can be found in dealloying related literature [122, 140].

Due to this dealloying related changes of catalyst particle structure, the activity enhancing strain and ligand effect of the alloy material on the Pt surface is at least reduced or even nullified. Compared to a pure Pt catalyst, the ORR activity not only decreases due to the loss of active centers through the loss and growth of the catalyst particles, but the specific activity of the material also decreases, so that the conversion rate of the ORR decreases [123, 137, 139, 140].

Besides the performance loss induced by the dealloying related structural changes of the alloy particles, deallyoing within the lifetime of a PEM-FC can have another negative effect on the cell performance and consequently on the longevity if the PEM-FC. With an estimated redox potential of -0.18 V the reduction of leached out Co^{2+} is thermodynamically unlikely in the operation range of a PEM-FC [140]. Consequently, Co^{2+} ions can be found in the CL ionomer and the membrane and will interact with H^+ transporting SO^{3-}-groups of the ionomer. This ionomer contamination can lead to significant voltage losses especially at current densities higher than 1.5 A/cm^2 [15, 140–143]. This loss might be related to an increase of R_{HFR} and R_{H^+}. A significant increase was measured by Ramaswamy et al. under dry conditions (RH 50 %). They attributed a performance loss of 52 mV at 2.5 A/cm^2 to Co^{2+} contamination caused by dealloying even under wet conditions (RH 100 %) [141]. But how dissolved alloy cations influence the cell performance within a PEM-FC lifetime is still not unambiguously answered and needs further studies under different operation conditions [37, 140].

2.4.3 Accelerated stress testing

The different degradation mechanisms explained in chapter 2.4 must be considered, to determine the longevity of PEM-FC systems. The single components of a PEM-FC have to fulfill the lifetime requirements of PEM-FCs (see Chapter 1). Consequently, the PEM-FCs must be analyzed under all possible operation conditions. This can be done by simulating real lifetime conditions of PEM-FCs vehicles on a test bench. But with run times up to 5000 h, this kind of durability testing is too time consuming for the evaluation of new materials [144].
Consequently, accelerated stress tests (ASTs) are needed, which cause degradation of the different fuel cell components and materials in a reasonable time [86, 144–148]. As the cost of a PEM-FC stack is still governed by cathode catalyst costs, its degradation has gained special interest in the literature. Numerous AST protocols have been published which are based on the platinum dissolution AST published by the U.S. DOE (see Figure 2.11). This protocol consists of

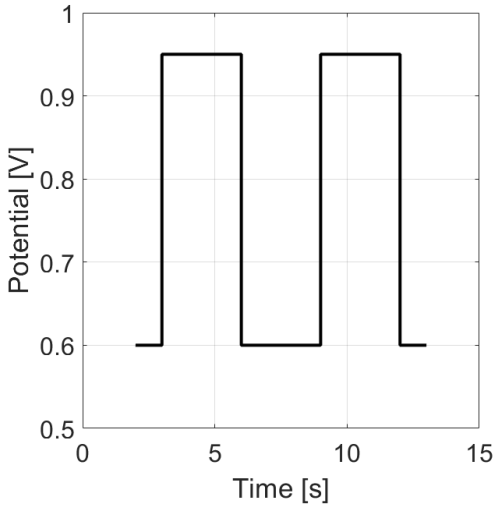

Figure 2.11: Schematic snippet of the platinum dissolution AST defined by the U.S. DOE [146].

a square wave profile between a lower potential limit of 0.6 and an upper potential limit of 0.95 V, both held for 3 seconds, whilst a controlled atmosphere of hydrogen at the anode and nitrogen at the cathode at atmospheric pressure level is maintained. Further parameters of the AST include a temperature of 80 °C and a relative humidity of 100 % at both electrodes. According to this protocol 30,000 of these AST cycles must be obtained, within these cycles the polarization curves and the ECSA are measured at a defined number of cycles [146]. In Table 2.4 all the required metrics, the measurement sequence and the targets of the AST protocol specified by the U.S.

DOE are given. Numerous variations of the basic AST-cycle can be found in literature, in these

Table 2.4: Measurement procedure, metrics and targets of the platinum dissolution AST according to the U.S. DOE [146].

Metric	Frequency	Target
Catalyst mass activity	At begin and end of test, minimum	< 40% loss of initial catalytic activity
Pol. curve from 0 to 1.5 A/cm^{-2}	at 0, 1000, 5000, 10000, and 30000 cycles	<30 mV loss at 0.8 A/cm^{-2}
ECSA	at 10, 100, 1000, 3000, 10000, 20000, and 30000 cycles	<40% loss of initial area

ASTs the different parameters (LPL, UPL, hold time at LPL and UPL, T, RH) were changed and variyng gas compositions at the cathode (H_2 / O_2 / air) were applied [44, 54, 91, 98, 106, 149–151]. Another type of cathode catalyst AST for PEM-FCs are different types of triangle wave ASTs, trapezoidal and combinations of the introduced AST types [44, 106, 144, 149].

2.5 PEM-FC degradation and performance loss modeling approaches [3]

A variety of accelerated stress tests (ASTs), like triangular wave or square wave ASTs, are used in literature to produce an electrode state close to the end-of-life (EoL) state targeted in LDV or HDV applications. In a number of works, different stressors, controlled by the operating parameters of the AST, such as potential, waveform, hold times, temperature and relative humidity on catalyst degradation are studied [42, 54, 91, 152, 153]. Such data is specifically relevant for the development and validation of degradation models of PEM-FCs.
Generally, the variety of different degradation model approaches can be divided into empirical approaches, physical approaches and hybrid approaches combining empirical and physical equations. Furthermore, the field was widened and diversified by the advances in artificial intelligence, specifically the development of neural networks or advanced machine learning [154–158]. A summary of models that make use of artificial intelligence like neural networks or machine

[3] Parts of this chapter has been published in D. Bernhard, T. Kadyk, S. Kirsch, H. Scholz and U.Krewer, "Model-assisted analysis and prediction of activity degradation in PEM-fuel cell cathodes," Journal of Power Sources, vol.562, p.232771 [150].

learning is given in [116, 159, 160]. These models gain their predictive capabilities from analyzing large sets of data [158, 159]. But as large amounts of degradation and performance data are rare, the applicability of these approaches is limited. Further empirical approaches dealing with degradation and performance losses in PEM-FCs can be found in literature [161–166]. For example, Chen et al. [162] assigned data from fuel cell buses to four alternative operating modes. For these operating modes, the voltage loss per start-stop- and load-change-cycles or per hour for idling and high power load phases is determined. By summing up these losses, the performance loss can be predicted. With this approach, Chen et al. were able to predict the voltage loss for their PEM-FC stack for arbitrary drive cycles. However, the applicability to other PEM-FC systems or operating conditions lacks generalizability. The model proposed by Messing et al. [166] used a start-stop-AST and a load-cycling-AST with harsh conditions. They derived two equations to describe the voltage loss caused by the two distinct ASTs. Then, they deconvoluted drive cycles into a series of start-stop and load-cycling-ASTs. This approach enables the prediction of run-time under different drive cycle scenarios until 90 % of the starting voltage at 0.6 A/cm^2 is reached. Unfortunately, the impact of changes in temperature, relative humidity and pressure is not considered, even though these operating conditions can have a significant influence on the cathode degradation [141, 152, 167–171].

In contrast to empirical models, physical-mathematical models are used to describe changes of the cathode catalyst [90, 142, 152, 170, 172–176]. For example, Holby et al. derived a kinetic platinum dissolution model to describe ECSA losses. These losses are related to a change of the particle size distribution (PSD) [172]. Li et al. refined this model by adding Ostwald ripening and platinum precipitation in the ionomer and the membrane [175]. A further model that uses the PSD changes to predict ECSA losses is derived by Schneider et. al. [152]. Their model accounts for Pt in the membrane, Ostwald ripening, the loss of catalyst particles caused by carbon corrosion and the loss of platinum due to the formation of subsurface oxides at potentials of $>$1.1 V. Further PSD-based degradation models can be found in [90, 142, 170, 176–180]. While these models are very useful to describe one part of catalyst degradation, namely ECSA loss, to the best of our knowledge, no physical models exists to describe the other part, namely losses of catalyst activity (measured by Tafel slope and exchange current density). Naturally, the derivation of cell voltage losses based on Tafel kinetics lacks precision when only ECSA losses are considered. This leads to the faulty prediction of an independence between voltage loss and current density, which does not pass experimental scrutiny [42, 44, 75].

Alternatively, catalyst degradation and linked voltage losses can be described with semi-empirical approaches [81, 91, 181–184]. For example, Moein-Jahromi et al. used an empirical model approach to describe the decay of ECSA, which is based on a first order ECSA decline rate. This loss of active surface is converted into a PSD, to derive the surface for oxygen diffusion through the ionomer film surrounding the catalyst particles. In addition, they developed a physics-based performance prediction model, which uses ECSA and the surface for oxygen diffusion as input parameters [185]. Another semi-empirical approach is presented by Kneer et. al. [91]. They

derived an empirical ECSA loss model, based on a first order kinetic approach, that is capable to predict the ECSA-loss for a wide range of AST parameters. These losses are then used as input for their performance loss prediction model that is based on simple Tafel kinetics. This model enables the prediction of the voltage loss up to a current density of 1.5 A/cm^2 reasonably. However, again the dependence on current density is lacking as a consequence of ignoring the changes in the other kinetic parameters.

For the design of durable fuel cell systems, models which allow the prediction of degradation related performance losses under drive cycle scenarios and related operating conditions, are needed. A possible approach is to convert drive cycles into an equivalent series of accelerated stress tests. Accordingly, the main objective of this work is to enable the performance loss prediction for accelerated stress test under various operating conditions like voltage profile or temperature.

One suitable model, capable to predict the loss of the electrochemical active surface area and the related performance losses for pure platinum catalysts aged with accelerated stress test with various operating conditions is the one presented in [91]. This thesis extends this approach by enabling predictions of Tafel slope, exchange current density and consequently the calculation of current dependent performance losses in PEM fuel cells for a PtCo catalyst.

The first part of the model is formed by a statistical-physical model for particle radius distribution evolution and ECSA loss [173]. The model is extended to account for the impact of the most important AST-parameter dependencies. By analyzing the experimental data, correlations were found between the ECSA-loss on the one side, and Tafel slope as well as specific exchange current density on the other side. These observed changes of Tafel slope and specific exchange current density are related to the different catalyst degradation mechanisms like dealloying and changes in the distribution of the crystal facets. The second part of the model is based on an extended Tafel-kinetic approach that accounts for these correlations and allows the prediction of cell voltage losses. After global parametrization, the model reproduces the voltage losses, measured in a current density range of 0.0-2.0 A/cm^2 with an accuracy of 7.1 mV.

3 Experimental [1]

In this chapter, the PEM-FC single cell setup and the experimental approach are introduced. To gather the necessary degradation data, a general testing sequence is derived. This sequence consists of a dedicated diagnostic procedure, which is used in a variety of accelerated stress tests. This approach allows to measure the decisive cathode and membrane properties within different degradation protocols. These are needed to determine the overpotentials introduced in Chapter 2.3. The obtained data are used in the Chapters 4 and 5.

3.1 Experimental setup

Experimental data were gathered using a 5 cm^2 MEA-design based on the studies of Baker and Caulk [49]. The water cooled gas flow field has an area of 50 cm^2, where the active MEA area of 5 cm^2 is arranged at the gas outlet of the flowfield (see Figure 3.1).

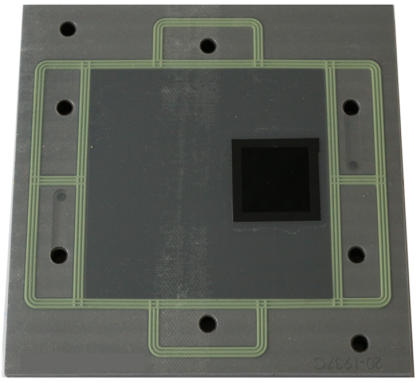

Figure 3.1: Flow-field with used GDL and 5 cm^2 MEA.

[1] Parts of this chapter has been published in D. Bernhard, T. Kadyk, U. Krewer, and S. Kirsch, "How platinum oxide affects the degradation analysis of PEM fuel cell cathodes," International Journal of Hydrogen Energy, vol. 46, no. 26, pp. 13 791–13 805, 2021 and D. Bernhard, T. Kadyk, S. Kirsch, H. Scholz and U.Krewer, "Model-assisted analysis and prediction of activity degradation in PEM-fuel cell cathodes," Journal of Power Sources, vol.562, p.232771 [54, 150].

A cathode loading of 0.25 mg_{Pt}/cm^2 PtCo catalyst with a Pt:Co molar ratio in the raw powder of 70:30, an un-alloyed Pt anode with a loading of 0.05 mg_{Pt}/cm^2, an ionomer with a low equivalent weight and a persulfonic acid based membrane with a thickness of 18 µm were used. For gas diffusion layers Sigracet 25BC were used on both sides, compressed with a pneumatic hardware to a compression in the active area of 1 MPa. All electrochemical data and operating conditions were gathered with a fully automatized single cell test bench from Horiba FuelCon GmbH and an additional external potentiostat (Zahner Zennium).

3.2 Test sequence

The basic test sequence is shown in Figure 3.2a. It begins with a conditioning procedure, consisting of several step changes in current and voltage, to activate the MEAs. Afterwards, the MEAs were characterized at begin of life (BoL) with a developed diagnostic procedure, containing cyclic voltammetry to determine the ECSA and an extended polarization curve measurement between 0-2.0 A/cm^2 (see lower part of Figure 3.2). This polarization curve measurement in-

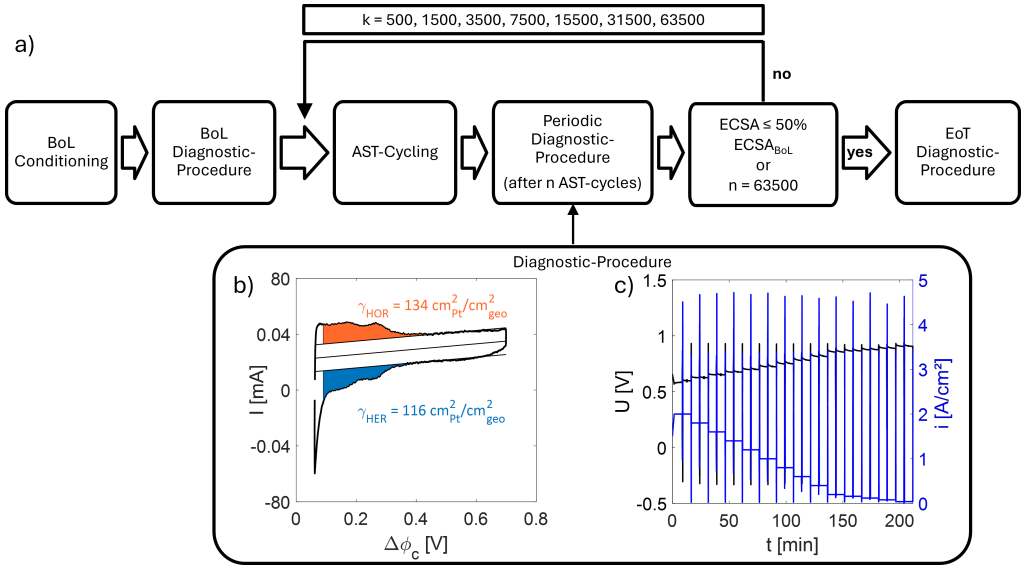

Figure 3.2: a) Schematic representation of the test sequence described in Chapter 3.2. The diagnostic procedure contains cyclic voltammetry (b) and an extended polarization curve measurement with limiting current and electrochemical impedance spectroscopy measurements (c). A detailed description of the diagnostic procedure is given in the following chapter. For the degradation of the MEAs different square wave potential ASTs are used (see Table 3.2). The degradation processes were interrupted after a defined number of AST-cycles k (k=500, 1500, 3500, 7500, 15500, 31500 and 63500) and the diagnostic procedure was repeated. The tests were stopped, if 50 % of the initial ECSA was lost or 63500 cycles were obtained.

cludes limiting current measurements and electrochemical impedance spectra at every load point to determine R_{mt} respectively, R_{HFR} and R_{H^+}. A detailed description of this procedure is given in the following chapter. After the BOL characterization, the MEAs were degraded with different ASTs. These ASTs were interrupted at a defined number of AST-cycles k (k = 500, 1500, 3500, 7500, 15500, 31500, (63500)) to determine the MEAs properties during the degradation test. The ASTs were terminated upon reaching either a 50 % loss of ECSA or 63,500 cycles, and the test sequence concluded with the end of test diagnostic procedure.

3.3 Diagnostic procedure

Figures 3.2b-c and 3.3 show the developed diagnostic procedure. It starts with determining the ECSA using cyclic voltammetry (Figure 3.2b). The CVs were recorded with a *Zahner Zennium* between 0.06 and 0.7 V with a H_2-atmosphere on the anode and N_2-atmosphere on the cathode and a scan-rate of 20 mV/s. They were recorded to derive ECSA and the H_2 crossover [42, 44]. The electrochemical surface area was obtained by averaging the hydrogen-desorption and hydrogen-adsorption charge using a specific charge of 210 C/cm_{Pt}^2. After the CV, the diagnostic procedure shown in Figure 3.3 was run with a cell temperature of 80 °C, H_2/air flows of 5 Nl/min, an inlet pressure on both sides of 2.0 bar and a relative humidity of 100 % at the cell inlet. These operation conditions ensure that cell temperature, pressure and relative humidity can be assumed to be constant over the active area of 5 cm^2 and so-called differential conditions are achieved. The diagnostic procedure consists of 13 different measurement periods of 15 min, each belonging to a specific current density between 0 and 2.0 A/cm^2 (see Figure 3.3a). In each period different "diagnostic tools" contained in three phases are used to extract the desired cell properties. In Phase I, the cell is conditioned for 7.5 min at the desired current density to set up the liquid water profiles (in-plane and through-plane) in the MEA (Figure 3.3b). In Phase II (Figure 3.3c), one potentiostatic and nine galvanostatic steps are carried out. Thereby, during the first step a voltage of 0.2 V is held for one second and the average current density is measured. Afterwards the steady state current density of Phase I is held again for 1 second, followed by nine galvanostatic steps. During these steps the current density, measured during the potentiostatic step, is increased step-wise to obtain even lower voltages. Throughout each of these steps the high current densities are maintained for 1 second, followed by a 1 second hold at the steady state current density of Phase I. The purpose of this sequence is two-fold. On the one hand, the low voltages involved lead to a complete reduction of PtOx. On the other hand, the R_{mt} of the load point as well as its corresponding liquid water profile can be estimated based on this sequence (see Chapter 2.3.3). For this estimation, the current density at the reversal point shown in Figure 3.3c is used as i_{lim}. For more details about the procedure and its legitimization, the reader is referred to Göbel et al. [50].

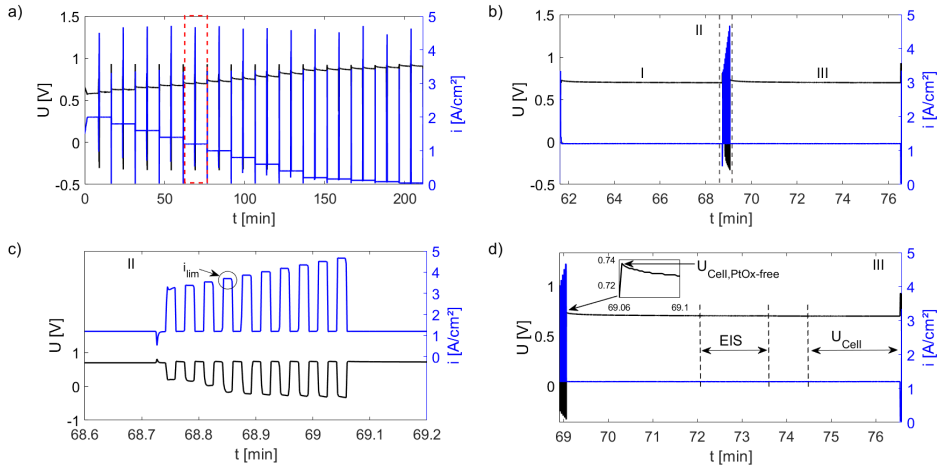

Figure 3.3: a) Overview of the developed diagnostic procedure comprising 13 measurement sequences between 2.0 and 0.0 A/cm^2; b) Detailed view of the measurement sequence at 1.2 A/cm^2; illustrating the three distinct phases of the procedure (highlighted in red in (a)); c) Close-up of Phase II from (b), showing the one potentiostatic and nine galvanostatic steps used to determine i_{lim}, which is required for calculating R_{mt} (see also Chapter 2.3.3); d) Close-up of Phase III from (b), including the determination of$U_{Cell,PtOx-free}$ (highlighted in the inset), U_{Cell}, and the ohmic resistances (R_{HFR},R_{H^+}) via EIS (refer to Chapter 2.3.4).

In Phase III (Figure 3.3d) the same current density as in Phase I is held for another 7.5 mins. Thereby, a voltage decay can be observed that is attributed to the re-formation of PtOx (see inlet Figure 3.3d) The maximum voltage (~1 s after the start of Phase III) is considered to be "PtOx-free".[2] The average voltage of the last two minutes of Phase III is referenced as stationary voltage. This voltage is used to extract the so-called stationary polarization curves from the 13 test sequences shown in Figure 3.3a. From the PtOx-free and stationary voltage, the losses due to PtOx-formation can be determined for every single load point shown in Figure 3.4a as $\eta_{|PtOx}$. The strict linkage of the voltage decay in Phase III to the formation of PtOx is reasonable as all other potential causes can be ruled out [50]: Firstly, the contribution from double layer charging within the observed voltage decay is insignificant as the capacitive current is in in the range of several µA/cm^2, assuming 100 mF/cm^2 as double layer capacity. Secondly, as Phase II is too short to change the temperature of the whole cell setup, the temperature in the catalyst layer and the temperature in Phase III is constant. Thirdly, if liquid water is absent the RH-profile is also settled within ms after Phase B. Consequently, no changes of the Ohmic losses in Phase III are expected. Fourthly, the resettling of the oxygen profile after Phase III is finished after 25 ms and it is assumed that the liquid water profile and the mass-transport-related losses within in Phase

[2] The term “PtOx-free” used in this context is somewhat loosely as in the first second of the hold time some surface adsorbates will have formed.

III are constant, too.
Fifth, if liquid water is present in the GDL and/or cathode, it can be argued that there is insufficient time for significant evaporation, and as a result, the mass transport-related losses remain unchanged during Phase III. This rationalization of the unchanged liquid water profile over Phase III is further supported by our later discussed findings (Figure 4.3), that the PtOx-losses at BoL are almost independent on current density - a misinterpretation of the mass-transport losses due to varying liquid profiles would cause a notable dependence instead. In addition to the PtOx-loss determination, EIS-Spectra between 50 Hz and 30 kHz were recorded from minute 3 to minute 4.5 of Phase III (Figure 3.3d) and were fitted with the help of a transmission line model to derive R_{HFR} and R_{H+} (see also Chapter 2.3.4).
In Figure 3.4a an exemplary set of PtOx-free and stationary polarization curves at BoL and EoT is shown. It can be seen how the PtOx related overpotentials η_{PtOx} and the degradation related voltage losses referred to as ΔU_{loss} for both types of polarization curve are determined.

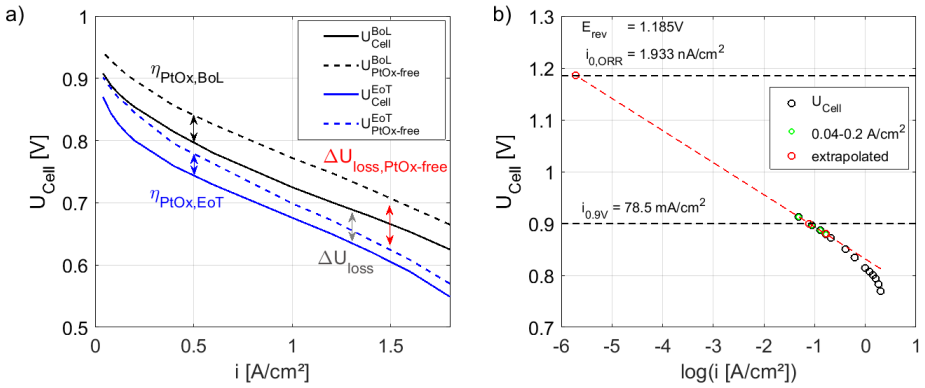

Figure 3.4: a) Exemplary data set of steady state (solid lines) and PtOx-free (dashed lines) polarization curves at BoL and EoT obtained with the developed diagnostic routine; b)Exemplary representation of the interpolation and extrapolation routine used to determine the current density at a cell voltage of 0.9 V and i_0 at E_{rev}.

Additionally, the gathered data are used to obtain the cathodic half cell voltage E_C (see also Chapter 2.3)

$$E_C = U_{Cell} + \eta_{R_{HFR}} + \eta_{mt} + \eta_{R_{H^+}}, \tag{3.1}$$

respectively the PtOx-free cathodic half cell voltage $E_{C,PtOx\text{-}free}$,

$$E_{C,PtOx-free} = U_{Cell,PtOx-free} + \eta_{R_{HFR}} + \eta_{mt} + \eta_{R_{H^+}}. \tag{3.2}$$

These cathodic half-cell potentials were used to determine the current density at a cathodic half-cell voltage of 0.9 V and the exchange current density i_0. These current densities were obtained

by extrapolating or interpolating the measured cathodic half-cell potentials within a current density range of 0.04 to 0.12 A/cm^2. Figure 3.4b illustrates the extrapolation and interpolation method using an exemplary data set. In order to estimate the specific catalyst activity (SA). Therefore the estimated current density at 0.9 V is divided by the derived ECSA.
Table 3.1 provides an overview of the values obtained through the described diagnostic procedure and their relation to the overpotentials discussed in Chapter 2.3.

Table 3.1: Overview of the diagnostic procedure, the obtained values, and their relation to the overpotentials described in the referenced chapters.

Phase / Calculations	**Purpose**	**Obtained value(s)**	**Related Overpotential(s)**	**Reference Chapter(s)**
I - Conditioning	set RH-profile	–	–	–
II - Limiting current measurements	Mass-transport evaluation, PtOx reduction	$i_{\text{lim}} \rightarrow R_{\text{mt}}$	η_{mt}	2.3.3
III - Load point measurement	Pol. curve determination	$U_{\text{Cell,PtOx-free}}$ U_{Cell} R_{HFR} R_{H^+}	η_{PtOx} $\eta_{R_{\text{HFR}}}$ $\eta_{R_{H^+}}$	2.3.4 2.3.5
Additional calculations	Get cathodic half cell potentials, i_0 determination	E_C $E_{C,\text{PtOx-free}}$ i_0,$i_{0,\text{PtOx-free}}$ $i_{0.9V}$	η_{act}	2.3.2

As described in Chapter 3.2 square wave ASTs are used to stress numerous MEAs. The parameters for the individual square wave ASTs are listed in Table 3.2.

Table 3.2: Overview of the varying conditions during accelerated test aging of the fuel cells.

AST-type	LPL [V]	UPL [V]	T [°C]	RH [%] [1]	τ [s] [2]	k_{EoT}
1 (Ref.)	0.6	OCV[3] (~ 0.98)	90	100	5	63500
2	0.72	OCV	90	100	5	63500
3	0.6	OCV	90	100	10	31500[4]
4	0.6	OCV	90	100	20	31500[4]
5	0.6	OCV	90	100	2.5	63500
6	0.6	OCV	70	100	5	63500
7	0.6	OCV	90	80	5	63500
8	0.6	0.85	90	100	5	63500
9	0.6	0.85	80	52.4	5	63500
10	0.6	0.9	90	100	10	31500 [5]
11	0.6	0.9	90	100	2.5	63500

[1] Same RH-values are used at the anode and the cathode in all ASTs.
[2] Describes the hold time at the lower potential limit (LPL) and upper potential limit (UPL).
[3] Open circuit voltage
[4] AST stopped after 31500 cycles as $ECSA_{norm} < 0.5$ is reached.
[5] AST stopped after 31500 cycles due to technical problems.

4 Part 1: Influence of platinum oxide formation on PEM-FC cathode degradation evaluation [1]

In this chapter, it is shown how the formation of surface oxides influences respectively disturbs the evaluation of voltage losses related to the degradation of a PEM-FC cathode. Therefore, it is described how the measured voltage losses can be divided into different shares, by using the equations introduced in Chapter 2.3. These relations and the gathered data are used, to identify how the formation of surface oxides impacts the evaluation of PtOx-losses within the lifetime of a PEM-FC cathode.

4.1 Voltage loss break down

In the following, it is shown how the performance change of the degraded MEA can be broken down into single voltage loss contributions, which are quantified with the gathered data. In Figure 3.4a, the solid black and blue lines represent the measured stationary polarization curve at BoL and EoT ($U_{Cell}^{BoL/EoT}$), respectively. They contain the reversible cell voltage E_{rev} and the various overpotentials:

$$U_{Cell}^{BoL/EoT} = E_{rev} - \eta_{R_{HFR}}^{BoL/EoT} - \eta_{A,act}^{BoL/EoT} - \eta_{C,act}^{BoL/EoT} - \eta_{R_{H^+}}^{BoL/EoT} - \eta_{mt}^{BoL/EoT} - \eta_{PtOx}^{BoL/EoT} - \eta_{?}^{BoL/EoT} \tag{4.1}$$

These overpotentials are Ohmic losses, $\eta_{R_{HFR}}$, related to the proton-transport through the membrane and the Ohmic resistances of the electrically conductive components of the cell, activity losses of the anode, $\eta_{A,act}$, (neglected in the rest of this work due to high anode activity) and losses related to cathode. These cathode losses are the activation overpotential, $\eta_{C,act}$, losses related to the transport of protons through the cathode $\eta_{R_{H^+}}$, losses attributed to the oxygen

[1] Parts of this chapter have been published in D. Bernhard, T. Kadyk, U. Krewer, and S. Kirsch, "How platinum oxide affects the degradation analysis of PEM fuel cell cathodes," International Journal of Hydrogen Energy, vol. 46, no. 26, pp. 13 791–13 805, 2021 [54].

transport from the gas channels to the catalyst η_{mt} and losses related to the formation of surface oxides η_{PtOx}. Furthermore, possible unassigned overpotentials are referred to as $\eta_?$. The PtOx-free polarization curves are described by setting η_{PtOx} to zero:

$$U_{Cell,PtOx-free}^{BoL/EoT} = E_{rev} - \eta_{R_{HFR}}^{BoL/EoT} - \eta_{A,act}^{BoL/EoT} - \eta_{C,act}^{BoL/EoT} - \eta_{R_{H^+}}^{BoL/EoT} - \eta_{mt}^{BoL/EoT} - \eta_?^{BoL/EoT} \tag{4.2}$$

As $U_{Cell}^{BoL/EoT}$ and $U_{Cell,PtOx-free}^{BoL/EoT}$ are measured (as described in Chapter 3.3), the PtOx losses are derived from their difference:

$$\eta_{PtOx}^{BoL/EoT} = U_{Cell,PtOx-free}^{BoL/EoT} - U_{Cell}^{BoL/EoT} \tag{4.3}$$

To quantify the performance losses caused by degradation designated as ΔU_{loss} and $\Delta U_{loss,PtOx-free}$ in Figure 3.4, the difference between the BoL and EoT polarization is determined as,

$$\Delta U_{loss} = U_{Cell}^{BoL} - U_{Cell}^{EoT} \tag{4.4}$$

and

$$\Delta U_{loss,PtOx-free} = U_{Cell,PtOx-free}^{BoL} - U_{Cell,PtOx-free}^{EoT}. \tag{4.5}$$

The obtained differences of the BoL and EoT overpotentials are described in equation 4.6 and 4.7:

$$\Delta U_{loss} = \Delta\eta_{ECSA} + \Delta\eta_{SA} + \Delta\eta_{R_{HFR}} + \Delta\eta_{R_{H^+}} + \Delta\eta_{mt} + \Delta\eta_{PtOx} + \Delta\eta_? \tag{4.6}$$

$$\Delta U_{loss,PtOx-free} = \Delta\eta_{ECSA} + \Delta\eta_{SA} + \Delta\eta_{R_{HFR}} + \Delta\eta_{R_{H^+}} + \Delta\eta_{mt} + \Delta\eta_? \tag{4.7}$$

The first and the second term of equation 4.6 account for losses which are related to a reduced *ECSA* and a changed catalyst activity. For the estimation of these losses the Equations 4.8-4.11 are used: Based on Equation 2.21 $\Delta\eta_{act}$ account for losses which are related to a reduced ECSA and a changed catalyst activity. In the following these losses are estimated by using the change of current density at a cell voltage of 0.9 V at BoL and EoT

$$\Delta\eta_{act,0.9V} = \eta_{act,0.9V}^{BoL} - \eta_{act,0.9V}^{EoT} = m \cdot log_{10}\left(\frac{i_{0.9V}^{BoL}}{i_{0.9V}^{EoT}}\right). \tag{4.8}$$

The current density $i_{0.9V}^{Bol/EoT}$ is obtained from extrapolation (or interpolation) of the PtOx-free polarization curve and m representing the Tafel slope

$$m = 2.303 \cdot \frac{R \cdot T}{\alpha \cdot F}. \tag{4.9}$$

With R being the gas constant, T being the cell temperature in Kelvin, α being the cathodic transfer coefficient (α = 1 according to [48]) and F being the Faraday constant. Accordingly, the

Tafel slope is approximately 70 mV/dec [42–44]. With the assumption, that this loss is related to a change in specific activity and loss of ECSA, Equation 4.8 can be interpreted as,

$$\Delta\eta_{act,0.9V} = \Delta\eta_{SA} + \Delta\eta_{ECSA}. \tag{4.10}$$

By disregarding changes in i_0, as they can be allocated to $\Delta\eta_{SA}$, this overpotential can be calculated by using Equation 4.10 and the ECSA-dependent term of Equation 2.21

$$\Delta\eta_{act,0.9V} = 2.303 \cdot \frac{R \cdot T}{\alpha \cdot F} \cdot \left[log\left(\frac{i_{0.9V}^{BoL}}{i_{0.9V}^{EoT}}\right) - log\left(\frac{ECSA^{BoL}}{ECSA^{EoT}}\right)\right]. \tag{4.11}$$

Where the $ECSA^{BoL/EoT}$ are obtained from CV-measurements (see Chapter 3.2).
The third part of the performance loss is linked to changes of the HFR extracted from the impedance spectroscopy described in Chapter 2.3.4. This performance loss is described in equation 4.12

$$\Delta\eta_{R_{HFR}} = i \cdot A \cdot (R_{HFR}^{BoL} - R_{HFR}^{EoT}). \tag{4.12}$$

Where i describes the current density and A the active area of the used MEA (5 cm^2). The fourth contributor to the performance losses is the change of proton conductivity in the cathode. This voltage loss is estimated with equation 4.13 [51],

$$\Delta\eta_{R_{H^+}} = \frac{1}{3} \cdot i \cdot A \cdot (R_{H^+}^{BoL} - R_{H^+}^{EoT}). \tag{4.13}$$

Where $R_{H^+}^{BoL,EoT}$ is extracted from the impedance spectra (see Figure 2.4). The fifth term of equation 4.6 is related to the comparison of the mass-transport behavior of the fresh and aged MEA, an equation derived from the work of Zhirul et al. [42] is used to calculate the mass-transport-related voltage loss at end-of-test:

$$\Delta\eta_{mt} = \frac{R \cdot T}{F} \cdot \left(\frac{1}{4} + \frac{\gamma}{\alpha}\right) \cdot ln\left(\frac{p_{O2,ch} - \frac{R \cdot T}{4F} \cdot i \cdot R_{mt}^{BoL}}{p_{O2,ch} - \frac{R \cdot T}{4F} \cdot i \cdot R_{mt}^{EoT}}\right) \tag{4.14}$$

Where $R_{mt}^{BoL,EoT}$ is derived from the limiting current measurements described in Chapter 3.2, α represents the cathodic transfer coefficient and γ is the ORR reaction order with respect to oxygen partial pressure ($\gamma = 0.54$ according to Neyerlin et al. [48]). The oxygen partial pressure in the channels of the flow field is described with $p_{O2,ch}$. Equation 4.15 describes the influence of the sixth term of Equation 4.6 on the cell performance (see also Figure 3.4,

$$\Delta\eta_{PtOx} = \eta_{PtOx}^{EoL} - \eta_{PtOx}^{BoL} \tag{4.15}$$

The last part of Equation 4.6 is attributed to unassigned voltage losses introduced in Chapter 2.3.6 and is addressed by $\Delta\eta_?$:

$$\Delta\eta_? = \eta_?^{EoL} - \eta_?^{BoL} \tag{4.16}$$

Whereby $\eta_?^{Bol/EoT}$ is obtained from equation 4.6, as all other contributors are specified. The equations introduced above are valid under the assumption that the cell temperature is constant over the active area of the used MEA and that the difference between the oxygen and hydrogen concentration at the cell in- and outlet is insignificant.

4.2 Results and discussion

This chapter is divided into four parts. In the first three parts (Chapters 4.2.1–4.2.3), the BoL and EoT data gathered from MEAs stressed with ASTs 3-5 (variations of hold times at LPL and UPL; see Table 3.2) using the diagnostic procedure explained in Chapter 3.3 are discussed. Finally, in Chapter 4.2.4, the breakdown of the EoT performance loss into its different contributing factors is analyzed.

4.2.1 High frequency resistance, cathode proton transport resistance and oxygen mass-transport resistance

Figure 4.1 shows the measured R_{HFR}, R_{H^+} and R_{mt} at low, medium and high current densities. The Figure 4.1a-c represent the high frequency resistances derived from the EIS measurements. The differences between the BoL and EoT values are insignificant. Consequently, it can be concluded, that the proton conductivity of the membrane is not significantly reduced, e.g. by leached-out Co^{2+} from the cathode or other membrane degradation effects.

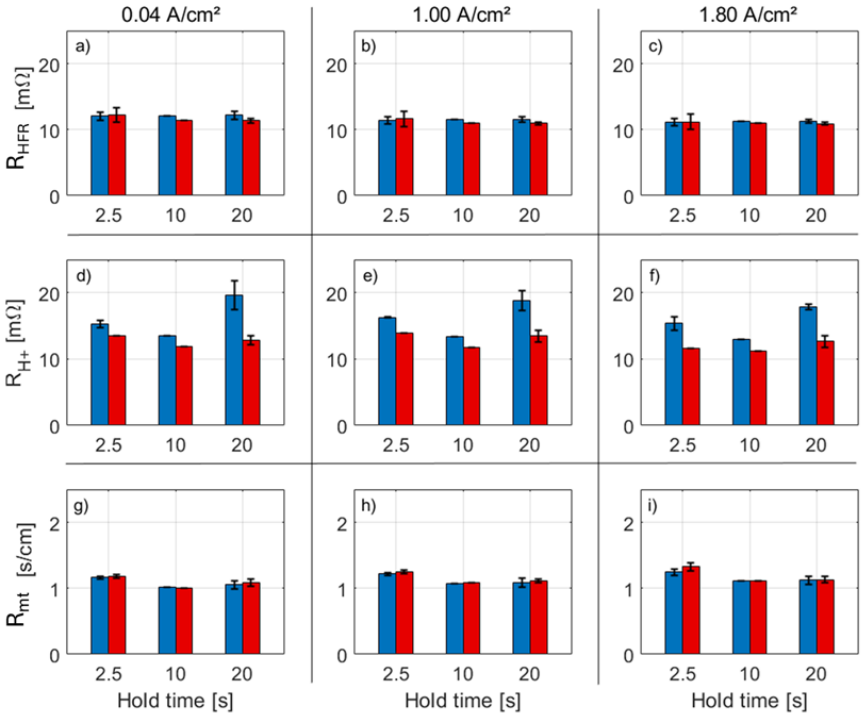

Figure 4.1: Overview of the measured BoL (blue) and EoT (red) values of R_{HFR} (a-c), R_{H+} (d-f) and R_{O2} (g-i) at 0.04, 1.0 and 1.8 A/cm^2 for AST-1, AST-3 and AST-4 (variation of hold times at LPL and UPL, see Table 3.2).

The Figure 4.1d-f show the obtained R_{H^+}. Even though there is a considerable scattering of the data (e.g. compare the BOL values), the proton transport resistance generally decreases at EOT. The reduction of R_{H^+} is possibly a result of reduced cathode thickness following carbon corrosion, which is known to become relevant at voltages as higher than 0.95 V [75, 149, 186, 187]. In addition to the reduced proton transport pathway, the reduced cathode layer thickness leads to an increasing amount of ionomer per volume, resulting in lower values for cathode proton resistance, as discussed, e.g., in [14, 188]. The influence of the changed cathode layer thickness on the Ohmic behavior of the analyzed MEAs is insignificant, as the R_{HFR} is mainly determined by the proton conductivity of the membrane.

In Figure 4.1g-l the extracted mass-transport resistances are summarized. For this cathode property, the difference between BoL and EoT is also insignificant. This result is in contradiction to the expectation derived from literature, where carbon corrosion leads to an increase of the oxygen mass-transport resistance [75, 114, 117]. But it is in line with findings recently published by

Harzer et. al. [44], where carbon corrosion was evident from SEM images although no significant increase in R_{mt} was detected. Generally, no difference in impact of the different degradation procedures on electron, ionic and oxygen mass transport could be observed in this work.

4.2.2 Catalyst activity

Figure 4.2 shows the electrochemical surface area (ECSA), current densities at 0.9 V, and the derived specific activity (SA) at BoL and EoT - normalized to the BoL values. The loss of current densities at 0.9 V increases with increasing hold time between 2.5 and 10 s but no significant difference between 10 and 20 s is found (Figure 4.2a). These losses can be divided in losses of ECSA and SA. The ECSA losses are shown in Figure 4.2b. Comparable results can be found in literature [106, 149], where higher ECSA losses were found with increasing hold times at the upper potential limit and lower potential limit.

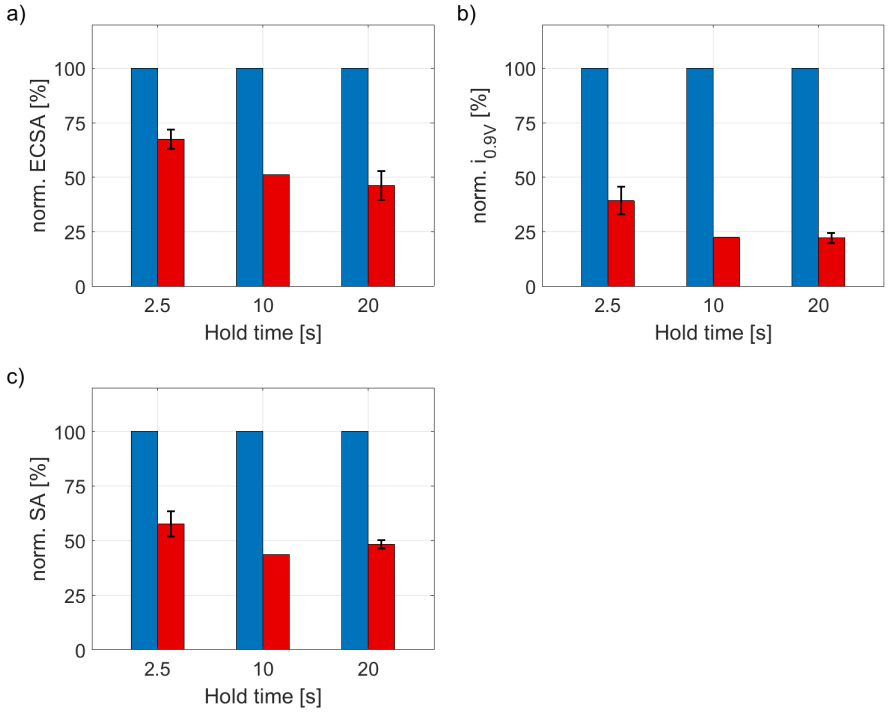

Figure 4.2: Overview of the normalized current densities at 0.9 V (a), electrochemical surface area (b) and specific activity (c) values at BoL (blue) and EoT (red) for ASTs 3-5 (variation of hold times at LPL and UPL, see Table 3.2).

The loss of SA (Figure 4.2c) is a well known degradation phenomenon for alloy catalyst [37, 100, 189, 190]. For pure Pt catalyst or catalysts with a very low alloy content, the specific activity shows only a slight decrease at EoT [37, 101, 191]. Consequently the loss of ECSA determines the voltage losses related to a change in activation overpotential [42, 75]. The loss of SA for the PtCo catalyst used in this work can be related to dealloying effects. The loss of the non-precious metal due to degradation results in a loss of the activity enhancing effect due to altered electronic structure of the catalyst material [37, 190].

4.2.3 Platinum oxide related overvoltages

In Figure 4.3a, the PtOx related overvoltages at BoL and EoT are shown as a function of cell voltage. But as the PtOx formation is driven by the potential on the cathode side it is necessary to consider the PtOx related overvoltages at BoL and EoT as a function of cathodic half cell voltage E_C (Figure 4.3b) to avoid a misinterpretation of the development of the PtOx related losses over time. The half cell voltage of the cathode is obtained by correcting the measured cell voltage $U_{equi.}^{BoL/EoT}$ with $\eta_{R_H^+}^{BoL/EoT}$,$\eta_{H+}^{BoL/EoT}$ and $\eta_{mt}^{BoL/EoT}$ (see also Equation 3.1). In general, Figure 4.3b shows, that the PtOx related overvoltages already exist at half cell voltages higher than 720 mV. This is in line with the recently published work of Kirchhoff et al., who show that oxide formation on platinum nanoparticles can already begin at 700 mV [57]. The PtOx related overvoltages increase with increasing half cell voltage (decreasing current density) between 750 and approximately 820 mV. After this maximum, the overvoltage decreases as the current density is further reduced.

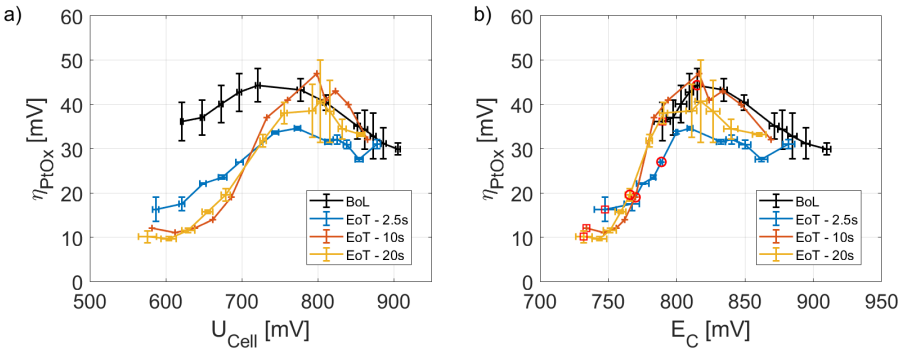

Figure 4.3: a) η_{PtOx} as function of the cell voltage BoL and EoT; b) η_{PtOx} as function of the half cell voltage E_C BoL and EoT (red circles: $\eta_{PtOx}^{BoL/EoT}$ @ 1.0 A/cm^2, red squares: $\eta_{PtOx}^{BoL/EoT}$ @ 1.8 A/cm^2).

To interpret this behavior, first, it needs to be stated, that there is (to the best of the authors knowledge) only a single further study on the subject of half cell voltage dependent voltage losses attributed to PtOx-formation [55]. Commonly, in papers investigating PtOx, the accumulated charge measured in the PtOx reduction peak of a CV is used for oxide quantification [59, 63, 65, 67]. In all these works, the amount of PtOx increases with increasing half cell voltage. This suggests that the PtOx overpotential would increase with half cell voltage, too - and contradicts the observed maximum in Figure 4.3. The increase of the PtOx overvoltage between 750 mV and 820 mV half cell voltage could be caused by higher kinetic loss due to an increasing oxide coverage of the catalyst particles [37, 192] and an increased loss from electron transport through (subsurface) oxides. Accordingly, the increase of oxide overvoltage with increasing half cell voltage, arises not uniquely from kinetic oxide losses, but at least partially from Ohmic oxide losses which also depend on current density. Consequently, the decrease of the PtOx losses at voltages higher than 820 mV represents lower kinetic and electronic losses from PtOx that arise from lower current densities (even though increasing Oxide loadings might further increase, as shown in [59, 65, 67]). Another possible explanation for the observed decrease of $\eta_{|PtOx}$ is the buckling effect occurring within the oxide formation process. Due to this process, the number of active sites for the ORR could increase again.
At half cell voltages lower than 750 mV $\eta_{|PtOx}$ seems to level off to a finite value. This 10 mV-offset could be related to the adsorption of anions from the ionomer on the catalyst surface. As Jinnouchi et al. showed by DFT simulations for Pt(111), adsorption of sulfonate containing anions is thermodynamically favored between half cell voltages of 400 and 780 mV. These adsorbates suppress the oxide formation, poison the catalyst and result in an inhibition of the ORR [192, 193]. Accordingly, it appears, that the "PtOx free" polarization curve not only shows reduced losses from PtOx, but is also not impacted (or at least less impacted) from anion adsorption, potentially in line with the findings of [194] about the regeneration of sulfonate adsorbates. Figure 4.4 shows the measured PtOx related overvoltages at 0.04, 1.0 and 1.8 A/cm^2 at BoL and EoT extracted from Figure 4.3b . At 0.04 A/cm^2 (Figure 4.4a) it can be seen that almost the same PtOx-related overvoltages are obtained at BoL and EoT independent of the chosen hold time. In Figure 4.4b and c, the overvoltages at 1.0 A/cm^2 respectively at 1.8 A/cm^2 are shown. At these current densities $\eta_{|PtOx}$ is reduced significantly at EoT due to decreased half cell voltage at higher current densities. And as the activity decreases with increasing hold time (see Figure 4.2) lower half cell voltages are obtained at EoT and consequently the reduction of $\eta_{|PtOx}$ is more severe if the hold time is increased from 2.5 to 10 s. But no further reduction of $\eta_{|PtOx}$ is obtained for a hold time of 20 s, as comparable activity losses are measured for hold times of 10 and 20 s (see Figure 4.2).

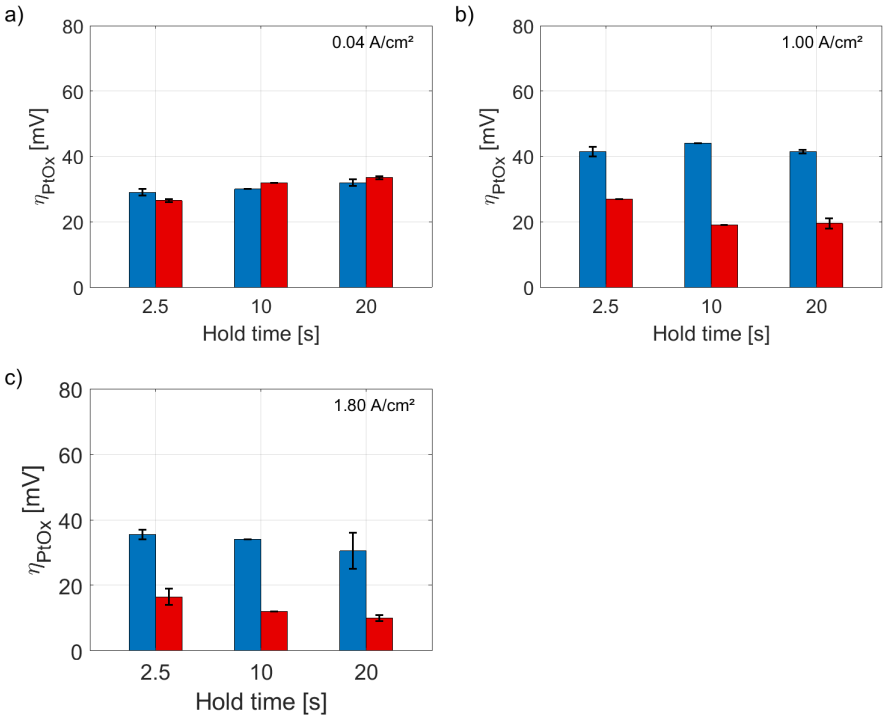

Figure 4.4: Overview of the average BoL (blue) and EoT (red) PtOx overvoltages at (a) 0.04 , (b) 1.0 and (c) 1.8 A/cm^2 obtained from the MEAs stressed with ASTs 3-5 (variation of hold times at LPL and UPL, see Table 3.2).

4.2.4 Break down of degradation-caused voltage losses

In this Chapter the differences between the different overvoltages defined in Chapter 2.3 at BoL and at EoT obtained for the three ASTs (AST 3-5, Table 3.2) are compared to each other. The data described in the chapters before is used to break down these losses into the different contributors of Chapter 2.3 and the origin of the unassigned voltage loss is discussed.

Figure 4.5a represents the stationary polarization curves at BoL and EoT for differently aged samples. In Figure 4.5b-d, the break down of the measured degradation related voltage losses at 0.04, 1.0 and 1.8 A/cm^2 following the equations 4.8-4.16 is depicted. In general one can see the following: As the R_{HFR} did not show significant changes over life (Figure 4.1a-c), additional R_{HFR}-related voltage losses (according to Equation 4.12) are absent. The same is true for oxygen transport related losses, as the oxygen transport resistance was stable, too (Figure 4.1g-i). The cathode proton resistance seemed to show some decrease for all variants of the AST (Figure 4.1d-f). This decrease was converted with the help of equation 4.13 and leads to negative

voltage loss changes. PtOx-losses were seen to be reduced at EoT in Figure 4.4 for all but the smallest currents. The work of Zago et al. also shows, that the catalyst activity is less influenced by PtOx for aged samples [193].

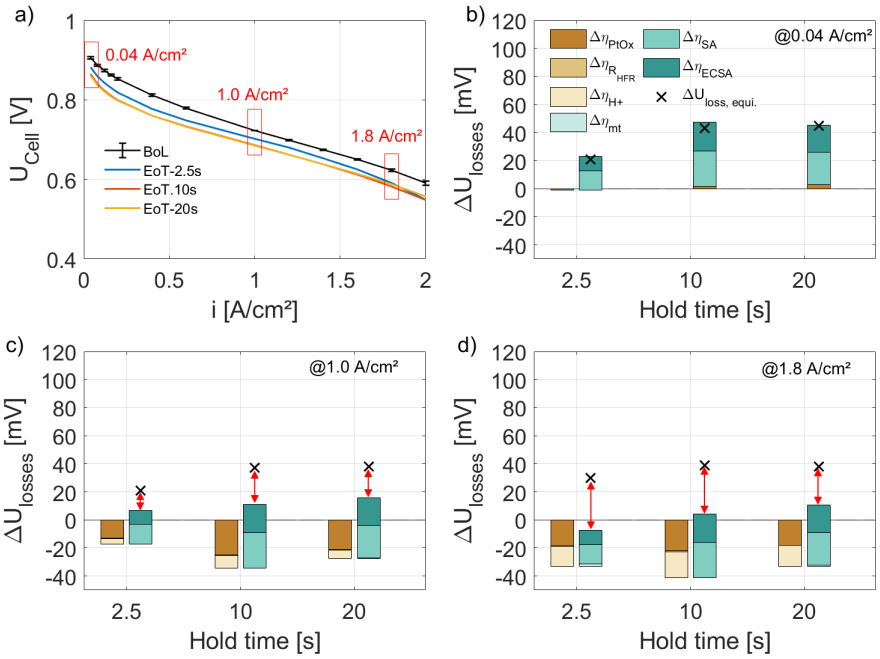

Figure 4.5: a) Averaged begin-of-life polarization curve and the obtained end-of-test polarization curves for the MEAs stressed with AST-3, AST-4 and AST-5 (variation of hold times at LPL and UPL) ; b-d) Break down of the additional voltage losses at end-of-test at 0.04 (b), 1.0 (c) and 1.8 A/cm^2 (d) into the different contributors introduced in Chapter 4.1.

Accordingly, in Figure 4.5c-d the difference is also counted as gain (bars heading negative). Increases in the voltage losses arise majorly from a reduction in activity, whereby ECSA and SA contribute almost equally. The related bars are heading up, starting below zero at the value of total gain. The gap between the upper end of the ECSA-related voltage losses and the black tick marks the additional unassigned voltage losses at EoT. They will be discussed in the end of this Chapter, when the impact of current density and hold time has been rationalized. According to Equation 4.11 the ECSA and SA related voltage losses are independent of current density and therefore constant in Figure 4.5b-d. Increasing gains (with increasing current density) arise on the one hand from the trend in cathode proton losses with hold time. But no clear trend can

be identified given the error bar of the cathode proton resistance (Figure 4.1d-f). On the other hand, increasing gains (with increasing current density) arise from reduced oxide-related voltage losses, whereby the root cause is simply a reduced oxide formation with decreasing half cell voltage EoT (as shown in Figure 4.3b). Thereby, the PtOx-gain is almost identical for 1.0 and 1.8 A/cm^2, simply due to the curvature of the oxide voltage losses with half cell voltage (Figure 4.3b - compare highlighted marks at 1.0 and 1.8 A/cm^2 BoL and EoT). Though, the gain from a reduced cathode proton resistance also increases due its direct dependence on current density (Equation 4.13).
Discussing the impact of hold times, it is evident, that the total losses (black ticks) increase from 2.5 to 10 s. The outcome of the AST with 20 s hold time is then very close to the AST with 10 s hold - hardly larger than the error bar ($\sim$5 mV). This result is in line with earlier studies [42, 106], which also found that ASTs with the same upper potential limit tend to the same EoT voltage losses. As expected, also ECSA and SA losses increase from 2.5 to 10 s, but not further when the hold time is 20 s. Regarding the trend in the PtOx-related voltage losses, one can see the lowest gain for the AST with 2.5 s hold time due to the higher EoT half cell voltage. And it seems that there is also a little less gain in the case of 20 s hold time. However, this potentially unexpected difference between the ASTs with 10 and 20 s hold time is in the order of 5 mV and therefore pretty small. Nonetheless, it might point to slightly different EoT states of the samples - evidently particle size and shape have a tremendous impact on PtOx build-up [57, 195].
In the end, the increase in unassigned voltage loss shall be discussed. Evidently, the loss is negligible at 0.04 A/cm^2 and increases with current density up to 35 mV. This insight is surprising, as the almost perfect vertical shift in the polarization curves EoT (Figure 4.5a) suggests that degradation trivially causes activity losses only. However, if the PtOx related voltage losses are taken into account, unassigned losses remain or rather turn out larger than without considering PtOx.
Earlier, others have identified an unassigned voltage loss, too [45, 74–76]. However, in the current work the discussion of the unassigned voltage loss is based on the direct determination of the oxygen transport resistance and PtOx-related voltage losses. Accordingly, with this additional diagnostic information, the often argued "increased oxygen transport resistance EoT" can be excluded, as no change in oxygen transport resistance over the course of AST-testing is seen (Figure 4.1g-i). A similar argument was made by in [44] derived from the comparison of stationary limiting currents at BoL and EoT. Oppositely, two hypotheses seem more plausible to explain the unassigned voltage loss. The first hypothesis is based on an increased Tafel slope over the course of AST testing. Support of this idea arises from Figure 4.6, which displays the unassigned voltage losses as a function of half cell voltage at EoT. Indeed, a linear increase with half cell voltage is seen. Therefore, the unassigned losses could be caused by a disregarded increase of the Tafel slope at EoT. This increase will lead to a steeper slope of the polarization curve and consequently the unassigned voltage losses would be reduced. However, assuming increasing Tafel slope is counter intuitive as PtCo is known to exhibit a larger Tafel slope compared to Pt [196–198]. But likely the catalyst is more Pt-like at EoT due to leaching and accordingly should

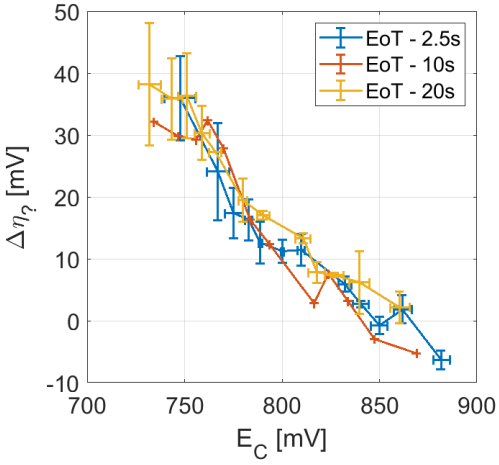

Figure 4.6: $\Delta\eta_?$ as function of the half cell voltage EoT.

have lower Tafel slope at EoT compared to BoL - not larger.

The second hypothesis that might be plausible is based on catalyst poisoning due to sulfonate adsorption on the catalyst surface [199, 200]. Indeed, Kodama et al. found an increasing voltage loss from Nafion at Pt with decreasing (Figure 6 in Kodma et al. [201]). Accordingly, at EoT more sulfonate adsorption losses could be expected at any given current. This expectation can be roughly quantified. Referring to Kodama et al. [201], the losses from Nafion at Pt increase from ∼40 mV at a half cell voltage of ∼900 mV to ∼60 mV at a half cell voltage of 700 mV. This means at least a voltage loss of ∼10 mV loss can be attributed to the interaction between Nafion and the catalyst if there is a reduction of the half cell voltage of 100 mV. Figure 4.3b shows, that the half cell voltage at 1.8 A/cm^2 decreases from ∼800 mV to ∼700 mV over the cause of AST-testing (for all ASTs). This decrease of half cell voltage yields in 35 mV of unassigned loss (Figure 4.6), which is indeed more than the 10 mV expected from [201]. Howerever, this study focuses on of Nafion on Pt(111) in an RDE-setup and therefore a considerably different system [201].

4.3 Concluding remark

In this Chapter 4, PEM-FC cathodes containing a PtCo catalyst, degraded via square wave accelerated stress tests (variation of hold time), were analyzed with a dedicated diagnostic procedure. For every individual load point, the oxygen transport resistance and voltage losses due to the formation of PtOx were obtained in addition to commonly measured electrochemical active surface area, high frequency as well as proton transport resistance. This data was used to break down the end-of-test voltage losses into six different contributors.

The high frequency resistance and the oxygen mass transport resistances shows no significant changes end-of-test. Consequently, no performance loss was attributed to an increased mass transport or to an increased Ohmic resistance end-of-test. In contrast, the proton resistance decreased for the analyzed samples, leading to performance gains after the accelerated stress tests. This behavior might be related to a loss of carbon, leading to an increased volumetric ionomer content. As the electrochemical active surface area and the specific activity were reduced due to degradation, activity related performance losses are obtained. The PtOx related losses are decreased at end-of-test, except at the smallest current densities. Most noticeably, it was shown that PtOx-related voltage losses show almost the same dependency on half cell voltage for all begin- and end-of-test samples. Taking all these different contributors into account, additional unassigned voltage losses remain.

Interestingly, the unassigned voltage loss was not only present at highest current densities as found elsewhere [45, 74, 76], but showed a steady increase with current density. When plotting it against half cell voltage, it was found to even be independent from the accelerated stress tests, or in other words: The unassigned voltage loss at end-of-test showed the same linear increase with cathode overvoltage for all accelerated stress tests. A possible explanation could be, that the origin of the unassigned loss might arise from ionomer adsorption that, based on an earlier publication, depends on half cell voltage [201]. In the end it can not be in scope of membrane electrode assembly testing to unambiguously identify the root cause of the unassigned voltage loss. Though with this new diagnostic procedure, a good attempt in revealing its true impact can be provided.

In the following chapter, an approach is presented for predicting activity degradation-related performance loss in PEM fuel cells using a generalized Tafel model. It also demonstrates how the reduction in PtOx-related voltage losses during degradation influences the prediction of kinetic performance losses associated with degradation.

5 Part 2: Model-assisted analysis and prediction of activity degradation in PEM-FC cathodes [1]

In this chapter a model for the prediction of performance losses related to the activity degradation of the cathode catalyst, arising from accelerated stress testing is presented. It is shown, how the gathered data are used to determine the cathodic half cell voltage, to make losses caused by activity degradation accessible.

5.1 Determination of kinetic cathode losses

Kinetic cathode losses are understood as voltage losses in absence of Ohmic losses (majorily from membrane and cathode ionomer) and losses from oxygen transport. Anodic losses are generally assumed to be negligible [37]. By correcting the measured cell voltage with these overpotentials, the cathodic half cell voltage E_C can be calculated with Equation 5.1

$$E_C(k,i) = U_{Cell}(k,i) + \eta_{R_{HFR}}(k,i) + \eta_{mt}(k,i) + \eta_{R_{H^+}}(k,i), \tag{5.1}$$

where U_{Cell}(k,i) represents the measured cell voltage depending at the number of AST cycles k and the current density i [44, 76]. The second, third and fourth term on the right hand side of Equation 5.1 describe the overpotentials related to the Ohmic resistance determined by $R_{HFR}(k,i)$, the oxygen mass transport determined by $R_{mt}(k,i)$ and the transport of the protons through the catalyst ionomer determined by $R_{H_+}(k,i)$. How these overpotentials can be calculated is described in the Chapters 2.3.3- 2.3.4. In Figure 5.3a half cell voltages $E_C(k,i)$ over the

[1] Parts of this chapter have been published in D. Bernhard, T. Kadyk, S. Kirsch, H. Scholz and U.Krewer, "Model-assisted analysis and prediction of activity degradation in PEM-fuel cell cathodes," Journal of Power Sources, vol.562, p.232771 [150].

course of AST testing can be seen, the difference between the half cell voltages during the stress test and the BoL half cell voltages ($k = 0$) is defined as kinetic cathode losses $\Delta E_{C,exp}(k,i)$

$$\Delta E_{C,exp}(k,i) = E_C(k,i) - E_C(0,i). \tag{5.2}$$

5.2 Modeling

In the following, the model equations describing the ECSA loss (Chapter. 5.2.1) and the voltage loss prediction (Chapter 5.2.2) are introduced. Afterwards, an exemplary simulation is presented to visualize the mechanics of the models (Chapter 5.2.3).

5.2.1 Losses in electrochemical surface area

The degradation of the electrode catalyst can be monitored through changes in the particle radius distribution $f_N(r,t)$, which is normalized to the begin of life particle radius distribution. According to Urchaga et al., the change of the distribution over time can be described by a Fokker-Planck type continuity equation, where the PRD is described by using the particle radius r [173],

$$\frac{\partial f_N(r,t)}{\partial t} = \frac{\partial}{\partial r} \cdot \left(f_N(r,t) \cdot \frac{dr}{dt} \right) + J^+ - J^- - k_{det} \cdot f_N(r,t). \tag{5.3}$$

In this equation, the first term on the right hand side describes the dissolution and redeposition due to Ostwald ripening. The terms J^+ and J^- describe particle coagulation and represent the particle creation and extinction terms, respectively. The last term describes particle inactivation, e.g. by detachment from the substrate. While trying to identify J^+ and J^- in the individual AST data sets the problem of overfitting occured. In consequence, these contributions were excluded from the model.[2] Accordingly, the change in particle radius distribution can be described with

$$\frac{\partial f_N(r,t)}{\partial t} = \frac{\partial}{\partial r} \cdot \left(f_N(r,t) \cdot \frac{dr}{dt} \right). \tag{5.4}$$

The rate of particle radius change is determined by dissolution and redeposition terms [173],

$$\frac{dr}{dt} = V_m \cdot k_{rdp} \cdot \bar{c}_{Pt}(t) \cdot exp\left(\frac{-R_0}{r} \right) - V_m \cdot k_{dis} \cdot c_{Pt}^{ref} \cdot exp\left(\frac{R_0}{r} \right), \tag{5.5}$$

[2] This simplification of Equation 5.3 is justified, as degradation of the cathode catalyst due to coagulation and inactivation of the catalyst particles is mainly driven by carbon corrosion (see also Chapter 2.4.2.2 [95, 116, 117]. Significant corrosion rates are normally expected at cell voltages higher than 1 V [44, 113–115], which do not occur in the degradation experiments carried out in this work.

where the redeposition parameter k_{rdp}, the product of dissolution parameter and platinum concentration $k_{dis} \cdot c_{Pt}^{ref}$ and the characteristic radius R_0 are extracted from the measured ECSA-evolution depending on the AST-conditions summarized in Table 5.1. Note that two different rate constants k_{dis} and k_{rdp} for forward and backward reaction were employed. The Pt redeposition rate depends on the concentration of Pt dissolved in the electrolyte, which can be calculated as [173]

$$\overline{c}_{Pt}(t) = \frac{m_V}{M_{Pt}} \cdot (1 - M_N(t)) \tag{5.6}$$

assuming that the initial concentration is zero, $\overline{c}_{Pt}(t=0) = 0$. Here, m_V is the Pt mass loading per unit volume, M_{Pt} is the molecular weight of Pt and $M_N(t)$ is the normalized dimensionless mass moment of $f_N(r,t)$ [173].

$$M_N(t) = \frac{\int_0^\infty r^3 \cdot f_N(r,t)dr}{\int_0^\infty r^3 \cdot f_N(r,0)dr} \tag{5.7}$$

Solving Equation 5.4, using Equation 5.5, allows for the determination of the evolution of the normalized electrochemical active surface area $ECSA_{norm}$ [173],

$$ECSA_{norm}(t) = \frac{\int_0^\infty r^2 \cdot f_N(r,t)dr}{\int_0^\infty r^2 \cdot f_N(r,0)dr}. \tag{5.8}$$

The model is solved by using a variable order solver based on numerical differentiation formulas implemented as ODE15s in MATLAB version 9.5.0.944444 (R2018b). The three parameters k_{rdp}, $k_{dis} \cdot c_{Pt}^{ref}$ and R_0 were fitted with a least-squares method. For the minimization a Nelder-Mead simplex algorithm was implemented (Used MATLAB function: fminsearch).
The evolution of the ECSA depends on the operating conditions of the AST. Empirical relationships between the degradation parameters and operating conditions were derived. In Equations 5.9 and 5.10 the derived relationship between the dissolution related parameter $k_{dis} \cdot c_{Pt}^{ref}$, respectively the redeposition related parameter k_{rdp} and the AST conditions are shown,

$$\begin{aligned} c_{Pt}^{ref} \cdot k_{dis}(UPL, LPL, RH, T, \tau) = c_{Pt}^{ref} k_{dis,ref} &\cdot \left(1 + g_\tau \cdot (\tau - \tau_{ref})\right) \\ &\cdot exp\left(-g_T \cdot \left(\frac{1}{T} - \frac{1}{T_{ref}}\right)\right) \\ &\cdot exp\left(g_{LPL} \cdot (LPL - LPL_{ref})\right) \\ &\cdot exp\left(g_{UPL} \cdot (UPL - UPL_{ref})\right) \\ &\cdot \left(1 + g_{RH} \cdot \left(\frac{RH}{RH_{ref}} - 1\right)\right) \end{aligned} \tag{5.9}$$

Table 5.1: Overview parameters ECSA-Model (see Equations 5.9 and 5.10)

Parameter		Unit
R_0	22.039	$[nm]$
$c_{Pt}^{ref} k_{dis}$	$1.9909 \cdot 10^{-16}$	$[mol/m^2 s]$
g_τ	0.0728	$[1/s]$
g_T	4875.7	$[K]$
g_{LPL}	2.6930	$[1/V]$
g_{UPL}	12.8143	$[1/V]$
g_{RH}	1.1644	$[-]$
$k_{rdp,ref}$	$1.9900 \cdot 10^{-10}$	$[m/s]$
h_τ	0.3446	$[1/s]$
h_{UPL}	28.8074	$[1/V]$
T_{ref}	363.15	$[K]$
τ_{ref}	5	$[s]$
LPL_{ref}	0.6	$[V]$
UPL_{ref}	OCV($\sim$0.98)	$[V]$
RH_{ref}	100	$[\%]$

and

$$k_{rdp}(\tau, UPL) \;=\; k_{rdp,ref} \cdot exp(h_\tau \cdot (\tau - \tau_{ref})) \cdot exp(-h_{UPL} \cdot (UPL - UPL_{ref})). \quad (5.10)$$

The parameters $c_{Pt}^{ref} k_{dis,ref}, g_\tau, g_T, g_{LPL}, g_{UPL}$ and g_{RH}, respectively $k_{rdp,ref}, h_\tau$ and h_{UPL} are needed to describe the dependency of the degradation parameters $k_{dis} \cdot c_{Pt}^{ref}$ and k_{rdp} from the operation conditions of the AST. The identified parameters and the reference values are summarized in Table 5.1.

5.2.2 Degradation related kinetic voltage losses

Assuming that Tafel slope and exchange current density can be correlated uniquely to the cycle number k of a given AST (see Chapter 5.3.3 for proof), the cathode activity related overpotential (η^g_{act}) can be understood via a generalized Tafel approach derived from Equation 2.21

$$\eta^g_{act}(k,i) = m(k) \cdot log\left(\frac{i}{i_0(k) \cdot ECSA(k)}\right), \tag{5.11}$$

with m being the Tafel slope and i_0 the exchange current density. The kinetic cathode voltage $\Delta E_{C,sim}(k,i)$ losses arising from cathode degradation then follow from

$$\begin{aligned}\Delta E_{C,sim}(k,i) &= \eta^g_{act}(k,i) - \eta^g_{act}(0,i) \\ &= m(k) \cdot log\left(\frac{i}{i_0(k) \cdot ECSA(k)}\right) - m(0) \cdot log\left(\frac{i}{i_0(0) \cdot ECSA(0)}\right).\end{aligned} \tag{5.12}$$

According to Equation 5.12, at least two further functions are needed to describe $i_0(k)$ and $m(k)$. In Chapter 5.3.3 two empirical correlations are introduced, which can be used to describe the change of these two cathode parameters.

5.2.3 Modeling process

Figure 5.1 gives a visual representation of how the two-part degradation model links changes in catalyst structure to performance losses, based on an exemplary data set under the degradation conditions of AST 1 (see Table 3.2). In Figure 5.1a, the PRD (particle radius distribution) evolution is simulated using Equations 5.4–5.10 with the parameters listed in Table 5.1, under the operating conditions of AST 1. It can be observed that the PRD shifts toward larger particle radii with an increasing number of AST cycles and continued degradation. This trend is consistent with particle growth mechanisms such as agglomeration and Ostwald ripening, both of which contribute to a reduction in electrochemically active surface area (ECSA).

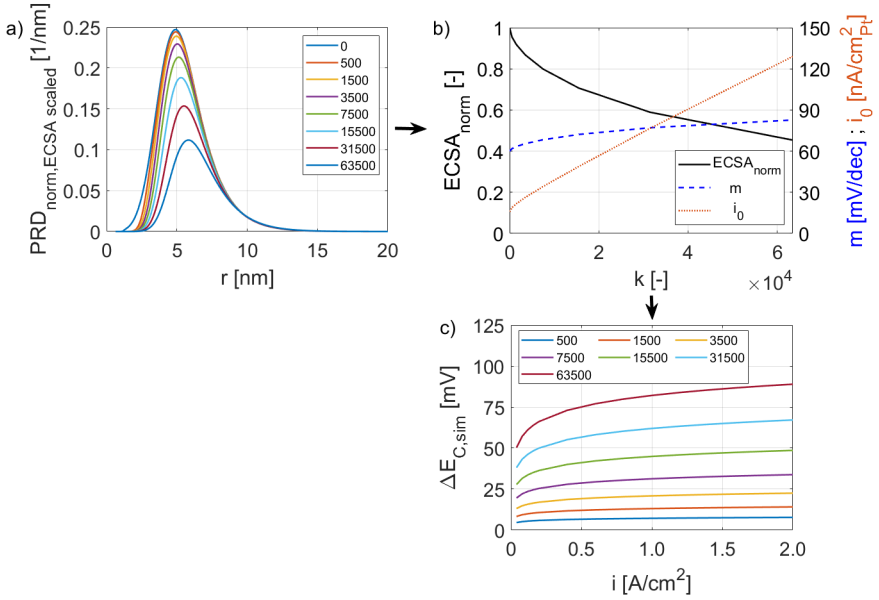

Figure 5.1: Model process shown with an exemplary data set based on the operation conditions of AST 1 defined in Table 3.2: a) Evolution of the normalized particle radius distribution (surface scaled) with cycle number given in the legend; b) Evolution of the normalized *ECSA* derived from the PRDs shown (Chapter 5.2.1 in (a) and the simulated values for m and i_0 depending on the number of AST cycles k (Chapter 5.3.3); c) Kinetic voltage losses ΔE_C between 0.0-2.0 A/cm^2 calculated with $ECSA_{norm}$, m and i_0 shown in (b) (Chapter 5.2.2).

The black line in Figure 5.1b depicts the ECSA evolution based on the simulated PRDs (see also Equation 5.8). The corresponding simulated values for the Tafel slope m and the exchange current density i_0, derived from the empirical correlations in Equation 5.13 and Equation 5.14 (presented in Chapter 5.3.3), are also shown in Figure 5.1b as a function of the number of AST

cycles k. Both m and i_0 increase during the AST, indicating degradation-induced changes in catalyst activity. Figure 5.1c shows the voltage losses ΔE_C, calculated using the generalized Tafel approach (Equation 5.12) over a current density range from 0 to 2.0 A/cm^2. The losses increase with both current density and the progression of the stress test.

5.3 Results and discussion

In the following, the experimentally determined trends of key variables for the different AST conditions summarized in Tab. 3.2 are analyzed. The key variables are ECSA, Tafel slope, exchange current density and cathode kinetic loss (see Sec. 5.3.1). In Chapter 5.3.2, the results obtained with the surface loss model introduced in Chapter 5.2.1 are shown and discussed. Subsequently, empirical correlations describing the Tafel slope and exchange current density as function of the normalized ECSA are derived and the parameters describing these correlations are identified (see Chapter 5.3.3). Finally, the accuracy of the kinetic cathode voltage loss model is discussed in Chapter 5.3.4.

5.3.1 Evaluation of experimental data

Figure 5.2 displays the influence of the different AST conditions on the measured ECSA loss. Figure 5.2a shows the influence of the UPL variation (0.85 V vs. OCV). It can be seen, that with an UPL of 0.85 V, an ECSA loss of 15 % is reached after 3.000 AST cycles. Afterwards, the ECSA loss decreases and an almost asymptotic behavior can be observed. Contrary with an UPL of 0.98 V, the ECSA is continuously reduced and no asymptotic behavior can be observed within the first 30000 AST cycles. Overall, there is a reduction to 55 % of ECSA for 0.98 V vs. 83 % for 0.85 V. This finds broad consens in current literature [42, 44, 91, 102, 106, 152, 202, 203]. In Figure 5.2b, the influence of the hold time is presented. It can be seen, that the ECSA loss increases with increasing hold time of the potential limits. After 31500 AST cycles, the ECSA is reduced by 33 %,45 % and 64 % of the original ECSA for hold time τ of 2.5 s, 5 s respectively 20 s. Comparable trends were observed earlier [42, 44, 91, 106, 152]

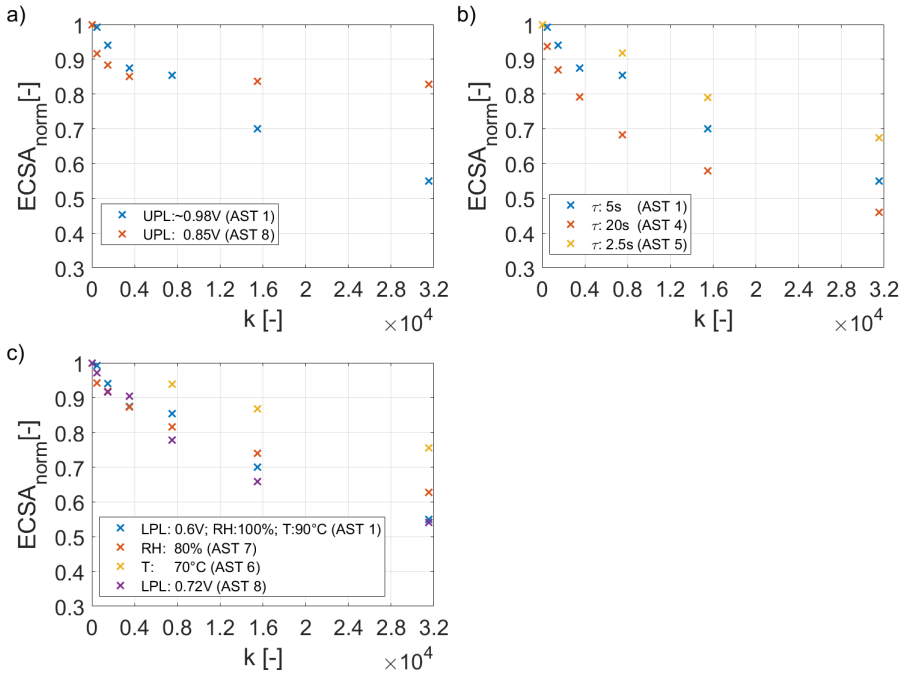

Figure 5.2: Measured ECSA evolution depending on the AST conditions UPL, hold time and T,RH, LPL and the number of AST cycles. As reference the data measured for AST 1 represented by the blue data points in the Figs. a-c are used. a) Influence of the UPL variation on the ECSA decay; b) Influence of the hold time τ at the UPL and LPL in the ECSA decay; c) Influence of RH,T and LPL variation on the ECSA decay.

In Figure 5.2c, the influence of T, RH and LPL on the measured ECSA loss is shown. Again, the ECSA decay of AST 1 is used as reference (blue crosses in 5.2a-c). It can be seen, that an increase of the LPL to 0.72 V has no significant influence on the ECSA loss, comparable to observations of Kneer et al. [91]. Reducing the temperature by about 20 K reduces the ECSA loss after 31500 AST cycles by about 20 %. A decreased degradation due to a temperature reduction has also been reported recently [152, 167–170]. Similarly, a reduction of the relative humidity causes a slight decrease of the ECSA-loss rate. This result is supported by numerous studies [151, 152, 170, 171].

Consequently, model parameters, $k_{dis} \cdot c_p^{ref}$ and k_{rdp} are most sensitive to the following AST properties: UPL, hold time and temperature. Only a slight dependency on RH is expected and the LPL should also have only a minor influence. The related empirical trends are part of the model formulation (see Equation 5.9 and Equation 5.10).

Figure 5.3a shows cathode half cell voltages during aging for an exemplary data set obtained with AST 1. The half cell voltage (Figure 5.3a) is plotted logarithmically with respect to current

density, to better focus the Tafel slopes. Evidently, the linear slope in the current density range between 0.0 and ~1.2 A/cm^2 seems constant on first sight as cycling progresses. But if analyzed in detail, (see Figure 5.3b - blue dashes) the Tafel slope is increasing from initial 65 mV/dec to 85 mV/dec at the end of test. At the same time, the exchange current density extracted from the range 0.0-0.2 A/cm^2 goes through a maximum (Figure 5.3b - orange dotted). Simultaneously, the particle radius distribution is shifted to bigger particles (shown in Figure 5.1) and the ECSA is reduced (Figure 5.3b - black solid). The observed changes of the activity parameters might be linked to dealloying, or changes in the distribution of the crystal facets. While dealloying reduces the activity enhancing strain and ligand effects [124, 135, 140], might have an impact due to altered relevance of differing reaction pathways. The hypothesis can be drawn, that the surface of the most active facet (111) at low current density (~120 mV/dec [204]) might degrade less or even grow at the cost of the most active facet (110) at high current density (~60 mV/dec [204]) [55], as this facet is most prone to degradation [105]. The increasing m and i_0 in this study would be a consequence of fitting these overlapping kinetics in the specific current density window. Coming back to the higher current densities in Figure 5.3a, the curves are bending down, the earlier the larger the number of AST-cycles. These high-current Tafel slopes are much steeper compared to the ones obtained for lower current densities and found frequently in literature [42, 44, 91, 141, 205]. A variety of reasons for this behavior is given, like an increased mass-transport [44, 91], a reduced proton conductivity due to leaching of alloy ions into the ionomer phase [141], catalyst poisoning due to a adsorbing ionomer [201, 206] or a shift in the reaction mechanism [70, 207]. Though, an unambiguous answer to this phenomena is still missing [44]. However, in this study this is of secondary importance as the operation range of heavy duty vehicles is focused on lower current densities.

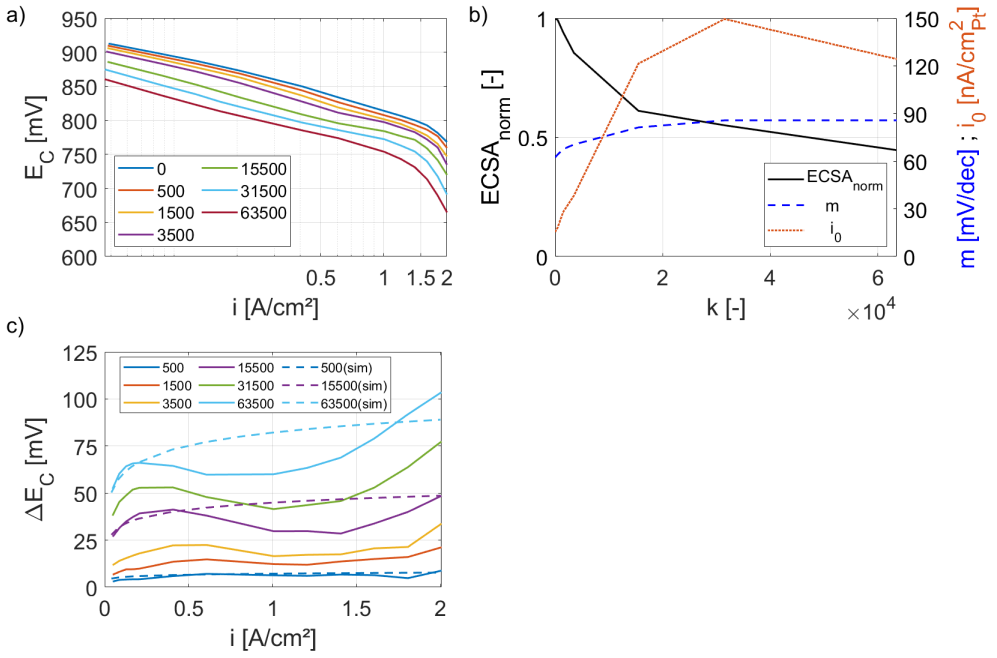

Figure 5.3: Exemplary data set obtained within the degradation process of AST 1 (see Tab. 3.2) a) Half cell voltage of the cathode; b) Measured evolution of ECSA, m and i_0 depending on the number of AST cycles k; c) Determined voltage losses (solid lines) using the calculated half cell voltages shown in (a) and simulated voltage losses (dashed lines) for k: 500, 15500 and 63500 .

In Figure 5.3c, the kinetic voltage losses are presented alongside the corresponding kinetic voltage loss simulation. After 500 AST cycles, the calculated aging-related cathode voltage losses are more or less constant over the analyzed current range. With progressing AST-cycling, this behavior changes and the losses show a wave-like behavior: The additional losses in cathode potential increase up to a current range between 0.2 and 0.6 A/cm^2 depending on the number of AST cycles. For higher current densities, in a medium range (0.3-1.4 A/cm^2), a decrease of the kinetic voltage losses can be observed, more pronounced for 15500, 31500 and 63500 AST cycles, compared to 500, 1500 and 3500 AST cycles. For even higher current densities the voltage losses increase again, rapidly.

The increase of cathode voltage loss for small current densities can be related to the increase of the kinetic overpotential with ongoing degradation [37, 42, 208] in line with the model presented in this thesis. Contrary, to this increase, the voltage losses decrease in the medium range of the current density. This observation can be related to a changed oxide formation on the active sites of the PtCo catalyst: For highly degraded MEAs, the half cell voltage for current densities

between 0.6 and 1.2 A/cm^2 falls below ~ 820 mV. Below this voltage, the influence of surface oxides on the obtained cell voltage is significantly reduced (10-30 mV) as demonstrated in Figure 4.3 [54]. These benefits from reduced oxide loadings after Pt-dissolution testing is not part of our model. Accordingly, the benefits in the medium current range can not be predicted. The rapid increase of the performance losses at even high current densities above 1.2 A/cm^2 is in line with observations made by [42, 44, 91, 141, 205] but also not part of this model. This increase can be related to the change of Tafel slope at high current densities discussed earlier, whose origins are yet to be identified unambiguously.

5.3.2 Evaluation of the ECSA loss model

In Figure 5.4 the simulated data is compared to ECSA results obtained from the AST experiments. It can be seen that the mechanistic based model presented in Chapter 5.2.1 complies with the experimental data gathered with a variety of aging conditions. With a standard deviation of 1.52~%, the model shows a good accuracy compared to the experimental data.

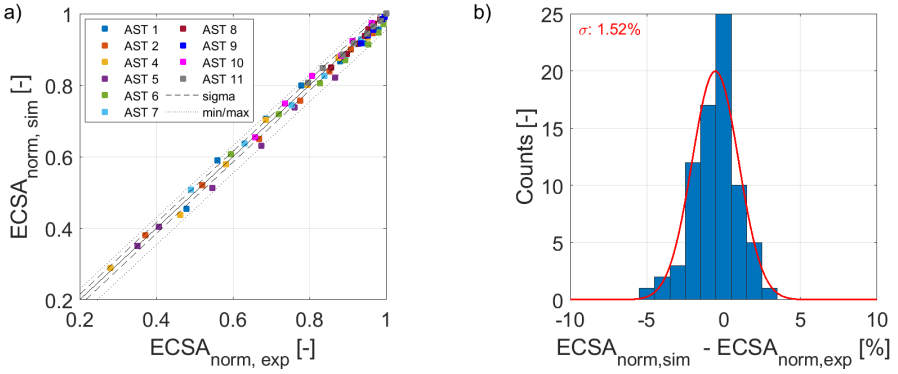

Figure 5.4: a) Comparison of the simulated and experimentally obtained electrochemical active surface area development within the accelerated stress tests. b) Histogram of the simulated and experimentally obtained electrochemical active surface area development within the accelerated stress tests.

This result shows, that the model presented in Chapter 5.2.1 can be used to describe *ECSA* losses under different operation conditions, by assuming dissolution and redeposition of the catalyst as governing degradation mechanism.

5.3.3 Correlating Tafel slope and exchange current density with ECSA

Figure 5.5 shows the experimentally determined $m(k)$ and $i_0(k)$ vs. the normalized ECSA values obtained with the different ASTs (see Tab. 3.2). In order to reduce the influence of the measurement noise and to avoid an overestimation of data points measured at high degradation rates, the measured data are averaged within $ECSA_{norm}$ steps of 10%. The resulting standard deviations are shown with the vertical and horizontal bars in Figure 5.5.

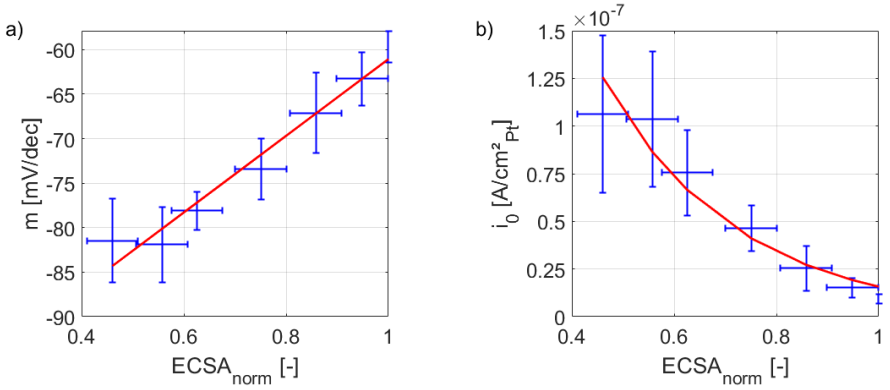

Figure 5.5: a) Correlation between average Tafel slopes and the normalized ECSA. The empirical correlation is based on a linear equation (red line). b) Correlation between averaged exchange current densities and the normalized ECSA. The empirical correlation is based on a exponential function (red line).

The potential mechanisms behind these trends were discussed earlier (see Chapter 5.3.1). It can be seen that the Tafel slope correlates linearly with $\mathrm{ECSA_{norm}}$, while the exchange current density shows an exponential dependency,

$$m(ECSA_{norm}) = p_1 \cdot ECSA_{norm} + p_2 \tag{5.13}$$

and

$$i_0(ECSA_{norm}) = p_3 \cdot e^{(p_4 \cdot ECSA_{norm})}, \tag{5.14}$$

with the parameters given in Table 5.2.

Table 5.2: Overview of the parameters used in the empirical correlations (see equations 5.13 and 5.14).

Paramter	Value	Unit
p_1	39.59	[mV/dec]
p_2	-101.19	[mV/dec]
p_3	$735.13 \cdot 10^{-}9$	[A/cm$_{Pt}{}^2$]
p_4	-3.9049	[-]

5.3.4 Evaluation of the kinetic voltage loss model with PtOx contribution

In Figure 5.6a, the accuracy of the kinetic voltage loss model is demonstrated by comparing simulated and experimental kinetic voltage losses in the range of 0-1.2 A/cm^2 (low and medium current range). The histogram shown in Figure 5.6b analyses the accuracy of the model, by presenting the difference between simulation and experiment on the x-axis and the counts of these differences on the y-axis. With a standard deviation of 5.3 mV the model describes the kinetic voltage losses in PEM-FCs with a good accuracy.
The model shows some inaccuracies especially at high kinetic voltage losses, which are related to high degrees of degradation. This can be related to a changed oxide formation on the active sites of the PtCo catalyst [54], as discussed in Chapter 5.3.1.

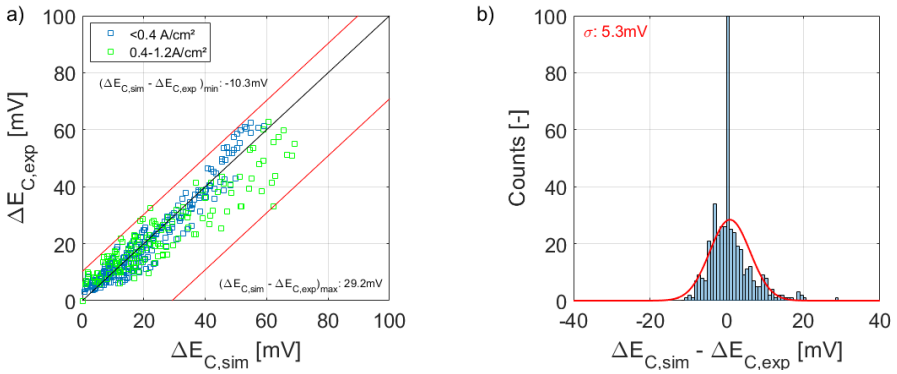

Figure 5.6: a) Comparison of the simulated and experimentally obtained degradation related performance losses in a current density range of 0-1.2 A/cm^2. The black line represents the parity line and the red lines mark the maximum under- respectively overestimation of the measured voltages losses by the model; b) Histogram of the simulated and experimentally obtained voltage losses in a range of 0-1.2 A/cm^2 with a standard deviation σ of 5.3 mV.

This can also be observed when comparing the simulated performance losses with the measured performance losses in Figure 5.3c. It can be seen, that the voltage losses in current density range between 0 and ~0.4 A/cm^2 are almost perfectly described by the model, independently from the number of AST cycles. In the medium current range (0.4-1.2 A/cm^2, represented by the green data points), the model overestimates the voltage losses, as it does not account for the changed influence of PtOx.

To get an impression whether the model is also valid over a wider range of performance, the model is analyzed for a current density range from 0 up to 2.0 A/cm^2. The result is shown in Figure 5.7.

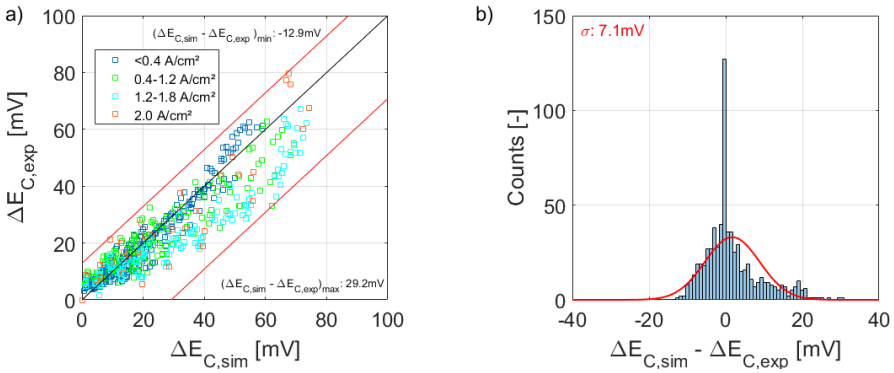

Figure 5.7: a) Comparison of the simulated and experimentally obtained degradation related performance losses in a current density range of 0-2.0 A/cm^2. The black line represents the parity line and the red lines mark the maximum under- respectively overestimation of the measured voltages losses by the model; b) Histogram of the simulated and experimentally obtained voltage losses in a range of 0-2.0 A/cm^2 with a standard deviation σ of 7.1 mV.

It can be seen that the maximal overestimation of the performance losses in Figure 5.7 (max: 29.2 mV) is identical to the values in Figure 5.6, showing that the related test points are already part of the smaller data set. For the underestimation of the voltage losses a slight increase from -10.3 mV up to -12.9 mV is obtained. Furthermore, the standard deviation increases by about 34 % from 5.3 mV to 7.1 mV. This broadening of the standard deviation is on the one hand related to a significantly increased number of data points with overestimated performance losses, at current densities between 1.2 and 1.8 A/cm^2. Especially these load points are also impacted by the changed oxide formation (shown with the cyan data points in Figure 5.7a). On the other hand the model shows a higher inaccuracy at 2.0 A/cm^2 (represented with the orange data points in Figure5.7a). At these high current densities and high degrees of degradation the change in high-current Tafel slope plays a major role (see also Figure 5.3 a and c) and the model starts to systematically underpredict the related losses. Hence, if the model was to be applied to high

current densities, e.g. in LDV, it requires an additional contribution, probably linked to the high-current Tafel slope.

5.3.5 Evaluation of kinetic voltage loss model without PtOx contribution

The Tafel approach described in Chapter 5.2.2 can also be used for the gathered the PtOx-free data. Therefore, the empirical correlations to determine the $ECSA_{norm}$ dependency of the Tafel slope and the exchange current density introduced in Chapter 5.3.3 (Equations 5.13-5.14) are derived with the PtOx-free polarization curves. The determined parameters are summarized in Table 5.3. With this correlations it is possible to simulate the kinetic voltage losses without the influence of PtOx ($\Delta E_{C,PtOx\text{-}free,sim}$).

Table 5.3: Overview of the parameters used in the empirical correlations (see equations 5.13 and 5.14).

Paramter	Value	Unit
$p_{1,PtOx-free}$	33.91	[mV/dec]
$p_{2,PtOx-free}$	-87.96	[mV/dec]
$p_{3,PtOx-free}$	$774.17 \cdot 10^{-}9$	[A/cm_{Pt}^2]
$p_{4,PtOx-free}$	-3.7417	[-]

In Figure 5.8a the accuracy of the kinetic voltage loss model is demonstrated by comparing simulated and experimental PtOx-free kinetic voltage losses in the range of 0-1.2 A/cm^2. The histogram shown in Figure 5.6b analyses the accuracy of the model, by presenting the difference between simulation and experiment on the x-axis and the counts of these differences on the y-axis. With a standard deviation of 4.9 mV the model describes the PtOx-free kinetic voltage losses in PEM-FCs also with a good accuracy (see Figure 5.8b).

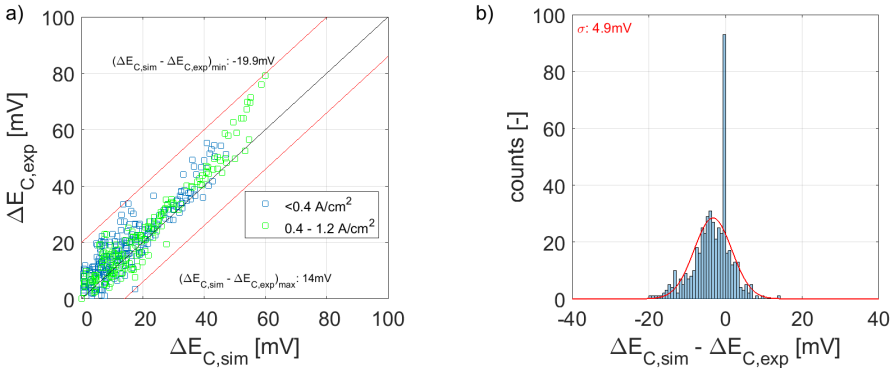

Figure 5.8: a) Comparison of the simulated and experimentally obtained degradation related performance losses, excluding the contribution of PtOx, in a current density range of 0.0-1.2 A/cm^2. The black line represents the parity line and the red lines mark the maximum under- respectively overestimation of the measured voltages losses by the model; b) Histogram of the simulated and experimentally obtained kinetic voltage losses in a range of 0-1.2 A/cm^2 with a standard deviation σ of 4.9 mV.

In contrast to the analysis in Chapter 5.3.4, where the range of 0.4–1.2 A/cm^2 was significantly affected by an unmodeled PtOx-related overpotential, the current analysis based on PtOx-free data sets demonstrates that the model is able to accurately predict the experimental $\Delta E_{C,Ptox\text{-}free}$ within this regime. This becomes evident from the close agreement of simulation and experiment in Figure 5.8a, where the vast majority of data points between 0.4–1.2 A/cm^2 (highlighted in green) lie within a narrow corridor around the parity line. This finding is in line with the conclusion drawn in Chapter 5.3.4, that the changed influence of PtOx occurring during degradation, must be considered in performance loss modeling.

To get an impression whether the PtOx-free model is also valid over a wider range of performance, the model is also analyzed for a current density range from 0 up to 2.0 A/cm^2. The result is shown in Figure 5.9. The standard deviation increases by about 20 % from 4.9 mV to 5.9 mV. In contrast to Figure 5.7a, it can be seen, that the PtOx free data sets are well predicted between 1.2 and 1.8 A/cm^2 (shown with the cyan data points). In the current density range between 1.2 and 1.8 A cm^2, and for moderate degradation levels ($\Delta E_C \leq 50$ mV), the PtOx-free model shows good agreement with the experimental data, as indicated by the cyan-coloured data points. This further validates the finding that PtOx effects must be considered in the prediction of kinetic voltage losses in PEM-FCs.

At higher current densities, however – even at 1.2 A cm^2 and under more pronounced degradation ($\Delta E_C > 50$ mV) – the model increasingly underestimates the observed voltage losses. This can also be attributed to changes in the Tafel slope that occur in the high-current region, even under PtOx-free conditions. Since such effects are also not accounted for in the PtOx-free model structure, further refinement is necessary to improve predictive accuracy in this regime.

However, PtOx-free conditions cannot be maintained during regular PEM-FC operation. Consequently, while modelling of PtOx-free states may provide theoretical insight, it seems to hold limited practical relevance.

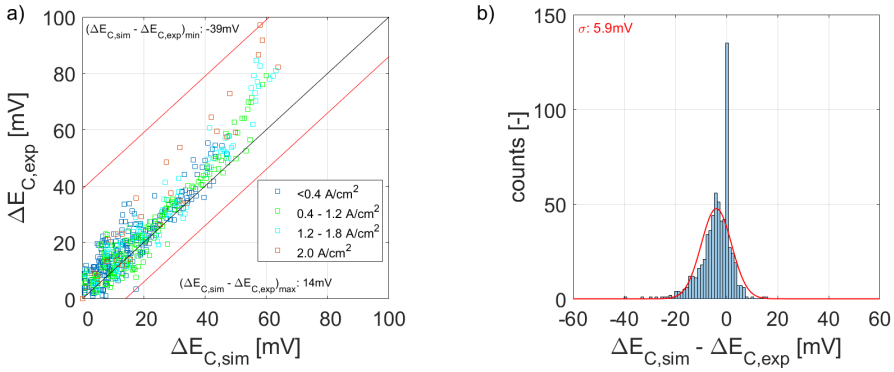

Figure 5.9: a) Comparison of the simulated and experimentally obtained degradation related performance losses, excluding the contribution of PtOx, in a current density range of 0-2.0 A/cm^2. The black line represents the parity line and the red lines mark the maximum under - respectively overestimation of the measured voltages losses by the model; b) Histogram of the simulated and experimentally obtained voltage losses in a range of 0-2.0 A/cm^2 with a standard deviation σ of 5.9 mV.

Nevertheless, this emphasizes one key result of the study: including the reduction in PtOx-related voltage losses is essential for reliably predicting fuel cell degradation under real operating conditions.

5.3.6 Deciphering the kinetic voltage loss model with PtOx contribution

The discussion is finalized by first breaking down the total loss $\Delta E_{C,sim}(k)$ into contributions arising from changes in ECSA as well as changes in m and i_0. While the former represents the impact of changes in catalyst surface area, the latter show the relevance of a changing activity parameters (as discussed in Chapter 5.3.1). Afterwards, the relevance of these contributions is discussed. Based on the generalized Tafel approach described in Chapter 5.2.2, the performance loss $\Delta E_C(k,i)$ can be split into three contributions (shown in the Appendix A.1)

$$\Delta E_{C,sim}(k,i) = \Delta\eta^{g}_{act,m}(k,i) + \Delta\eta^{g}_{act,m,i0}(k) + \Delta\eta^{g}_{act,m,ECSA}(k), \tag{5.15}$$

with the first contribution representing the overpotential change caused by a change of Tafel slope $m(k)$

$$\Delta\eta^{g}_{act,m}(k,i) = (m(k) - m(0)) \cdot log\left(\frac{i}{i_0(0) \cdot ECSA(0)}\right). \tag{5.16}$$

The second contributor describes the combined influence of $m(k)$ and $i_0(k)$ on the overpotential

$$\begin{aligned}\Delta\eta^{g}_{act,m,i0}(k) &= m(k) \cdot log\left(\frac{i_0(0)}{i_0(k)}\right) \\ &= \underbrace{m(0) \cdot log\left(\frac{i_0(0)}{i_0(k)}\right)}_{\Delta\eta^{g}_{act,m,i0,1}(k)} + \underbrace{(m(k) - m(0)) \cdot log\left(\frac{i_0(0)}{i_0(k)}\right)}_{\Delta\eta^{g}_{act,m,i0,2}(k)}.\end{aligned} \tag{5.17}$$

The third contributor combines the overpotential change due to reduced $ECSA(k)$ and the influence of $m(k)$

$$\begin{aligned}\Delta\eta^{g}_{act,m,ECSA}(k) &= m(k) \cdot log\left(\frac{ECSA(0)}{ECSA(k)}\right) \\ &= \underbrace{m(0) \cdot log\left(\frac{ECSA(0)}{ECSA(k)}\right)}_{\Delta\eta^{g}_{act,m,ECSA,1}(k)} + \underbrace{(m(k) - m(0)) \cdot log\left(\frac{ECSA(0)}{ECSA(k)}\right)}_{\Delta\eta^{g}_{act,m,ECSA,2}(k)}.\end{aligned} \tag{5.18}$$

Thereby, the differentiation into two terms indexed with "1" and "2" in Equation 5.17 is meaningfull as the two terms represent i_0-linked voltage loss contributions referred to the Tafel slope begin of life and the change of Tafel slope over the course of testing, respectively. The same applies to the ESCA-losses in Equation 5.18. Below, it can be shown, that the terms with "2" can be neglected. Accordingly, the voltage loss contributions from a change of Tafel slope, exchange current density and ECSA can be separated. Figures 5.10a, b, and c represent this deconvolution

for simulated performance losses caused by the operating conditions of AST 1 after 500, 15500 and 63500 AST cycles. To get an impression of how $\Delta\eta^g_{act,m}$ is influenced by the current density, the deconvolution is shown at 0.04, 0.2, 0.6, 1.0 and 1.8 A/cm^2. Positive values are voltage losses,which are obtained for $\Delta\eta^g_{act,m}$ and $\Delta\eta^g_{act,m,ECSA,1}$ and $\Delta\eta^g_{act,m,ECSA,2}$. Negative values can be interpreted as voltage "gains" due to a increasing i_0 (see Figure 5.1b) resulting in negative values for $\Delta\eta^g_{act,m,i_0,1}$ and $\Delta\eta^g_{act,m,i_0,2}$. Generally, it can be seen that the secondary contributions $\Delta\eta^g_{act,m,i_0,2}$ and $\Delta\eta^g_{act,m,ECSA,2}$ are of minor importance and can be neglected. Consequently, the evaluation of ΔE_C can be done by analyzing $\Delta\eta^g_{act,m,ECSA1}$ related to a reduced ECSA and the sum of "$\Delta\eta^g_{act,m} + \Delta\eta^g_{act,m,i_0,1}$", representing the impact of deallyoing or altered facet distribution. It can be seen that the voltage losses are dominated by $\Delta\eta^g_{act,m} + \Delta\eta^g_{act,m,i_0,1}$, which cause at least 50% of the voltage losses. These losses are higher than the losses caused by losses of ECSA. This conclusion is the same, no matter which AST or which cycle number is considered. Accordingly, Figure 5.10 reveals that the poorly-understood contributor to End of Life performance losses, namely change of activity, is of major importance, while well-understood losses associated with catalyst surface changes are of much lower importance.

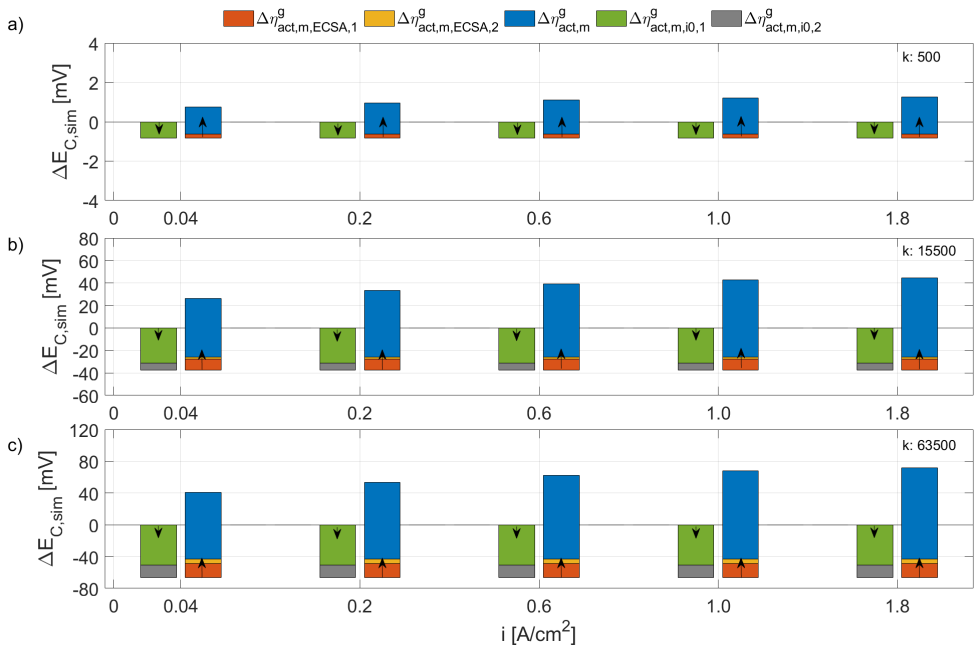

Figure 5.10: Deconvolution of kinetic voltage losses simulated with the introduced model with the operating conditions of AST 1 after: a) 500 AST cycles, representing a low level of degradation; b) 15500 AST cycles, representing a mid level of degradation and c) 63500 AST cycles, representing a high level of degradation cycles.

5.4 Concluding remark

In this Chapter 5, a model for the degradation of alloy catalysts in polymer electrolyte membrane fuel cells is developed. The model consists of two submodels, the first submodel accounts for the changes in electrochemically active surface, the second submodel accounts for changes in the activity of the catalyst material, probably caused by dealloying and changes in the distribution of crystal facets.

The changes in electrochemically active surface were modeled with a statistical physics-based model that describes the evolution of the particle radius distribution based on particle-altering processes, including dissolution and redeposition. This model was fitted to ECSA data obtained via accelerated stress tests, performed over a wide range of operating conditions. The obtained model parameters, i.e. dissolution and redeposition rate constants, were described as functions of the AST operating conditions using empirical relationships to parameterize these dependencies. With this semi-empirical ECSA loss model, the experimentally determined ECSA losses were reproduced with a standard deviation of 1.52 % in a range of 0-50 % total surface loss.

The second submodel is based on a generalized Tafel approach. It is coupled to the first submodel by using experimentally found correlations between ECSA and the Tafel parameters, namely Tafel slope and exchange current density. After parametrization, degradation was predicted for ASTs of a wide parameter range for a current range of 0.0-2.0 A/cm^2 with a standard deviation of 7.1 mV. By reducing the current density range to 0.0-1.2 A/cm^2, the accuracy of the model improves to 5.3 mV. Systematic deviations are a consequence of the voltage loss model´s simplicity. As reduced oxide loadings in a current density range between 0.6 and 1.2 A/cm^2 for degraded cathodes are ignored, the model overestimates the losses in this range. Oppositely, at higher current densities, the kinetic voltage losses are underestimated as the model disregards the possibility of a changing Tafel slope.

Furthermore, the improved agreement between model and experiment under PtOx-free conditions, as discussed in Chapter 5.3.5, underlines the validity of the proposed degradation model within the low- to medium-load range and highlights the relevance of oxide-related effects for correct interpretation of kinetic losses.

Despite these limitations, the presented model allows to interpret the kinetic voltage loss as a sum of overpotentials related to a loss of electrochemical surface area and changes of the activity. Interestingly, it was found that the performance losses for the MEA used in this work are not described sufficiently due to loss of electrochemical active surface area alone, as at least 50% of the voltage losses are caused by the overpotentials explicitly related to a changing activity parameters. Accordingly, this study shows that during cathode degradation studies of PEM-FCs, Tafel slope and exchange current density should be the most relevant metric, not the electrochemical surface area.

6 Conclusion

6.1 Summary

The aim of this work was to develop a model that can predict voltage losses caused by the aging of the cathode in PEM fuel cells (PEM-FC) used in automotive applications. These predictions can be utilized to develop operating strategies that minimize cathode aging. Existing models that account for cathode aging either focus solely on predicting losses in the electrochemically active surface area (ECSA) without translating these losses into voltage losses, or they translate these ECSA losses into voltage losses using only the Tafel equation. This approach is adequate for pure Pt catalysts with high loadings (0.25-0.4 $mg_{Pt}/^2$) in a current density range of 0 to ~1.5 A/cm^2 [42, 44, 91]. However, for practical reasons of efficiency and cost, PtCo catalysts are predominantly used. Due to their construction, these catalysts also experience structural changes affecting kinetic parameters exchange current density (i_0) and Tafel slope. These parameters are typically held constant in the classical Tafel equation. The classical approach for predicting cathode voltage losses is therefore not applicable for the employed catalyst, as it does not account for the dynamic evolution of parameters Tafel slope and i_0. The development of new models to predict voltage losses due to cathode aging is thus essential for deriving optimal operating strategies to prevent PEM-FC aging in automotive use. This study first determined which damage scenario has the most significant impact on voltage losses during cathode degradation within the examined operating window. The influence of individual factors over a cathode's lifecycle was quantified, revealing that ECSA loss due to Pt dissolution and changes in kinetic parameters i_0 and Tafel slope caused by dealloying and structural changes of the catalyst particles are responsible for the observed voltage losses. Additionally, an empirical relationship between the decrease in ECSA and changes in Tafel slope and i_0 was derived. Based on these findings, a model derived by Urchaga et al. was adapted to predict ECSA loss as a function of the chosen AST parameters [173]. By linking this ECSA loss prediction with the derived empirical relationship, the degradation-induced changes in Tafel slope and i_0 can be simultaneously predicted. To translate these changes into voltage losses, the classical Tafel approach was extended to account for the variations in Tafel slope and exchange current density. This consideration of the variable Tafel slope and exchange current density forms a promising foundation for future simulations to predict cathode degradation in Pt alloy catalysts. This consideration of the variable Tafel slope and

exchange current density forms a promising foundation for future simulations to predict cathode degradation in Pt alloy catalysts.
However, to further refine the model and enhance its accuracy, it is crucial to account for additional factors influencing voltage losses. Another significant contributor is the overpotential caused by oxide formation, firstly quantified by this work during accelerated stress tests. It was shown that the overpotential caused by oxide formation decreases over time with aging, and PtOx losses depend on the cathode potential. This study revealed that PtOx-related losses decrease at the end of the test, except at the smallest current densities. Notably, it was demonstrated that PtOx-related voltage losses exhibit almost the same dependency on half-cell voltage for all begin- and end-of-test samples. However, when PtOx-related voltage losses are considered, unassigned losses remain or even appear larger than without considering them. Interestingly, this unassigned voltage loss was not only present at the highest current densities, as found elsewhere, but showed a steady increase with current density.

6.2 Outlook

To enhance the prediction of ECSA loss, the ECSA model needs to be extended to cover a wider range of operating parameters, including voltages greater than 1 V, which are relevant for start-stop and fuel starvation scenarios. This requires additional accelerated stress tests (ASTs) in the potential range of 1 to 1.4 V. It is important to note that the simplifications used in this study's model may no longer be valid under these conditions. By incorporating these extensions, ECSA loss predictions could also be made for start-stop and fuel starvation events. Another approach involves predicting ECSA loss based not on AST cycles but on potential profiles. This would enable the prediction of platinum loss through anodic and cathodic dissolution, allowing ECSA loss predictions for arbitrary voltage profiles, including those with voltages above 1V. However, the potential impact of carbon corrosion on ECSA losses must also be considered. Schneider et al.'s study follows this approach [152].
In addition to adapting the ECSA loss model, further extensions and adjustments to the voltage loss prediction are possible. One potential enhancement is to add a component to the model that accounts for insufficiently described losses at high current densities. Based on existing theories regarding behavior at high current densities, it is conceivable that these losses are due to mass transport limitations, which are not adequately captured by the measurement method used to determine oxygen transport resistance. To test this hypothesis, the voltage loss of aged samples at current densities above a certain threshold should be analyzed at various channel pressures. If the voltage loss decreases with increasing pressure, it is likely that the limiting current measurement method used in this study inadequately describes mass transport at higher current densities. The existing data suggests that this threshold current density decreases with aging. Furthermore, the

existing model can be optimized in the range of mean current densities (0.6-1.2 A/cm^2) by correcting this range for the change in oxide potentials during aging. In order to accomplish this, it must be checked whether a dependency between PtOx overpotential and ECSA decrease exists. This allows for the definition of an additional contribution that incorporates the decreasing oxide formation during aging into the model.
Validating the proposed model for different catalyst types is crucial to ensure its robustness and applicability across various PEMFC configurations. This can be achieved experimentally by conducting a series of tests using alternative catalyst materials such as platinum-nickel (PtNi) or platinum-iridium (PtIr) alloys. Experimental validation should include comprehensive accelerated stress tests (ASTs) under varying operating conditions, similar to those used for PtCo catalysts, but tailored to the specific characteristics of the new catalysts. Techniques such as cyclic voltammetry, polarization curve measurements, and electrochemical impedance spectroscopy will be essential to monitor changes in the electrochemically active surface area (ECSA), voltage losses, and overall cell performance.
Additionally, incorporation of in-situ diagnostics and post-mortem analyses could offer deeper insights into degradation mechanisms specific to each catalyst type. In practical terms, transmission electron microscopy (TEM) and X-ray diffraction (XRD) to examine structural changes, as well as X-ray photoelectron spectroscopy (XPS) could be used to investigate surface chemical composition and therefore achieve this task. Incorporating in-situ diagnostics and post-mortem analyses is critical for understanding the physical root of why the Tafel slope changes during catalyst degradation. The Tafel slope, related to the mechanism of the oxygen reduction reaction (ORR), can vary due to structural and chemical transformations in the catalyst over time. To precisely analyze these changes, transmission electron microscopy (TEM) may be employed to observe nanostructural changes in the catalyst particles, including for example particle size growth, agglomeration, and morphological alterations [120, 133, 209]. These structural changes directly impact the catalytic sites' activity and availability, thus altering the Tafel slope. An methodical approach like X-ray diffraction (XRD) or X-ray absorption spectroscopy (XAS) could be employed to provide insights into crystallographic modifications and phase transformations [123, 124, 210–212]. These affect the catalyst's electrochemical behavior and therefore represent an additional source for variations in the Tafel slope [123]. Another approach would be to examine the surface chemical composition via X-ray photoelectron spectroscopy (XPS), thus gathering information on the oxidation states of platinum and the presence of surface contaminants or oxide layers. These surface alterations can lead to changes in reaction pathways and kinetic parameters, further affecting the Tafel slope [70, 213, 214]. Understanding these degradation mechanisms at a fundamental level allows for the identification of the exact causes of Tafel slope variations. This knowledge can guide the development of more robust catalysts and the optimization of operational strategies to mitigate these effects. Additionally, these insights provide valuable information for the refinement of predictive models, enhancing accuracy and

therefore predicting real-world behavior of catalysts under various operating conditions. By addressing these underlying physical changes, the durability and efficiency of fuel cell systems can be improved, extending their operational life and thereby boosting their commercial viability for automotive applications. The impact of this validation is significant, as it would not only confirm the generalizability and reliability of the model but also contribute to a broader understanding of the degradation phenomena associated with different catalyst materials. This in turn, could lead to the optimization of catalyst compositions and operating strategies, ultimately improving the durability and efficiency of PEM-FCs across a wider range of applications. Furthermore, successful validation could pave the way for the development of universal models, capable of predicting performance and degradation for various catalyst types, thereby accelerating the advancement of fuel cell technologies.

Bibliography

[1] A. Alaswad, A. Omran, J. R. Sodre, T. Wilberforce, G. Pignatelli, M. Dassisti, A. Baroutaji, and A. G. Olabi, "Technical and Commercial Challenges of Proton-Exchange Membrane (PEM) Fuel Cells," *Energies*, vol. 14, no. 1, p. 144, 2021.

[2] J. Curtin, C. McInerney, B. Ó Gallachóir, C. Hickey, P. Deane, and P. Deeney, "Quantifying stranding risk for fossil fuel assets and implications for renewable energy investment: A review of the literature," *Renewable and Sustainable Energy Reviews*, vol. 116, p. 109402, 2019. [Online]. Available: https://www.sciencedirect.com/science/article/pii/S1364032119306100

[3] A. Mancino, C. Menale, F. Vellucci, M. Pasquali, and R. Bubbico, "PEM Fuel Cell Applications in Road Transport," *Energies*, vol. 16, no. 17, p. 6129, 2023.

[4] D. A. Cullen, K. C. Neyerlin, R. K. Ahluwalia, R. Mukundan, K. L. More, R. L. Borup, A. Z. Weber, D. J. Myers, and A. Kusoglu, "New roads and challenges for fuel cells in heavy-duty transportation," *Nature Energy*, vol. 6, no. 5, pp. 462–474, 2021.

[5] H. Wang, R. Wang, S. Sui, T. Sun, Y. Yan, and S. Du, "Cathode Design for Proton Exchange Membrane Fuel Cells in Automotive Applications," *Automotive Innovation*, vol. 4, no. 2, pp. 144–164, 2021.

[6] Y. Wang, Y. Pang, H. Xu, A. Martinez, and K. S. Chen, "PEM Fuel cell and electrolysis cell technologies and hydrogen infrastructure development – a review," *Energy & Environmental Science*, vol. 15, no. 6, pp. 2288–2328, 2022.

[7] T. Selmi, A. Khadhraoui, and A. Cherif, "Fuel cell-based electric vehicles technologies and challenges," *Environmental science and pollution research international*, vol. 29, no. 52, pp. 78 121–78 131, 2022.

[8] Dimitrios Papageorgopoulos, DOE Hydrogen and Fuel Cell Technologies Office, "Full Cell Technologies Subprogram Overview."

[9] J. Marcinkoski, R. Vijayagopal, j. Adams, B. James, J. Kopasz, and R. Ahluwalia, "DOE Hydrogen and Fuel Cells Program Record 19006: Hydrogen Class 8 Long Haul Truck

Targets." [Online]. Available: https://www.hydrogen.energy.gov/docs/hydrogenprogramlibraries/pdfs/19006_hydrogen_class8_long_haul_truck_targets.pdf?Status=Master

[10] Dimitrios Papageorgopoulos, "Fuel Cell Technologies Overview." [Online]. Available: https://www.hydrogen.energy.gov/docs/hydrogenprogramlibraries/pdfs/plenary8_papageorgopoulos_2021_o.pdf?Status=Master

[11] A. A. Franco, S. Passot, P. Fugier, C. Anglade, E. Billy, L. Guétaz, N. Guillet, E. de Vito, and S. Mailley, "Pt[sub x]Co[sub y] Catalysts Degradation in PEFC Environments: Mechanistic Insights," *Journal of The Electrochemical Society*, vol. 156, no. 3, p. B410, 2009.

[12] C. S. Gittleman, H. Jia, E. S. de Castro, C. R. Chisholm, and Y. S. Kim, "Proton conductors for heavy-duty vehicle fuel cells," *Joule*, vol. 5, no. 7, pp. 1660–1677, 2021.

[13] S. P. Jiang and Q. Li, "Polymer Electrolyte Membrane Fuel Cells: Principles and Materials," pp. 173–228.

[14] Y. Wang, D. F. Ruiz Diaz, K. S. Chen, Z. Wang, and X. C. Adroher, "Materials, technological status, and fundamentals of PEM fuel cells – A review," *Materials Today*, vol. 32, pp. 178–203, 2020.

[15] A. Kusoglu and A. Z. Weber, "New Insights into Perfluorinated Sulfonic-Acid Ionomers," *Chemical reviews*, vol. 117, no. 3, pp. 987–1104, 2017.

[16] T. Yoshida and K. Kojima, "Toyota MIRAI Fuel Cell Vehicle and Progress Toward a Future Hydrogen Society," *Interface magazine*, vol. 24, no. 2, pp. 45–49, 2015. [Online]. Available: https://iopscience.iop.org/article/10.1149/2.F03152if/pdf

[17] D. Banham and S. Ye, "Current Status and Future Development of Catalyst Materials and Catalyst Layers for Proton Exchange Membrane Fuel Cells: An Industrial Perspective," *ACS Energy Letters*, vol. 2, no. 3, pp. 629–638, 2017.

[18] S. Mo, L. Du, Z. Huang, J. Chen, Y. Zhou, P. Wu, L. Meng, N. Wang, L. Xing, M. Zhao, Y. Yang, J. Tang, Y. Zou, and S. Ye, "Recent Advances on PEM Fuel Cells: From Key Materials to Membrane Electrode Assembly," *Electrochemical Energy Reviews*, vol. 6, no. 1, 2023.

[19] P. Kurzweil, *Brennstoffzellentechnik: Grundlagen, Komponenten, Systeme, Anwendungen // Grundlagen, Komponenten, Systeme, Anwendungen ; mit 199 Tabellen*, 2nd ed. Wiesbaden: Springer Vieweg, 2013. [Online]. Available: http://dx.doi.org/10.1007/978-3-658-00085-1

[20] P. C. Okonkwo, I. Ben Belgacem, W. Emori, and P. C. Uzoma, "Nafion degradation mechanisms in proton exchange membrane fuel cell (PEMFC) system: A review," *International Journal of Hydrogen Energy*, vol. 46, no. 55, pp. 27 956–27 973, 2021.

[21] W. Olbrich, T. Kadyk, U. Sauter, and M. Eikerling, "Modeling of wetting phenomena in cathode catalyst layers for PEM fuel cells," *Electrochimica Acta*, vol. 431, p. 140850, 2022.

[22] ——, "Review - Wetting Phenomena in Catalyst Layers of PEM Fuel Cells: Novel Approaches for Modeling and Materials Research," *Journal of The Electrochemical Society*, vol. 169, no. 5, p. 054521, 2022.

[23] H. Guo, L. Chen, S. A. Ismail, L. Jiang, S. Guo, J. Gu, X. Zhang, Y. Li, Y. Zhu, Z. Zhang, and D. Han, "Gas Diffusion Layer for Proton Exchange Membrane Fuel Cells: A Review," *Materials (Basel, Switzerland)*, vol. 15, no. 24, 2022.

[24] Y. Wang, D. F. Ruiz Diaz, K. S. Chen, Z. Wang, and X. C. Adroher, "Materials, technological status, and fundamentals of PEM fuel cells – A review," *Materials Today*, vol. 32, pp. 178–203, 2020.

[25] R. P. O'Hayre, S.-W. Cha, W. G. Colella, and F. B. Prinz, *Fuel cell fundamentals*, third edition ed. Hoboken, New Jersey: John Wiley & Sons Inc, 2016.

[26] L. Cindrella, A. M. Kannan, J. F. Lin, K. Saminathan, Y. Ho, C. W. Lin, and J. Wertz, "Gas diffusion layer for proton exchange membrane fuel cells—A review," *Journal of Power Sources*, vol. 194, no. 1, pp. 146–160, 2009.

[27] F. Lapicque, M. Belhadj, C. Bonnet, J. Pauchet, and Y. Thomas, "A critical review on gas diffusion micro and macroporous layers degradations for improved membrane fuel cell durability," *Journal of Power Sources*, vol. 336, pp. 40–53, 2016.

[28] M. P. Rodgers, L. J. Bonville, H. R. Kunz, D. K. Slattery, and J. M. Fenton, "Fuel cell perfluorinated sulfonic acid membrane degradation correlating accelerated stress testing and lifetime," *Chemical reviews*, vol. 112, no. 11, pp. 6075–6103, 2012.

[29] M. Zatoń, J. Rozière, and D. J. Jones, "Current understanding of chemical degradation mechanisms of perfluorosulfonic acid membranes and their mitigation strategies: a review," *Sustainable Energy & Fuels*, vol. 1, no. 3, pp. 409–438, 2017.

[30] K. I. Jeong, J. Oh, S. A. Song, D. Lee, D. G. Lee, and S. S. Kim, "A review of composite bipolar plates in proton exchange membrane fuel cells: Electrical properties and gas permeability," *Composite Structures*, vol. 262, p. 113617, 2021.

[31] Y. Leng, P. Ming, D. Yang, and C. Zhang, "Stainless steel bipolar plates for proton exchange membrane fuel cells: Materials, flow channel design and forming processes," *Journal of Power Sources*, vol. 451, p. 227783, 2020.

[32] Y. Song, C. Zhang, C.-Y. Ling, M. Han, R.-Y. Yong, D. Sun, and J. Chen, "Review on current research of materials, fabrication and application for bipolar plate in proton exchange membrane fuel cell," *International Journal of Hydrogen Energy*, vol. 45, no. 54, pp. 29 832–29 847, 2020.

[33] X. Li, "Bipolar plates and flow field design," in *Fuel Cells for Transportation // FUEL CELLS FOR TRANSPORTATION*. S.l.: Elsevier and WOODHEAD PUBLISHING, 2023, pp. 305–337.

[34] P. Sharma and O. P. Pandey, "Proton exchange membrane fuel cells: fundamentals, advanced technologies, and practical applications," in *PEM Fuel Cells*. Elsevier, 2022, pp. 1–24.

[35] S. P. Jiang and Q. Li, "Fuel Cell Thermodynamics," in *Introduction to Fuel Cells*, S. P. Jiang and Q. Li, Eds. Singapore: Springer Singapore, 2022, pp. 27–68.

[36] M. Eikerling and A. Kulikovsky, *Polymer Electrolyte Fuel Cells*. CRC Press, 2014.

[37] D. D. Papadias, R. K. Ahluwalia, N. Kariuki, D. Myers, K. L. More, D. A. Cullen, B. T. Sneed, K. C. Neyerlin, R. Mukundan, and R. L. Borup, "Durability of Pt-Co Alloy Polymer Electrolyte Fuel Cell Cathode Catalysts under Accelerated Stress Tests," *Journal of The Electrochemical Society*, vol. 165, no. 6, pp. F3166–F3177, 2018.

[38] O. E. Herrera, D. P. Wilkinson, and W. Mérida, "Anode and cathode overpotentials and temperature profiles in a PEMFC," *Journal of Power Sources*, vol. 198, pp. 132–142, 2012.

[39] S. P. Jiang and Q. Li, "Fuel Cell Electrochemistry," in *Introduction to Fuel Cells*, S. P. Jiang and Q. Li, Eds. Singapore: Springer Singapore, 2022, pp. 69–122.

[40] D. Stolten, Ed., *Hydrogen and fuel cells: Fundamentals, technologies and applications ; contributions to the 18th World Hydrogen Energy Conference 2010, Essen*, 2nd ed. Weinheim: Wiley-VCH, 2011. [Online]. Available: https://application.wiley-vch.de/books/sample/3527327118_c01.pdf

[41] O. T. Holton and J. W. Stevenson, "The Role of Platinum in Proton Exchange Membrane Fuel Cells," *Platinum Metals Review*, vol. 57, no. 4, pp. 259–271, 2013. [Online]. Available: https://www.ingentaconnect.com/content/matthey/pmr/2013/00000057/00000004/art00002?crawler=true

[42] P. Zihrul, I. Hartung, S. Kirsch, G. Huebner, F. Hasché, and H. A. Gasteiger, "Voltage Cycling Induced Losses in Electrochemically Active Surface Area and in H2 /Air-Performance of PEM Fuel Cells // Voltage Cycling Induced Losses in Electrochemically Active Surface Area and in H 2 /Air-Performance of PEM Fuel Cells," *Journal of The Electrochemical Society*, vol. 163, no. 6, pp. F492–F498, 2016.

[43] N. P. Subramanian, T. A. Greszler, J. Zhang, W. Gu, R. Makharia, and J. Zhang, "Pt-Oxide Coverage-Dependent Oxygen Reduction Reaction (ORR) Kinetics," *Journal of The Electrochemical Society*, vol. 159, no. 5, pp. B531–B540, 2012.

[44] G. S. Harzer, J. N. Schwämmlein, A. M. Damjanović, S. Ghosh, and H. A. Gasteiger, "Cathode Loading Impact on Voltage Cycling Induced PEMFC Degradation: A Voltage Loss Analysis," *Journal of The Electrochemical Society*, vol. 165, no. 6, pp. F3118–F3131, 2018.

[45] T. A. Greszler, D. Caulk, and P. Sinha, "The Impact of Platinum Loading on Oxygen Transport Resistance," *Journal of The Electrochemical Society*, vol. 159, no. 12, pp. F831–F840, 2012.

[46] P. Zihrul, "Untersuchungen zur Aktivität und Stabilität von Membran-Elektroden-Einheiten für PEM-Brennstoffzellen," Ph.D. dissertation, Technische Universität München. [Online]. Available: https://mediatum.ub.tum.de/1449745

[47] W. Gu, D. R. Baker, Y. Liu, and H. A. Gasteiger, "Proton exchange membrane fuel cell (PEMFC) down–the–channel performance model," in *Handbook of fuel cells*, W. Vielstich, Ed. Hoboken, NJ: Wiley Interscience, 2010.

[48] K. C. Neyerlin, W. Gu, J. Jorne, and H. A. Gasteiger, "Determination of Catalyst Unique Parameters for the Oxygen Reduction Reaction in a PEMFC," *Journal of The Electrochemical Society*, vol. 153, no. 10, p. A1955, 2006. [Online]. Available: https://iopscience.iop.org/article/10.1149/1.2266294/pdf

[49] D. R. Baker, D. A. Caulk, K. C. Neyerlin, and M. W. Murphy, "Measurement of Oxygen Transport Resistance in PEM Fuel Cells by Limiting Current Methods," *Journal of The Electrochemical Society*, vol. 156, no. 9, p. B991, 2009.

[50] M. Göbel, S. Kirsch, L. Schwarze, L. Schmidt, H. Scholz, J. Haußmann, M. Klages, J. Scholta, H. Markötter, S. Alrwashdeh, I. Manke, and B. R. Müller, "Transient limiting current measurements for characterization of gas diffusion layers," *Journal of Power Sources*, vol. 402, pp. 237–245, 2018. [Online]. Available: https://chemistry-europe.onlinelibrary.wiley.com/doi/pdfdirect/10.1002/elsa.202100049?download=true

[51] R. Makharia, M. F. Mathias, and D. R. Baker, "Measurement of Catalyst Layer Electrolyte Resistance in PEFCs Using Electrochemical Impedance Spectroscopy," *Journal of The Electrochemical Society*, vol. 152, no. 5, p. A970, 2005.

[52] Thomas Gaumont, G. Maranzana, Olivier Lottin, Jérôme Dillet, Sophie Didierjean, J Pauchet, L Guétaz, T. Gaumont, G. Maranzana, O. Lottin, J. Dillet, S. Didierjean, J. Pauchet, and L. Guétaz, "Measurement of protonic resistance of catalyst layers as a tool for degradation monitoring," *International Journal of Hydrogen Energy*, vol. 42, no. 3, pp. 1800–1812, 2017.

[53] S. Jomori, N. Nonoyama, and T. Yoshida, "Analysis and modeling of PEMFC degradation: Effect on oxygen transport," *Journal of Power Sources*, vol. 215, pp. 18–27, 2012.

[54] D. Bernhard, T. Kadyk, U. Krewer, and S. Kirsch, "How platinum oxide affects the degradation analysis of PEM fuel cell cathodes," *International Journal of Hydrogen Energy*, vol. 46, no. 26, pp. 13 791–13 805, 2021.

[55] M. J. Eckl, Y. Mattausch, C. K. Jung, S. Kirsch, L. Schmidt, G. Huebner, J. E. Mueller, L. A. Kibler, and T. Jacob, "The influence of platinum surface oxidation on the performance of a polymer electrolyte membrane fuel cell—probing changes of catalytically active surface sites on a polycrystalline platinum electrode for the oxygen reduction reaction," *Electrochemical Science Advances*, vol. 2, no. 3, 2022.

[56] J. X. Wang, N. M. Markovic, and R. R. Adzic, "Kinetic Analysis of Oxygen Reduction on Pt(111) in Acid Solutions: Intrinsic Kinetic Parameters and Anion Adsorption Effects," *The Journal of Physical Chemistry B*, vol. 108, no. 13, pp. 4127–4133, 2004.

[57] B. Kirchhoff, L. Braunwarth, C. Jung, H. Jónsson, D. Fantauzzi, and T. Jacob, "Simulations of the Oxidation and Degradation of Platinum Electrocatalysts," *Small (Weinheim an der Bergstrasse, Germany)*, vol. 16, no. 5, p. e1905159, 2020.

[58] B. Kirchhoff, C. Jung, H. Jónsson, D. Fantauzzi, and T. Jacob, "Simulations of the Electrochemical Oxidation of Pt Nanoparticles of Various Shapes," *The Journal of Physical Chemistry C*, vol. 126, no. 15, pp. 6773–6781, 2022.

[59] S. Arisetty, Y. Liu, W. Gu, and M. Mathias, "Modeling Platinum Oxide Growth of PEMFC Cathode Catalysts," *ECS Transactions*, vol. 69, no. 17, pp. 273–289, 2015.

[60] Y. Takagi, H. Wang, Y. Uemura, T. Nakamura, L. Yu, O. Sekizawa, T. Uruga, M. Tada, G. Samjeské, Y. Iwasawa, and T. Yokoyama, "In situ study of oxidation states of platinum nanoparticles on a polymer electrolyte fuel cell electrode by near ambient

pressure hard X-ray photoelectron spectroscopy," *Physical chemistry chemical physics : PCCP*, vol. 19, no. 8, pp. 6013–6021, 2017.

[61] T. Suzuki and Y. Morimoto, "Kinetics of Oxide Formation and Reduction at Pt Catalyst in Polymer Electrolyte Fuel Cells," *Electrochemistry*, vol. 84, no. 7, pp. 511–515, 2016.

[62] G. Jerkiewicz, G. Vatankhah, J. Lessard, M. P. Soriaga, and Y.-S. Park, "Surface-oxide growth at platinum electrodes in aqueous H2SO4," *Electrochimica Acta*, vol. 49, no. 9-10, pp. 1451–1459, 2004.

[63] E. L. Redmond, B. P. Setzler, F. M. Alamgir, and T. F. Fuller, "Elucidating the oxide growth mechanism on platinum at the cathode in PEM fuel cells," *Physical chemistry chemical physics : PCCP*, vol. 16, no. 11, pp. 5301–5311, 2014.

[64] S. G. Rinaldo, W. Lee, J. Stumper, and M. Eikerling, "Mechanistic Principles of Platinum Oxide Formation and Reduction," *Electrocatalysis*, vol. 5, no. 3, pp. 262–272, 2014.

[65] M. Alsabet, M. Grden, and G. Jerkiewicz, "Comprehensive study of the growth of thin oxide layers on Pt electrodes under well-defined temperature, potential, and time conditions," *Journal of Electroanalytical Chemistry*, vol. 589, no. 1, pp. 120–127, 2006.

[66] A. M. Gómez-Marín, J. Clavilier, and J. M. Feliu, "Sequential Pt(111) oxide formation in perchloric acid: An electrochemical study of surface species inter-conversion," *Journal of Electroanalytical Chemistry*, vol. 688, pp. 360–370, 2013.

[67] B. E. Conway, B. Barnett, H. Angerstein-Kozlowska, and B. V. Tilak, "A surface–electrochemical basis for the direct logarithmic growth law for initial stages of extension of anodic oxide films formed at noble metals," *The Journal of chemical physics*, vol. 93, no. 11, pp. 8361–8373, 1990.

[68] A. Kongkanand and J. M. Ziegelbauer, "Surface Platinum Electrooxidation in the Presence of Oxygen," *The Journal of Physical Chemistry C*, vol. 116, no. 5, pp. 3684–3693, 2012.

[69] M. J. Eslamibidgoli and M. H. Eikerling, "Atomistic Mechanism of Pt Extraction at Oxidized Surfaces: Insights from DFT," *Electrocatalysis*, vol. 7, no. 4, pp. 345–354, 2016.

[70] J. Huang, J. Zhang, and M. Eikerling, "Unifying theoretical framework for deciphering the oxygen reduction reaction on platinum," *Physical Chemistry Chemical Physics*, vol. 20, no. 17, pp. 11 776–11 786, 2018.

[71] J. X. Wang, J. Zhang, and R. R. Adzic, "Double-trap kinetic equation for the oxygen reduction reaction on Pt(111) in acidic media," *The journal of physical chemistry. A*, vol. 111, no. 49, pp. 12 702–12 710, 2007.

[72] J. X. Wang, F. A. Uribe, T. E. Springer, J. Zhang, and R. R. Adzic, "Intrinsic kinetic equation for oxygen reduction reaction in acidic media: the double Tafel slope and fuel cell applications," *Faraday discussions*, vol. 140, pp. 347–62; discussion 417–37, 2008.

[73] M. Markiewicz, C. Zalitis, and A. Kucernak, "Performance measurements and modelling of the ORR on fuel cell electrocatalysts – the modified double trap model," *Electrochimica Acta*, vol. 179, pp. 126–136, 2015.

[74] A. Orfanidi, P. Madkikar, H. A. El-Sayed, G. S. Harzer, T. Kratky, and H. A. Gasteiger, "The Key to High Performance Low Pt Loaded Electrodes," *Journal of The Electrochemical Society*, vol. 164, no. 4, pp. F418–F426, 2017.

[75] A. Kneer, J. Jankovic, D. Susac, A. Putz, N. Wagner, M. Sabharwal, and M. Secanell, "Correlation of Changes in Electrochemical and Structural Parameters due to Voltage Cycling Induced Degradation in PEM Fuel Cells," *Journal of The Electrochemical Society*, vol. 165, no. 6, pp. F3241–F3250, 2018.

[76] J. P. Owejan, J. E. Owejan, and W. Gu, "Impact of Platinum Loading and Catalyst Layer Structure on PEMFC Performance," *Journal of The Electrochemical Society*, vol. 160, no. 8, pp. F824–F833, 2013.

[77] A. Z. Weber and A. Kusoglu, "Unexplained transport resistances for low-loaded fuel-cell catalyst layers," *J. Mater. Chem. A*, vol. 2, no. 41, pp. 17 207–17 211, 2014.

[78] C. Gerling, M. Hanauer, U. Berner, and K. Andreas Friedrich, "PEM Single Cells under Differential Conditions: Full Factorial Parameterization of the ORR and HOR Kinetics and Loss Analysis," *Journal of The Electrochemical Society*, vol. 169, no. 1, p. 014503, 2022.

[79] J. Zhang, *PEM fuel cell electrocatalysts and catalyst layers // PEM Fuel Cell Electrocatalysts and Catalyst Layers: Fundamentals and applications // Fundamentals and Applications*. London: Springer and Springer-Verlag, 2008.

[80] F. A. de Bruijn, V. A. T. Dam, and G. J. M. Janssen, "Review: Durability and Degradation Issues of PEM Fuel Cell Components," *Fuel Cells*, vol. 8, no. 1, pp. 3–22, 2008.

[81] M. Moein-Jahromi, M. J. Kermani, and S. Movahed, "Degradation forecast for PEMFC cathode-catalysts under cyclic loads," *Journal of Power Sources*, vol. 359, pp. 611–625, 2017.

[82] S. S. Araya, N. Li, and V. Liso, “Degradation and failure modes in proton exchange membrane fuel cells,” in *PEM Fuel Cells*. Elsevier, 2022, pp. 199–222.

[83] M. Mayur, M. Gerard, P. Schott, and W. Bessler, “Lifetime Prediction of a Polymer Electrolyte Membrane Fuel Cell under Automotive Load Cycling Using a Physically-Based Catalyst Degradation Model,” *Energies*, vol. 11, no. 8, p. 2054, 2018.

[84] X.-Z. Yuan, H. Li, S. Zhang, J. Martin, and H. Wang, “A review of polymer electrolyte membrane fuel cell durability test protocols,” *Journal of Power Sources*, vol. 196, no. 22, pp. 9107–9116, 2011.

[85] C. Lim, L. Ghassemzadeh, F. van Hove, M. Lauritzen, J. Kolodziej, G. G. Wang, S. Holdcroft, and E. Kjeang, “Membrane degradation during combined chemical and mechanical accelerated stress testing of polymer electrolyte fuel cells,” *Journal of Power Sources*, vol. 257, pp. 102–110, 2014.

[86] M. G. George, H. Liu, D. Muirhead, R. Banerjee, N. Ge, P. Shrestha, J. Lee, S. Chevalier, J. Hinebaugh, M. Messerschmidt, R. Zeis, J. Scholta, and A. Bazylak, “Accelerated Degradation of Polymer Electrolyte Membrane Fuel Cell Gas Diffusion Layers,” *Journal of The Electrochemical Society*, vol. 164, no. 7, pp. F714–F721, 2017.

[87] H. Liu, M. G. George, N. Ge, D. Muirhead, P. Shrestha, J. Lee, R. Banerjee, R. Zeis, M. Messerschmidt, J. Scholta, P. Krolla, and A. Bazylak, “Microporous Layer Degradation in Polymer Electrolyte Membrane Fuel Cells,” *Journal of The Electrochemical Society*, vol. 165, no. 6, pp. F3271–F3280, 2018.

[88] J. Park, H. Oh, T. Ha, Y. I. Lee, and K. Min, “A review of the gas diffusion layer in proton exchange membrane fuel cells: Durability and degradation,” *Applied Energy*, vol. 155, pp. 866–880, 2015.

[89] Y. Pan, H. Wang, and N. P. Brandon, “Gas diffusion layer degradation in proton exchange membrane fuel cells: Mechanisms, characterization techniques and modelling approaches,” *Journal of Power Sources*, vol. 513, p. 230560, 2021.

[90] T. Jahnke, G. A. Futter, A. Baricci, C. Rabissi, and A. Casalegno, “Physical Modeling of Catalyst Degradation in Low Temperature Fuel Cells: Platinum Oxidation, Dissolution, Particle Growth and Platinum Band Formation,” *Journal of The Electrochemical Society*, vol. 167, no. 1, p. 013523, 2019.

[91] A. Kneer and N. Wagner, “A Semi-Empirical Catalyst Degradation Model Based on Voltage Cycling under Automotive Operating Conditions in PEM Fuel Cells,” *Journal of The Electrochemical Society*, vol. 166, no. 2, pp. F120–F127, 2019.

[92] H. Chen, Z. Zhan, P. Jiang, Y. Sun, L. Liao, X. Wan, Q. Du, X. Chen, H. Song, R. Zhu, Z. Shu, S. Li, and M. Pan, "Whole life cycle performance degradation test and RUL prediction research of fuel cell MEA," *Applied Energy*, vol. 310, p. 118556, 2022.

[93] R. K. F. Della Bella, B. M. Stühmeier, and H. A. Gasteiger, "Universal Correlation between Cathode Roughness Factor and H 2 /Air Performance Losses in Voltage Cycling-Based Accelerated Stress Tests," *Journal of The Electrochemical Society*, vol. 169, no. 4, p. 044528, 2022.

[94] D. J. Myers, X. Wang, M. C. Smith, and K. L. More, "Potentiostatic and Potential Cycling Dissolution of Polycrystalline Platinum and Platinum Nano-Particle Fuel Cell Catalysts," *Journal of The Electrochemical Society*, vol. 165, no. 6, pp. F3178–F3190, 2018.

[95] J. C. Meier, C. Galeano, I. Katsounaros, J. Witte, H. J. Bongard, A. A. Topalov, C. Baldizzone, S. Mezzavilla, F. Schüth, and K. J. J. Mayrhofer, "Design criteria for stable Pt/C fuel cell catalysts," *Beilstein journal of nanotechnology*, vol. 5, pp. 44–67, 2014.

[96] Y. Yu, H. Li, H. Wang, X.-Z. Yuan, G. Wang, and M. Pan, "A review on performance degradation of proton exchange membrane fuel cells during startup and shutdown processes: Causes, consequences, and mitigation strategies," *Journal of Power Sources*, vol. 205, pp. 10–23, 2012.

[97] T. Mittermeier, A. Weiß, F. Hasché, and H. A. Gasteiger, "PEM Fuel Cell Start-Up/Shut-Down Losses vs Relative Humidity: The Impact of Water in the Electrode Layer on Carbon Corrosion," *Journal of The Electrochemical Society*, vol. 165, no. 16, pp. F1349–F1357, 2018.

[98] R. K. Ahluwalia, D. D. Papadias, N. N. Kariuki, J.-K. Peng, X. Wang, Y. Tsai, D. G. Graczyk, and D. J. Myers, "Potential Dependence of Pt and Co Dissolution from Platinum-Cobalt Alloy PEFC Catalysts Using Time-Resolved Measurements," *Journal of The Electrochemical Society*, vol. 165, no. 6, pp. F3024–F3035, 2018.

[99] J. C. Meier, C. Galeano, I. Katsounaros, J. Witte, H. J. Bongard, A. A. Topalov, C. Baldizzone, S. Mezzavilla, F. Schüth, and K. J. J. Mayrhofer, "Design criteria for stable Pt/C fuel cell catalysts," *Beilstein journal of nanotechnology*, vol. 5, pp. 44–67, 2014.

[100] R. K. Ahluwalia, X. Wang, J.-K. Peng, N. N. Kariuki, D. J. Myers, S. Rasouli, P. J. Ferreira, Z. Yang, A. Martinez-Bonastre, D. Fongalland, and J. Sharman, "Durability of De-Alloyed Platinum-Nickel Cathode Catalyst in Low Platinum Loading

Membrane-Electrode Assemblies Subjected to Accelerated Stress Tests," *Journal of The Electrochemical Society*, vol. 165, no. 6, pp. F3316–F3327, 2018.

[101] E. Padgett, V. Yarlagadda, M. E. Holtz, M. Ko, B. D. A. Levin, R. S. Kukreja, J. M. Ziegelbauer, R. N. Andrews, J. Ilavsky, A. Kongkanand, and D. A. Muller, "Mitigation of PEM Fuel Cell Catalyst Degradation with Porous Carbon Supports," *Journal of The Electrochemical Society*, vol. 166, no. 4, pp. F198–F207, 2019.

[102] A. A. Topalov, S. Cherevko, A. R. Zeradjanin, J. C. Meier, I. Katsounaros, and K. J. J. Mayrhofer, "Towards a comprehensive understanding of platinum dissolution in acidic media," *Chem. Sci.*, vol. 5, no. 2, pp. 631–638, 2014. [Online]. Available: https://pubs.rsc.org/en/content/articlepdf/2014/sc/c3sc52411f

[103] S. Cherevko, G. P. Keeley, S. Geiger, A. R. Zeradjanin, N. Hodnik, N. Kulyk, and K. J. J. Mayrhofer, "Dissolution of Platinum in the Operational Range of Fuel Cells," *ChemElectroChem*, vol. 2, no. 10, pp. 1471–1478, 2015.

[104] S. Cherevko, N. Kulyk, and K. J. Mayrhofer, "Durability of platinum-based fuel cell electrocatalysts: Dissolution of bulk and nanoscale platinum," *Nano Energy*, vol. 29, pp. 275–298, 2016.

[105] D. J. S. Sandbeck, O. Brummel, K. J. J. Mayrhofer, J. Libuda, I. Katsounaros, and S. Cherevko, "Dissolution of Platinum Single Crystals in Acidic Medium," *Chemphyschem : a European journal of chemical physics and physical chemistry*, vol. 20, no. 22, pp. 2997–3003, 2019.

[106] A. Kneer, N. Wagner, C. Sadeler, A.-C. Scherzer, and D. Gerteisen, "Effect of Dwell Time and Scan Rate during Voltage Cycling on Catalyst Degradation in PEM Fuel Cells," *Journal of The Electrochemical Society*, vol. 165, no. 10, pp. F805–F812, 2018.

[107] P. Ren, P. Pei, Y. Li, Z. Wu, D. Chen, and S. Huang, "Degradation mechanisms of proton exchange membrane fuel cell under typical automotive operating conditions," *Progress in Energy and Combustion Science*, vol. 80, p. 100859, 2020.

[108] Z. Duan and G. Henkelman, "Atomic-Scale Mechanisms of Electrochemical Pt Dissolution," *ACS Catalysis*, vol. 11, no. 23, pp. 14 439–14 447, 2021.

[109] Josef Christian Meier, "Degradation phenomena and design principles for stable and active Pt/C fuel cell catalysts," Ph.D. dissertation, Ruhr-Universität Bochum, Universitätsbibliothek, 2014.

[110] L. Castanheira, W. O. Silva, F. H. Lima, A. Crisci, L. Dubau, and F. Maillard, "Carbon Corrosion in Proton-Exchange Membrane Fuel Cells: Effect of the Carbon Structure, the

Degradation Protocol, and the Gas Atmosphere," *ACS Catalysis*, vol. 5, no. 4, pp. 2184–2194, 2015.

[111] N. Yousfi-Steiner, P. Moçotéguy, D. Candusso, and D. Hissel, "A review on polymer electrolyte membrane fuel cell catalyst degradation and starvation issues: Causes, consequences and diagnostic for mitigation," *Journal of Power Sources*, vol. 194, no. 1, pp. 130–145, 2009.

[112] J. Zhao, Z. Tu, and S. H. Chan, "Carbon corrosion mechanism and mitigation strategies in a proton exchange membrane fuel cell (PEMFC): A review," *Journal of Power Sources*, vol. 488, p. 229434, 2021.

[113] N. Linse, "Start/stop phenomena in polymer electrolyte fuel cells," Ph.D. dissertation, ETH Zurich, 2012.

[114] H. Schulenburg, B. Schwanitz, N. Linse, G. G. Scherer, A. Wokaun, J. Krbanjevic, R. Grothausmann, and I. Manke, "3D Imaging of Catalyst Support Corrosion in Polymer Electrolyte Fuel Cells," *The Journal of Physical Chemistry C*, vol. 115, no. 29, pp. 14 236–14 243, 2011.

[115] S. Maass, F. Finsterwalder, G. Frank, R. Hartmann, and C. Merten, "Carbon support oxidation in PEM fuel cell cathodes," *Journal of Power Sources*, vol. 176, no. 2, pp. 444–451, 2008.

[116] J. Zhao, X. Li, C. Shum, and J. McPhee, "A Review of physics-based and data-driven models for real-time control of polymer electrolyte membrane fuel cells," *Energy and AI*, vol. 6, p. 100114, 2021.

[117] J. C. Meier, C. Galeano, I. Katsounaros, A. A. Topalov, A. Kostka, F. Schüth, and K. J. J. Mayrhofer, "Degradation Mechanisms of Pt/C Fuel Cell Catalysts under Simulated Start–Stop Conditions," *ACS Catalysis*, vol. 2, no. 5, pp. 832–843, 2012.

[118] H. Tang, Z. Qi, M. Ramani, and J. F. Elter, "PEM fuel cell cathode carbon corrosion due to the formation of air/fuel boundary at the anode," *Journal of Power Sources*, vol. 158, no. 2, pp. 1306–1312, 2006.

[119] L. Wang, W. Gao, Z. Liu, Z. Zeng, Y. Liu, M. Giroux, M. Chi, G. Wang, J. Greeley, X. Pan, and C. Wang, "Core–Shell Nanostructured Cobalt–Platinum Electrocatalysts with Enhanced Durability," *ACS Catalysis*, vol. 8, no. 1, pp. 35–42, 2018.

[120] H. L. Xin, S. Alayoglu, R. Tao, A. Genc, C.-M. Wang, L. Kovarik, E. A. Stach, L.-W. Wang, M. Salmeron, G. A. Somorjai, and H. Zheng, "Revealing the atomic restructuring of Pt-Co nanoparticles," *Nano letters*, vol. 14, no. 6, pp. 3203–3207, 2014. [Online]. Available: https://pubs.acs.org/doi/pdf/10.1021/nl500553a

[121] S. Takahashi, N. Takahashi, N. Todoroki, and T. Wadayama, "Dealloying of Nitrogen-Introduced Pt-Co Alloy Nanoparticles: Preferential Core-Shell Formation with Enhanced Activity for Oxygen Reduction Reaction," *ACS omega*, vol. 1, no. 6, pp. 1247–1252, 2016.

[122] Laetitia Dubau, Miguel Lopez-Haro, Luis Castanheira, Julien Durst, Marian Chatenet, Pascale Bayle-Guillemaud, Laure Guétaz, Nicolas Caqué, Elisabeth Rossinot, and Frédéric Maillard, "Probing the structure, the composition and the ORR activity of Pt3Co/C nanocrystallites during a 3422h PEMFC ageing test."

[123] J. A. Gilbert, A. J. Kropf, N. N. Kariuki, S. DeCrane, X. Wang, S. Rasouli, K. Yu, P. J. Ferreira, D. Morgan, and D. J. Myers, "In-Operando Anomalous Small-Angle X-Ray Scattering Investigation of Pt 3 Co Catalyst Degradation in Aqueous and Fuel Cell Environments," *Journal of The Electrochemical Society*, vol. 162, no. 14, pp. F1487–F1497, 2015.

[124] Q. Jia, K. Caldwell, K. Strickland, J. M. Ziegelbauer, Z. Liu, Z. Yu, D. E. Ramaker, and S. Mukerjee, "Improved Oxygen Reduction Activity and Durability of Dealloyed PtCo x Catalysts for Proton Exchange Membrane Fuel Cells: Strain, Ligand, and Particle Size Effects," *ACS Catalysis*, vol. 5, no. 1, pp. 176–186, 2015.

[125] Q. Jia, W. Liang, M. K. Bates, P. Mani, W. Lee, and S. Mukerjee, "Activity descriptor identification for oxygen reduction on platinum-based bimetallic nanoparticles: in situ observation of the linear composition-strain-activity relationship," *ACS nano*, vol. 9, no. 1, pp. 387–400, 2015.

[126] P. Strasser, S. Koh, T. Anniyev, J. Greeley, K. More, C. Yu, Z. Liu, S. Kaya, D. Nordlund, H. Ogasawara, M. F. Toney, and A. Nilsson, "Lattice-strain control of the activity in dealloyed core-shell fuel cell catalysts," *Nature chemistry*, vol. 2, no. 6, pp. 454–460, 2010.

[127] J. R. Kitchin, J. K. Nørskov, M. A. Barteau, and J. G. Chen, "Role of strain and ligand effects in the modification of the electronic and chemical properties of bimetallic surfaces," *Physical review letters*, vol. 93, no. 15, p. 156801, 2004.

[128] ——, "Modification of the surface electronic and chemical properties of Pt(111) by subsurface 3d transition metals," *The Journal of chemical physics*, vol. 120, no. 21, pp. 10 240–10 246, 2004.

[129] L. Su, W. Jia, C.-M. Li, and Y. Lei, "Mechanisms for enhanced performance of platinum-based electrocatalysts in proton exchange membrane fuel cells," *ChemSusChem*, vol. 7, no. 2, pp. 361–378, 2014.

[130] L. PC, Z. Ma, Z. P. Cano, A. Yu, Z. Chen, G. Jiang, X. Fu, L. Yang, T. Wu, Z. Bai, and J. Lu, "Enhancing Oxygen Reduction Activity of Pt-based Electrocatalysts: From Theoretical Mechanisms to Practical Methods," *Angewandte Chemie (International ed. in English)*, vol. 59, no. 42, pp. 18 334–18 348, 2020. [Online]. Available: https://www.osti.gov/servlets/purl/1804068

[131] L. Tao, K. Wang, F. Lv, H. Mi, F. Lin, H. Luo, H. Guo, Q. Zhang, L. Gu, M. Luo, and S. Guo, "Precise synthetic control of exclusive ligand effect boosts oxygen reduction catalysis," *Nature communications*, vol. 14, no. 1, p. 6893, 2023.

[132] F. Hasché, M. Oezaslan, and P. Strasser, "Activity, Structure and Degradation of Dealloyed PtNi 3 Nanoparticle Electrocatalyst for the Oxygen Reduction Reaction in PEMFC," *Journal of The Electrochemical Society*, vol. 159, no. 1, pp. B24–B33, 2011.

[133] F. R. Nikkuni, L. Dubau, E. A. Ticianelli, and M. Chatenet, "Accelerated degradation of Pt3Co/C and Pt/C electrocatalysts studied by identical-location transmission electron microscopy in polymer electrolyte environment," *Applied Catalysis B: Environmental*, vol. 176-177, pp. 486–499, 2015.

[134] L. Dubau, F. Maillard, M. Chatenet, J. André, and E. Rossinot, "Nanoscale compositional changes and modification of the surface reactivity of Pt3Co/C nanoparticles during proton-exchange membrane fuel cell operation," *Electrochimica Acta*, vol. 56, no. 2, pp. 776–783, 2010.

[135] F. Jiang, F. Zhu, F. Yang, X. Yan, A. Wu, L. Luo, X. Li, and J. Zhang, "Comparative Investigation on the Activity Degradation Mechanism of Pt/C and PtCo/C Electrocatalysts in PEMFCs during the Accelerate Degradation Process Characterized by an in Situ X-ray Absorption Fine Structure," *ACS Catalysis*, vol. 10, no. 1, pp. 604–612, 2019.

[136] Y. Zhao, J. Liu, Y. Zhao, and F. Wang, "Composition-controlled synthesis of carbon-supported Pt-Co alloy nanoparticles and the origin of their ORR activity enhancement," *Physical chemistry chemical physics : PCCP*, vol. 16, no. 36, pp. 19 298–19 306, 2014.

[137] N. Ishiguro, S. Kityakarn, O. Sekizawa, T. Uruga, H. Matsui, M. Taguchi, K. Nagasawa, T. Yokoyama, and M. Tada, "Kinetics and Mechanism of Redox Processes of Pt/C and Pt 3 Co/C Cathode Electrocatalysts in a Polymer Electrolyte Fuel Cell during an Accelerated Durability Test," *The Journal of Physical Chemistry C*, vol. 120, no. 35, pp. 19 642–19 651, 2016.

[138] L. Dubau, J. Durst, F. Maillard, M. Chatenet, J. André, and E. Rossinot, "Influence of PEMFC Operating Conditions on the Durability of Pt 3 Co/C Electrocatalysts," *ECS Transactions*, vol. 33, no. 1, pp. 399–405, 2010.

[139] Y. Tan, H. Matsui, N. Ishiguro, T. Uruga, D.-N. Nguyen, O. Sekizawa, T. Sakata, N. Maejima, K. Higashi, H. C. Dam, and M. Tada, "Pt–Co/C Cathode Catalyst Degradation in a Polymer Electrolyte Fuel Cell Investigated by an Infographic Approach Combining Three-Dimensional Spectroimaging and Unsupervised Learning," *The Journal of Physical Chemistry C*, vol. 123, no. 31, pp. 18 844–18 853, 2019.

[140] S. Chen, H. A. Gasteiger, K. Hayakawa, T. Tada, and Y. Shao-Horn, "Platinum-Alloy Cathode Catalyst Degradation in Proton Exchange Membrane Fuel Cells: Nanometer-Scale Compositional and Morphological Changes," *Journal of The Electrochemical Society*, vol. 157, no. 1, p. A82, 2010.

[141] N. Ramaswamy, S. Kumaraguru, W. Gu, R. S. Kukreja, K. Yu, D. Groom, and P. Ferreira, "High-Current Density Durability of Pt/C and PtCo/C Catalysts at Similar Particle Sizes in PEMFCs," *Journal of The Electrochemical Society*, vol. 168, no. 2, p. 024519, 2021.

[142] Y. Yang, M. Bai, J. Lv, L. Gao, Y. Li, X. Lv, Y. Li, and Y. Song, "One-Dimensional Modeling for Aging of Pt-Co Core-Shell Catalysts in Proton Exchange Membrane Fuel Cells," *Journal of The Electrochemical Society*, vol. 169, no. 5, p. 054526, 2022.

[143] Y. Cai, J. M. Ziegelbauer, A. M. Baker, W. Gu, R. S. Kukreja, A. Kongkanand, M. F. Mathias, R. Mukundan, and R. L. Borup, "Electrode Edge Cobalt Cation Migration in an Operating Fuel Cell: An In Situ Micro-X-ray Fluorescence Study," *Journal of The Electrochemical Society*, vol. 165, no. 6, pp. F3132–F3138, 2018.

[144] S. Stariha, N. Macauley, B. T. Sneed, D. Langlois, K. L. More, R. Mukundan, and R. L. Borup, "Recent Advances in Catalyst Accelerated Stress Tests for Polymer Electrolyte Membrane Fuel Cells," *Journal of The Electrochemical Society*, vol. 165, no. 7, pp. F492–F501, 2018.

[145] R. Mukundan, A. M. Baker, A. Kusoglu, P. Beattie, S. Knights, A. Z. Weber, and R. L. Borup, "Membrane Accelerated Stress Test Development for Polymer Electrolyte Fuel Cell Durability Validated Using Field and Drive Cycle Testing," *Journal of The Electrochemical Society*, vol. 165, no. 6, pp. F3085–F3093, 2018.

[146] U.S. Department of Energy, "Fuel Cell Technologies Office Multi-Year Research, Development, and Demonstration Plan - Section 3.4 Fuel Cells: 2016 FUEL CELLS SECTION," 2016. [Online]. Available: https://www.energy.gov/eere/fuelcells/downloads/fuelcell-

[147] "CellEvaluationAndAnalysisProtocolGuideline: NEDO," 2014.

[148] S. Zhang, X. Yuan, H. Wang, W. Merida, H. Zhu, J. Shen, S. Wu, and J. Zhang, "A review of accelerated stress tests of MEA durability in PEM fuel cells," *International Journal of Hydrogen Energy*, vol. 34, no. 1, pp. 388–404, 2009.

[149] C. Takei, K. Kakinuma, K. Kawashima, K. Tashiro, M. Watanabe, and M. Uchida, "Load cycle durability of a graphitized carbon black-supported platinum catalyst in polymer electrolyte fuel cell cathodes," *Journal of Power Sources*, vol. 324, pp. 729–737, 2016.

[150] D. Bernhard, T. Kadyk, S. Kirsch, H. Scholz, and U. Krewer, "Model-assisted analysis and prediction of activity degradation in PEM-fuel cell cathodes," *Journal of Power Sources*, vol. 562, p. 232771, 2023.

[151] N. Ramaswamy, S. Kumaraguru, R. S. Kukreja, D. Groom, K. Jarvis, and P. Ferreira, "Mitigation of PtCo/C Cathode Catalyst Degradation via Control of Relative Humidity," *Journal of The Electrochemical Society*, vol. 168, no. 12, p. 124512, 2021.

[152] P. Schneider, C. Sadeler, A.-C. Scherzer, N. Zamel, and D. Gerteisen, "Fast and Reliable State-of-Health Model of a PEM Cathode Catalyst Layer," *Journal of The Electrochemical Society*, vol. 166, no. 4, pp. F322–F333, 2019.

[153] W. Bi, Q. Sun, Y. Deng, and T. F. Fuller, "The effect of humidity and oxygen partial pressure on degradation of Pt/C catalyst in PEM fuel cell," *Electrochimica Acta*, vol. 54, no. 6, pp. 1826–1833, 2009.

[154] K. Benaggoune, M. Yue, S. Jemei, and N. Zerhouni, "A data-driven method for multi-step-ahead prediction and long-term prognostics of proton exchange membrane fuel cell," *Applied Energy*, vol. 313, p. 118835, 2022.

[155] K. Chen, S. Laghrouche, and A. Djerdir, "Degradation model of proton exchange membrane fuel cell based on a novel hybrid method," *Applied Energy*, vol. 252, p. 113439, 2019.

[156] J. Fu, Z. Fu, and S. Song, "Proton membrane fuel cell stack performance prediction through deep learning method," *Energy Reports*, vol. 8, pp. 5387–5395, 2022.

[157] E. Maleki and N. Maleki, "Artificial Neural Network Modeling of Pt/C Cathode Degradation in PEM Fuel Cells," *Journal of Electronic Materials*, vol. 45, no. 8, pp. 3822–3834, 2016.

[158] H. Zhen, W. Gong, and L. Wang, "Offline data–driven evolutionary optimization based on model selection," *Swarm and Evolutionary Computation*, vol. 71, p. 101080, 2022.

[159] A. Tang, Y. Yang, Q. Yu, Z. Zhang, and L. Yang, "A Review of Life Prediction Methods for PEMFCs in Electric Vehicles," *Sustainability*, vol. 14, no. 16, p. 9842, 2022.

[160] R.-H. Lin, X.-N. Xi, P.-N. Wang, B.-D. Wu, and S.-M. Tian, "Review on hydrogen fuel cell condition monitoring and prediction methods," *International Journal of Hydrogen Energy*, vol. 44, no. 11, pp. 5488–5498, 2019.

[161] J. Kim, M. Kim, T. Kang, Y.-J. Sohn, T. Song, and K. H. Choi, "Degradation modeling and operational optimization for improving the lifetime of high-temperature PEM (proton exchange membrane) fuel cells," *Energy*, vol. 66, pp. 41–49, 2014. [Online]. Available: https://www.sciencedirect.com/science/article/pii/S0360544213007421

[162] H. Chen, P. Pei, and M. Song, "Lifetime prediction and the economic lifetime of Proton Exchange Membrane fuel cells," *Applied Energy*, vol. 142, pp. 154–163, 2015.

[163] X. Zhang, D. Yang, M. Luo, and Z. Dong, "Load profile based empirical model for the lifetime prediction of an automotive PEM fuel cell," *International Journal of Hydrogen Energy*, vol. 42, no. 16, pp. 11 868–11 878, 2017.

[164] T.-W. Lee, A. A. Tseng, K.-S. Bae, and Y. H. Do, "Simulation of the Proton-Exchange Membrane (PEM) Fuel Cell Life-Cycle Performance with Data-Driven Parameter Estimation," *Energy & Fuels*, vol. 24, no. 3, pp. 1882–1888, 2010.

[165] P. Pei, Q. Chang, and T. Tang, "A quick evaluating method for automotive fuel cell lifetime," *International Journal of Hydrogen Energy*, vol. 33, no. 14, pp. 3829–3836, 2008.

[166] M. Messing and E. Kjeang, "Empirical modeling of cathode electrode durability in polymer electrolyte fuel cells," *Journal of Power Sources*, vol. 451, p. 227750, 2020.

[167] M. K. Debe, A. K. Schmoeckel, G. D. Vernstrom, and R. Atanasoski, "High voltage stability of nanostructured thin film catalysts for PEM fuel cells," *Journal of Power Sources*, vol. 161, no. 2, pp. 1002–1011, 2006. [Online]. Available: https://www.sciencedirect.com/science/article/pii/S037877530601024X

[168] Wu Bi and Thomas F. Fuller, "Temperature Effects on PEM Fuel Cells Pt-C Catalyst Degradation," *Journal of The Electrochemical Society*, vol. 155, 2008.

[169] S. S. Kocha, "Electrochemical Degradation," in *Polymer Electrolyte Fuel Cell Degradation*. Elsevier, 2012, pp. 89–214.

[170] R. K. Ahluwalia, S. Arisetty, J.-K. Peng, R. Subbaraman, X. Wang, N. Kariuki, D. J. Myers, R. Mukundan, R. Borup, and O. Polevaya, "Dynamics of Particle Growth and

Electrochemical Surface Area Loss due to Platinum Dissolution," *Journal of The Electrochemical Society*, vol. 161, no. 3, pp. F291–F304, 2013 // 2014.

[171] Wu Bi, Qunhui Sun, Yulin Deng, and Thomas F. Fuller, "The effect of humidity and oxygen partial pressure on degradation of Pt-C catalyst in PEM fuel cell," *Electrochimica Acta*, vol. 54, pp. 1826–1833, 2009.

[172] E. F. Holby and D. Morgan, "Application of Pt Nanoparticle Dissolution and Oxidation Modeling to Understanding Degradation in PEM Fuel Cells," *Journal of The Electrochemical Society*, vol. 159, no. 5, pp. B578–B591, 2012.

[173] P. Urchaga, T. Kadyk, S. G. Rinaldo, A. O. Pistono, J. Hu, W. Lee, C. Richards, M. H. Eikerling, and C. A. Rice, "Catalyst Degradation in Fuel Cell Electrodes // Catalyst Degradation in Fuel Cell Electrodes: Accelerated Stress Tests and Model-based Analysis: Accelerated Stress Tests and Model-based Analysis," *Electrochimica Acta*, vol. 176, pp. 1500–1510, 2015.

[174] T. Jahnke, G. Futter, A. Latz, T. Malkow, G. Papakonstantinou, G. Tsotridis, P. Schott, M. Gérard, M. Quinaud, M. Quiroga, A. A. Franco, K. Malek, F. Calle-Vallejo, R. Ferreira de Morais, T. Kerber, P. Sautet, D. Loffreda, S. Strahl, M. Serra, P. Polverino, C. Pianese, M. Mayur, W. G. Bessler, and C. Kompis, "Performance and degradation of Proton Exchange Membrane Fuel Cells: State of the art in modeling from atomistic to system scale," *Journal of Power Sources*, vol. 304, pp. 207–233, 2016.

[175] Y. Li, K. Moriyama, W. Gu, S. Arisetty, and C. Y. Wang, "A One-Dimensional Pt Degradation Model for Polymer Electrolyte Fuel Cells," *Journal of The Electrochemical Society*, vol. 162, no. 8, pp. F834–F842, 2015.

[176] H. A. Baroody, D. B. Stolar, and M. H. Eikerling, "Modelling-based data treatment and analytics of catalyst degradation in polymer electrolyte fuel cells," *Electrochimica Acta*, vol. 283, pp. 1006–1016, 2018.

[177] S. G. Rinaldo, P. Urchaga, J. Hu, W. Lee, J. Stumper, C. Rice, and M. Eikerling, "Theoretical analysis of electrochemical surface-area loss in supported nanoparticle catalysts," *Physical chemistry chemical physics : PCCP*, vol. 16, no. 48, pp. 26 876–26 886, 2014.

[178] S. G. Rinaldo, W. Lee, J. Stumper, and M. Eikerling, "Catalyst Degradation: Nanoparticle Population Dynamics and Kinetic Processes," *ECS Transactions*, vol. 50, no. 2, pp. 1505–1513, 2013.

[179] ——, "Nonmonotonic dynamics in Lifshitz-Slyozov-Wagner theory: Ostwald ripening in nanoparticle catalysts," *Phys. Rev. E*, vol. 86, no. 4, p. 041601, 2012. [Online]. Available: https://link.aps.org/doi/10.1103/PhysRevE.86.041601

[180] H. A. Baroody and E. Kjeang, "Predicting Platinum Dissolution and Performance Degradation under Drive Cycle Operation of Polymer Electrolyte Fuel Cells," *Journal of The Electrochemical Society*, vol. 168, no. 4, p. 044524, 2021.

[181] L. Lu, M. Ouyang, H. Huang, P. Pei, and F. Yang, "A semi-empirical voltage degradation model for a low-pressure proton exchange membrane fuel cell stack under bus city driving cycles," *Journal of Power Sources*, vol. 164, no. 1, pp. 306–314, 2007.

[182] J. M. Desantes, R. Novella, B. Pla, and M. Lopez-Juarez, "A modeling framework for predicting the effect of the operating conditions and component sizing on fuel cell degradation and performance for automotive applications," *Applied Energy*, vol. 317, p. 119137, 2022.

[183] M. Ou, R. Zhang, Z. Shao, B. Li, D. Yang, P. Ming, and C. Zhang, "A novel approach based on semi-empirical model for degradation prediction of fuel cells," *Journal of Power Sources*, vol. 488, p. 229435, 2021.

[184] C. Robin, M. Gérard, M. Quinaud, J. d'Arbigny, and Y. Bultel, "Proton exchange membrane fuel cell model for aging predictions: Simulated equivalent active surface area loss and comparisons with durability tests," *Journal of Power Sources*, vol. 326, pp. 417–427, 2016.

[185] M. Moein-Jahromi and M. J. Kermani, "Performance prediction of PEM fuel cell cathode catalyst layer using agglomerate model," *International Journal of Hydrogen Energy*, vol. 37, no. 23, pp. 17 954–17 966, 2012.

[186] N. Macauley, D. D. Papadias, J. Fairweather, D. Spernjak, D. Langlois, R. Ahluwalia, K. L. More, R. Mukundan, and R. L. Borup, "Carbon Corrosion in PEM Fuel Cells and the Development of Accelerated Stress Tests," *Journal of The Electrochemical Society*, vol. 165, no. 6, pp. F3148–F3160, 2018.

[187] K. H. Kangasniemi, D. A. Condit, and T. D. Jarvi, "Characterization of Vulcan Electrochemically Oxidized under Simulated PEM Fuel Cell Conditions," *Journal of The Electrochemical Society*, vol. 151, no. 4, p. E125, 2004. [Online]. Available: https://iopscience.iop.org/article/10.1149/1.1649756/pdf

[188] D. Gerteisen, "Impact of Inhomogeneous Catalyst Layer Properties on Impedance Spectra of Polymer Electrolyte Membrane Fuel Cells," *Journal of The Electrochemical Society*, vol. 162, no. 14, pp. F1431–F1438, 2015.

[189] N. Macauley, R. Mukundan, D. A. Langlois, K. C. Neyerlin, S. S. Kocha, K. L. More, M. Odgaard, and R. L. Borup, "Durability of PtCo/C Cathode Catalyst Layers Subjected to Accelerated Stress Testing," *ECS Transactions*, vol. 75, no. 14, pp. 281–287, 2016.

[190] M. Watanabe, H. Yano, D. A. Tryk, and H. Uchida, “Highly Durable and Active PtCo Alloy/Graphitized Carbon Black Cathode Catalysts by Controlled Deposition of Stabilized Pt Skin Layers,” *Journal of The Electrochemical Society*, vol. 163, no. 6, pp. F455–F463, 2016.

[191] H. Yano, M. Watanabe, A. Iiyama, and H. Uchida, “Particle-size effect of Pt cathode catalysts on durability in fuel cells,” *Nano Energy*, vol. 29, pp. 323–333, 2016.

[192] R. Jinnouchi, T. Hatanaka, Y. Morimoto, and M. Osawa, “First principles study of sulfuric acid anion adsorption on a Pt(111) electrode,” *Physical chemistry chemical physics : PCCP*, vol. 14, no. 9, pp. 3208–3218, 2012. [Online]. Available: https://pubs.rsc.org/en/content/articlepdf/2012/cp/c2cp23172g

[193] M. Zago, A. Baricci, A. Bisello, T. Jahnke, H. Yu, R. Maric, P. Zelenay, and A. Casalegno, “Experimental analysis of recoverable performance loss induced by platinum oxide formation at the polymer electrolyte membrane fuel cell cathode,” *Journal of Power Sources*, vol. 455, p. 227990, 2020.

[194] H. S. Choo, D. K. Chun, J. H. Lee, H. S. Shin, S. K. Lee, Y. S. Park, and B. K. Ahn, Eds., *SAE 2015 World Congress & Exhibition // Performance Recovery of Fuel Cell Stack for FCEV*, ser. SAE Technical Paper Series. SAE International400 Commonwealth Drive, Warrendale, PA, United States, 2015.

[195] D. Fantauzzi, S. Krick Calderón, J. E. Mueller, M. Grabau, C. Papp, H.-P. Steinrück, T. P. Senftle, A. C. T. van Duin, and T. Jacob, “Growth of Stable Surface Oxides on Pt(111) at Near-Ambient Pressures,” *Angewandte Chemie*, vol. 129, no. 10, pp. 2638–2642, 2017.

[196] C. Zalitis, A. Kucernak, X. Lin, and J. Sharman, “Electrochemical Measurement of Intrinsic Oxygen Reduction Reaction Activity at High Current Densities as a Function of Particle Size for Pt 4– x Co x /C (x = 0, 1, 3) Catalysts,” *ACS Catalysis*, pp. 4361–4376, 2020.

[197] H. Yano, I. Arima, M. Watanabe, A. Iiyama, and H. Uchida, “Oxygen Reduction Activity and Durability of Ordered and Disordered Pt 3 Co Alloy Nanoparticle Catalysts at Practical Temperatures of Polymer Electrolyte Fuel Cells,” *Journal of The Electrochemical Society*, vol. 164, no. 9, pp. F966–F972, 2017.

[198] G. Sievers, S. Mueller, A. Quade, F. Steffen, S. Jakubith, A. Kruth, and V. Brueser, “Mesoporous Pt–Co oxygen reduction reaction (ORR) catalysts for low temperature proton exchange membrane fuel cell synthesized by alternating sputtering,” *Journal of Power Sources*, vol. 268, pp. 255–260, 2014.

[199] J. Liu and Y. Huang, "Oxygen Reduction Reaction on PtCo Nanocatalyst: (Bi)sulfate Anion Poisoning," *Nanoscale research letters*, vol. 13, no. 1, p. 156, 2018.

[200] K. Kodama, A. Shinohara, N. Hasegawa, K. Shinozaki, R. Jinnouchi, T. Suzuki, T. Hatanaka, and Y. Morimoto, "Catalyst Poisoning Property of Sulfonimide Acid Ionomer on Pt (111) Surface," *Journal of The Electrochemical Society*, vol. 161, no. 5, pp. F649–F652, 2014.

[201] K. Kodama, A. Shinohara, R. Jinnouchi, and Y. Morimoto, "Strategies for Designing Ideal Pt/Ionomer Interfaces in Polymer Electrolyte Fuel Cells," *Popularizing FC-Vehicles: Desiging and Controlling Electrochmeical Reactions in the MEA*, no. 49, pp. 1–11, 2018.

[202] A. Ohma, K. Shinohara, A. Iiyama, T. Yoshida, and A. Daimaru, "Membrane and Catalyst Performance Targets for Automotive Fuel Cells by FCCJ Membrane, Catalyst, MEA WG," *ECS Transactions*, vol. 41, no. 1, pp. 775–784, 2011.

[203] Z. Yang, S. Ball, D. Condit, and M. Gummalla, "Systematic Study on the Impact of Pt Particle Size and Operating Conditions on PEMFC Cathode Catalyst Durability," *Journal of The Electrochemical Society*, vol. 158, no. 11, p. B1439, 2011.

[204] N. M. Markovic, H. A. Gasteiger, and P. N. Ross, "Oxygen Reduction on Platinum Low-Index Single-Crystal Surfaces in Sulfuric Acid Solution: Rotating Ring-Pt(hkl) Disk Studies," *The Journal of Physical Chemistry*, vol. 99, no. 11, pp. 3411–3415, 1995.

[205] J. N. Schwämmlein, G. S. Harzer, P. Pfändner, A. Blankenship, H. A. El-Sayed, and H. A. Gasteiger, "Activity and Stability of Carbon Supported Pt x Y Alloys for the ORR Determined by RDE and Single-Cell PEMFC Measurements," *Journal of The Electrochemical Society*, vol. 165, no. 15, pp. J3173–J3185, 2018.

[206] K. Kodama, K. Motobayashi, A. Shinohara, N. Hasegawa, K. Kudo, R. Jinnouchi, M. Osawa, and Y. Morimoto, "Effect of the Side-Chain Structure of Perfluoro-Sulfonic Acid Ionomers on the Oxygen Reduction Reaction on the Surface of Pt," *ACS Catalysis*, vol. 8, no. 1, pp. 694–700, 2017.

[207] T. Shinagawa, A. T. Garcia-Esparza, and K. Takanabe, "Insight on Tafel slopes from a microkinetic analysis of aqueous electrocatalysis for energy conversion," *Scientific reports*, vol. 5, p. 13801, 2015.

[208] S. Arisetty, X. Wang, R. K. Ahluwalia, R. Mukundan, R. Borup, J. Davey, D. Langlois, F. Gambini, O. Polevaya, and S. Blanchet, "Catalyst Durability in PEM Fuel Cells with Low Platinum Loading," *Journal of The Electrochemical Society*, vol. 159, no. 5, pp. B455–B462, 2012.

[209] P. Strasser, M. Gliech, S. Kuehl, and T. Moeller, "Electrochemical processes on solid shaped nanoparticles with defined facets," *Chemical Society reviews*, vol. 47, no. 3, pp. 715–735, 2018.

[210] M. Gummalla, S. Ball, D. Condit, S. Rasouli, K. Yu, P. Ferreira, D. Myers, and Z. Yang, "Effect of Particle Size and Operating Conditions on Pt3Co PEMFC Cathode Catalyst Durability," *Catalysts*, vol. 5, no. 2, pp. 926–948, 2015.

[211] Q. Jia, W. Liang, M. K. Bates, P. Mani, W. Lee, and S. Mukerjee, "Activity descriptor identification for oxygen reduction on platinum-based bimetallic nanoparticles: in situ observation of the linear composition-strain-activity relationship," *ACS nano*, vol. 9, no. 1, pp. 387–400, 2015.

[212] Q. Jia, C. U. Segre, D. Ramaker, K. Caldwell, M. Trahan, and S. Mukerjee, "Structure–property–activity correlations of Pt-bimetallic nanoparticles: A theoretical study," *Electrochimica Acta*, vol. 88, pp. 604–613, 2013.

[213] M. Wakisaka, H. Suzuki, S. Mitsui, H. Uchida, and M. Watanabe, "Increased Oxygen Coverage at Pt−Fe Alloy Cathode for the Enhanced Oxygen Reduction Reaction Studied by EC−XPS," *The Journal of Physical Chemistry C*, vol. 112, no. 7, pp. 2750–2755, 2008. [Online]. Available: https://pubs.acs.org/doi/pdf/10.1021/jp0766499

[214] Y. Huang, J. Zhang, A. Kongkanand, F. T. Wagner, J. C. M. Li, and J. Jorné, "Transient Platinum Oxide Formation and Oxygen Reduction on Carbon-Supported Platinum and Platinum-Cobalt Alloy Electrocatalysts," *Journal of The Electrochemical Society*, vol. 161, no. 1, pp. F10–F15, 2014.

List of Figures

List of Tables

List of Abbreviations and Symbols

Latin letters

A	active area of the MEA	cm^2
a_i	activity of species in the electrochemical reaction	$-$
c_{Pt}^{ref}	reference Pt concentration	$molm^{-3}$
E	potential difference between anode and cathode	V
E^0	standard potential	V
E_C	cathodic half cell voltage	V
$ECSA_A$	electrochemical active surface area of the anode	$cm_{Pt}^2 cm^{-2}$
$ECSA_C/ECSA$	electrochemical active surface area of the cathode	$cm_{Pt}^2 cm^{-2}$
$ECSA_{norm}$	normalized electrochemical active surface area	$-$
F	Faraday constant	$Cmol^{-1}$
f_N	dimensionless normalized particle radius distribution function	$-$
g_τ	correlation factor k_{dis} τ	s^{-1}
g_{LPL}	correlation factor k_{dis} LPL	V^{-1}
g_{RH}	correlation factor k_{dis} RH	$-$
g_T	correlation factor k_{dis} T	$-$
g_{UPL}	correlation factor k_{dis} UPL	V^{-1}
h_τ	correlation factor k_{rdp} τ	s^{-1}
h_{UPL}	correlation factor k_{rdp} UPL	V^{-1}
i	current density	Acm^{-2}
i_0	exchange current density	Acm_{Pt}^{-2}
i_{H_2}	hydrogen crossover current	Acm^{-2}
i_{lim}	limiting current density	Acm_{Pt}^{-2}
J^+	creation term in the Smoluchowski coagulation equation	s^{-1}

J^-	extinction term in the Smoluchowski coagulation equation	s^{-1}
k	number of AST cycles	–
k_{det}	detachment rate	s^{-1}
k_{dis}	dissolution rate	ms^{-1}
k_{rdp}	redeposition rate	ms^{-1}
m	Tafel-slope	$mVdec^{-1}$
$M_N(t)$	normalized dimensionless mass moment of fN (r,t)	–
M_{Pt}	molecular weight of Pt	$gmol^{-1}$
m_V	Pt mass loading per unit volume	gm^{-3}
n	number of electrons	–
p_1	empirical correlation parameter	$mVdec^{-1}$
p_2	empirical correlation parameter	$mVdec^{-1}$
p_3	empirical correlation parameter	Acm_{Pt}^{-2}
p_4	empirical correlation parameter	–
p_{H2}	hydrogen partial pressure	Pa
p_{O2}	oxygen partial pressure	Pa
q	conducted charge	C
R	Ideal gas constant	$Jmol^{-1}K^{-1}$
r	particle radius	nm
R_0	characteristic particle radius	nm
R_{H^+}	proton transport resistance	$m\Omega$
R_{HFR}	High frequency resistance	$m\Omega$
R_{mt}	oxygen mass transport resistance	scm^{-1}
T	temperature	K
U_{Cell}	cell voltage	mV
V_m	molar volume of Pt	m^3mol^{-1}
V_{RHE}	potential vs. the Reversible Hydrogen Electrode	V
W_{elec}	electrical work	$kJmol^{-1}$

Greek letters

α	transfer coefficient	–
$\Delta\eta^{g}_{act,m,ECSA}$	overpotential change due to ECSA and exchange current density	mV
$\Delta\eta^{g}_{act,m,i0}$	overpotential change due to Tafel slope and exchange current density	mV
$\Delta\eta^{g}_{act,m}$	overpotential change due to Tafel slope variation	mV
ΔG	Gibbs Free Energy	$kJmol^{-1}$
ΔS^{0}_{rxn}	entropy of reaction at standard conditions	$Jmol^{-1}K^{-1}$
$\eta_{act,A}$	anode activity overpotential	mV
$\eta_{act,C}/\eta_{act}$	cathode activity overpotential	mV
η^{g}_{act}	generalized cathode activity overpotential	mV
η_{H^+}	proton transport overpotential through ionomer	mV
η_{HFR}	ohmic resistance overpotential	mV
η_{HOR}	HOR overpotential	mV
η_{mt}	oxygen mass transport overpotential	mV
η_{ORR}	ORR overpotential	mV
η_{PtOx}	platinum oxide overpotential	mV
γ	ORR reaction order wrt p_{O_2}	–
τ	hold time in accelerated stress	s
τ_{ref}	reference hold time in accelerated stress	s

Sub- and Superscripts

BOL	Begin of Life
EOT	End of Test
exp	based on experimental data
g	generalized approach
$PtOx$	related to the platinum oxide containing state of the catalyst
$PtOx-free$	related to the platinum oxide-free state of the catalyst
sim	based on modeled data

Abbreviations

BPP	bipolar plates
CCL	cathode catlyst layer
CCM	catalyst coated membrane
CL	catalyst layer
CV	Cyclic Voltammogram
ECSA	electrochemical surface area
FFP	flow field plates
GDL	gas diffusion layer
HDV	heavy-duty-vehicle
HHV	higher heating value
HOR	hydrogen oxidation reaction
ICE	internal combustion engine
KIT	Karlsruhe Institute of Technology
LDV	light-duty-vehicle
LHV	lower heating value
LPL	lower potential limit
MEA	membrane electrode assembly
MPL	micro-porous layer
OCV	open circuit voltage
ORR	oxygen reduction reaction
PEM-FC	Polymer Electrolyte Membrane Fuel Cell
PFSA	polyperfluorosulfonic acid
PGM	platinum group metals
PRD	particle radius distribution
PTFE	polytetrafluoroethylen
PtOx	platinum oxide
RH	relative humidity
TFE	tetrafluoroethylen
UPL	upper potential limit

A Appendix

A.1 Derivation of the equations 5.16-5.18

The following Equation is based on Equations 5.11-5.12 under the assumption, that both the Tafel slope m and the exchange current density i_0 vary during the degradation process of a PEM-FC cathode:

$$
\begin{aligned}
\Delta E_C(k,i) &= \eta^g_{act}(k) - \eta^g_{act}(0) \\
&= m(k) \cdot log\left(\frac{i}{i_0(k) \cdot ECSA(k)}\right) \\
&- (m(0) + m(k) - m(k)) \cdot log\left(\frac{i}{i_0(0) \cdot ECSA(0)}\right) \\
&= (m(k) - m(0)) \cdot log\left(\frac{i}{i_0(k) \cdot ECSA(k)}\right) \\
&+ m(k) \cdot log\left(\frac{i}{i_0(k) \cdot ECSA(k)}\right) - m(k) \cdot log\left(\frac{i}{i_0(0) \cdot ECSA(0)}\right) \\
&= \underbrace{(m(k) - m(0)) \cdot log\left(\frac{i}{i_0(0) \cdot ECSA(0)}\right)}_{\Delta\eta^g_{act,m}(k,i)} + \underbrace{m(k) \cdot log\left(\frac{ECSA(0)}{ECSA(k)}\right)}_{\Delta\eta^g_{act,m,ECSA}(k)} \\
&+ \underbrace{m(k) \cdot log\left(\frac{i_0(0)}{i_0(k)}\right)}_{\Delta\eta^g_{act,m,i_0}(k)}
\end{aligned}
\tag{A.1}
$$